UNIVERSITY OF LEEDS

The Effect of Corrosion on the Particle Emissions Emitted from Different Brake Rotor Materials

By Ishmaeel Ghouri

Submitted in accordance with the requirements for the Degree of Philosophy

The University of Leeds

School of Mechanical Engineering

Institute of Design, Robotics and Optimisation

2025

Intellectual Property

The candidate confirms that the work submitted is his own and that appropriate credit has been given where reference has been made to the work of others.

Signed

Acknowledgements

First and foremost, I would like to express my deepest gratitude to the Almighty for His countless blessings.

I am profoundly grateful to my supervisors, Professor David Barton, Professor Richard Barker, and Dr Peter Brooks, for their invaluable support, insightful feedback, and unwavering encouragement throughout my research. Their guidance has been instrumental in shaping the direction and quality of this work.

My sincere thanks also go to Anthony Wiese, Fabian Limmer, the electrical team, Tarsem Hunjan, Matthew Buckley and Hardy Whiteley-Boocock for their technical advice, collaboration, and support. Your contributions have been crucial to the success of this project.

I want to extend heartfelt thanks to my beloved family, my mother, father, brothers, and sisters, for their endless love, patience, and encouragement. Your unwavering belief in me provided the strength I needed during the most challenging moments. I truly could not have achieved this without you.

I am also thankful to my peers and colleagues, Callum Sweeney, Francess Dent, Pyria Afrian, Ramesh Devaramani, and everyone in Office 3.39a for their camaraderie and for making the tough times more bearable. Your support and shared laughter have meant a great deal.

To the third-year students, Imran Shaikh, Sam Williamson, Nikita Bogdanovs and Sree Sriram, who completed their final-year projects under my supervision, thank you for your hard work and dedication. It was a pleasure working with each of you, and I wish you all the very best in your future endeavours.

I would like to thank TMD Friction for supplying friction material and Suman Shrestha from Curtiss-Wright Keronite for their generous support in sharing technical knowledge, which significantly enriched the practical aspects of this research.

I would like to sincerely thank the EPSRC for its financial support. Without it, this research would not have been possible.

Abstract

The new Euro 7 standard, set to be in place by 2026, will be the first legislation to attempt to cap the emissions produced by a friction brake system. This has prompted brake manufacturers to seek alternative solutions to reduce the emissions generated by conventional grey cast iron (GCI) friction brake systems. With electric vehicles becoming the future of modern vehicles, their regenerative braking system will cause friction brakes not to be used as frequently as in an internal combustion engine vehicle. This may lead to a build-up of corrosion on the brake rotor that may not only affect the performance and service life of the brakes but also increase particle wear emissions when braking.

This study compares the friction, wear and emission characteristics of two aluminium-based rotors with those of a conventional GCI rotor. Aluminium metal matrix composites (Al-MMC) and plasma electrolytic oxidation (PEO)- treated aluminium (Al-PEO) rotors were the two selected aluminium-based alloys alternative to GCI. As these lightweight materials could be a solution to reduce the risk of corrosion failure, possibly lower brake emissions, and improve the overall efficiency of the vehicle by reducing its unsprung mass.

Generally, all 3 rotors produced satisfactory and stable coefficient of friction (CoF), both before and after corrosion. However, wear and emissions from the GCI rotor increased significantly after the corrosion cycle. The Al-MMC rotor also suffered some deleterious effects of corrosion, mainly due to SiC particles being dislodged from the surface. Although there was some evidence of surface damage away from the rubbing surface, the Al-PEO rotor produced the lowest particulate emissions of all 3 rotors, both before and after corrosion. These results suggest that, with further optimisation of the PEO processing conditions and a more compatible pad material, the Al-PEO rotor is a viable and more environmentally-friendly alternative to the current GCI system.

Contents

List of Figures

List of Tables

Chapter 1

Introduction

> *"The journey of a thousand miles begins with a single step"*
> *Lao Tzu*

1.1 Research background

Over the years, there have been significant developments in reducing greenhouse gases and other air pollutants emitted by internal combustion engine (ICE) vehicles, despite an increase in the total number of vehicles each year. More strict restrictions on ICE vehicles have led some countries to place a ban on the sale of new ICE vehicles to help tackle climate change [1]. With Norway being one of the first countries to plan to implement this, two-thirds of all new vehicles sold in Norway in 2021 had fully electric powertrains [2]. As more countries, such as the UK, Denmark, Germany, Iceland and others follow in the footsteps of Norway, banning sales of new ICE vehicles will inevitably lead to a substantial increase in the number of battery electric vehicles (BEVs) on the road [3], [4].

Despite BEVs not producing any exhaust emissions, they still emit particulate matter (PM) into the environment, mainly from the wearing of brakes, tyres, road surfaces and the resuspension of road dust. With BEVs becoming more popular and the decline of ICE vehicles, it is predicted that the non-exhaust PM emissions will soon surpass those from the exhaust [5]. One of the biggest contributors to non-exhaust emissions is the friction brake system. As part of the braking mechanism to slow or stop a vehicle, wear particles are released from the brakes and emitted into the environment. Brake particles not only cause pollution to the environment but pose direct risks to human health [6]. There is evidence that friction brake emissions will continue to increase with the rising number of vehicles on the road each year [7].

Most BEVs are fitted with regenerative braking, in which the drive motor acts as a generator to convert the vehicle's kinetic energy into electrical energy and hence retard the vehicle [8]. The electrical energy generated from braking is fed back into the vehicle battery, thereby increasing the BEVs range by 8% to 25% compared to vehicles without regenerative braking [9]. However, when the battery is nearly fully charged, the regenerative braking system is less relied on, and the vehicle system switches to relying on the friction brakes to slow or stop the vehicle. At low speeds, the regenerative braking is efficient [10].

The most commonly used brake rotor material is grey cast iron (GCI) [11]. This is unsurprising as GCI has good mechanical properties and low manufacturing costs [12]. Despite these desirable properties, GCI is highly prone to corrosion, which is known to affect braking performance and increase particle emissions [13], [14]. As a disc brake system is generally an open design to allow for airflow to cool the rotor in particular, this poses a problem as it allows the atmospheric environment to cause potential damage to the brake system. In locations that experience a large amount of rainfall or freezing conditions, this can lead to corrosion problems. For example, the acidity of rainwater can have an impact on the rate of corrosion [15]. The use of salts such as sodium chloride, magnesium chloride and calcium chloride on the roads in freezing conditions can also influence the rate of corrosion [16]. When such salts are absorbed in water, concentrated chloride solutions are formed which are highly corrosive and are known to cause corrosion pits in metals even when they have protective coatings [15], [17].

It is estimated that the global cost of corrosion in 2013 was 2.5 trillion US dollars. An estimate between 15% and 35% of the corrosion cost ($375 to $875 billion) could be saved if effective corrosion control practices were implemented [18]. The automotive industry is not immune to corrosion, especially of disc brakes as they are open to the environment and most brake rotors are made of cast iron, which is highly prone to corrosion leading to the formation of iron oxide products (red rust) on its exposed surfaces.

The development of regenerative braking systems to recover energy loss from braking battery electric vehicles (BEV), by electrical means, leads to less severe demand and less frequent use of the friction brake. As most road vehicles use GCI brake rotors, this exacerbates the possibility of corrosion forming and remaining on the brake friction surfaces, thereby potentially reducing braking performance and increasing wear emissions as well as negatively affecting the appearance of the rotor.

A further problem with GCI as a rotor material is its density which is at least several times higher than that of most light alloys and polymers that have been increasingly used to replace ferrous materials in many other automotive structures and components. One solution to both the weight and corrosion problems of GCI brake rotors is to develop an alternative lightweight material which would ideally also be more corrosion resistant. A lightweight brake rotor would reduce the total mass of the vehicle resulting in less energy required to accelerate the vehicle and thereby improve overall vehicle efficiency leading to a greater range for BEVs before recharging. Moreover, as the brake rotor contributes a high proportion of the unsprung mass of the vehicle, a reduction in this mass will also reduce road damage and tyre emissions.

1.2 Research aim & objectives

1.2.1 Aim

The overall aim of this project is to investigate the effects of corrosion on the tribology and particle emissions of standard grey cast iron and alternative light-weight brake rotor materials.

1.2.2 Objectives

- To research, develop and implement a comprehensive dynamometer brake test and corrosion exposure protocol which can be applied in a consistent manner to all brake rotor materials investigated.
- To apply the developed protocol to a medium-size passenger car brake fitted with a GCI rotor in order to quantify the effects of corrosion on the braking performances and wear emissions from this industry-standard friction pair.
- To evaluate novel brake rotor materials, including SiC reinforced aluminium metal-matrix composite (Al-MMC) and an unreinforced aluminium alloy with a plasma electrolytic surface treatment (Al-PEO), when subjected to the same brake test regime before and after corrosion as for the standard GCI rotor.
- To use the test results to compare the impact of corrosion on the braking performance, particle wear emissions, and surface topography of the different rotor materials and to assess the overall merits of each material.

1.2.3 Research Approach

The motivation for this study stems from a previous investigation by Sanuddin et al. [19], on the particle emissions from a GCI compared to a prototype Al-PEO rotor. This study focused on braking performance, thermal impact, and particle wear emissions of the two brake rotors. It was found that the Al-PEO rotor produced lower PM emissions than the GCI rotor at low brake pressures. However, at higher brake pressures, the GCI rotor produced fewer emissions. As this was only a preliminary study, the friction material selected to run against for the Al-PEO rotor may not have been optimised for the novel PEO surface.

The present study builds on some of the aspects of this previous research, though there were also gaps in the methodology that warranted further development. The first step in this study was to identify an appropriate corrosion test procedure that was simple to carry out. A fixture was designed to house the brake rotor inside the salt spray chamber, and suitable friction materials for the Al-MMC and Al-PEO rotor were sourced. The brake test procedure was also modified from the previous study to incorporate the newly-developed corrosion test protocol in order to enable a meaningful comparison between the uncorroded and corroded brake rotors for each rotor material.

1.3 Structure of Thesis

This section briefly explains the content of each chapter

Chapter 2 - Literature Review

In Chapter 2, the fundamental theory and background of braking systems are presented, along with a review of research papers relevant to the present study.

Chapter 3 - Experimental Equipment, Materials and Methodology

In Chapter 3, the test methodology chosen for this project is presented and explained, along with a detailed description of the testing equipment. The testing materials, including the brake rotors and pads, are also described.

Chapter 4 - Grey Cast Iron Study

Chapter 4 presents the performance evaluation of the standard GCI brake rotor, including pad wear and particle emissions, under both uncorroded and corroded conditions. It includes surface imagery of the rotors pre- and post-corrosion, providing a visual comparison between the two states. Additionally, the chapter details the surface analysis and chemical characterisation of both the brake rotor and pads after testing.

Chapter 5 - Aluminium Metal Matrix Composite Study

The same test procedure and post-test analysis from the GCI study was applied in the Al-MMC study. The Al-MMC prototype brake rotor consisted of 30% SiC reinforcement in a cast aluminium alloy matrix. Its overall geometric parameters were based on the GCI brake from a Rover 75 vehicle and are similar to the dimensions of the GCI rotor used for the tests described in Chapter 4. The brake pads selected for the tests were aftermarket pads made for the Lotus Elise S1 sports car, which originally was fitted with Al-MMC brake rotors. The brake pads utilised a special glass-fibre reinforced formulation which was specifically developed to work against Al-MMC rotors.

Chapter 6 - Plasma Electrolytic Oxidation - Aluminium (PEO-Al) Study

The same test procedure for both braking and corrosion used for the GCI and Al-MMC studies was applied to the Al-PEO rotor. The 3-piece prototype PEO-Al rotor used in this study was machined from wrought Al 6082 billet. The PEO coating was only applied to the friction surface and not the whole brake rotor. The brake pads were the same bespoke pads developed for Al-matrix rotors used in the Al-MMC study.

Chapter 7 Discussion

Chapter 7 compares the performance, pad wear, and brake wear emissions of all three brake rotors under both uncorroded and corroded conditions. It includes a detailed and in-depth discussion of the impact of corrosion on the braking and emissions performances of each rotor.

Chapter 8 - Conclusion & Recommendations For Future Work

Chapter 8 Summarises the result and highlights the key findings from the research. Details of ideas and recommendations for future work are also outlined in this chapter.

Chapter 2

Literature Review

> *"Simplicity is the ultimate*
> *sophistication"*
> *Leonardo da Vinci*

2.1 Introduction to friction brakes

Automotive friction brakes have been around since the late 1800s, but they have not always looked like what we are used to today. The main function of an automotive brake system is to bring the vehicle to a stop or to slow it down in a safe and controlled manner. Friction brakes are not only used for slowing the vehicle down, but are also used as a parking brake.

Figure 2.1a shows an image of a typical hydraulic passenger car brake system. The brake system is mainly comprised of a master cylinder, brake lines, brake calliper or wheel cylinder, and the brake mechanism. Figure 2.1b shows the two main types of brake mechanisms, the disc brake and the drum brake. For the disc brake mechanism, when the driver activates the brake pedal by pushing on it, this causes the hydraulic fluid from the master cylinder to push out the pistons in the brake calliper, which are engaged with the brake pads. The brake pads are then pushed towards the brake disc, creating contact between the two surfaces. This contact between the stationary brake pad and the rotating brake disc generates a frictional torque, which is used to slow or stop the vehicle [20]. As shown in Figure 2.1b, the drum brake mechanism uses contact between the brake lining and brake drum rather than between the brake pad and brake disc. Similarly to how the brake pad and disc mechanism work, the brake fluid pushes the brake lining out, resulting in contact between the stationary brake lining and the rotating drum brake, which generates the required frictional torque [21].

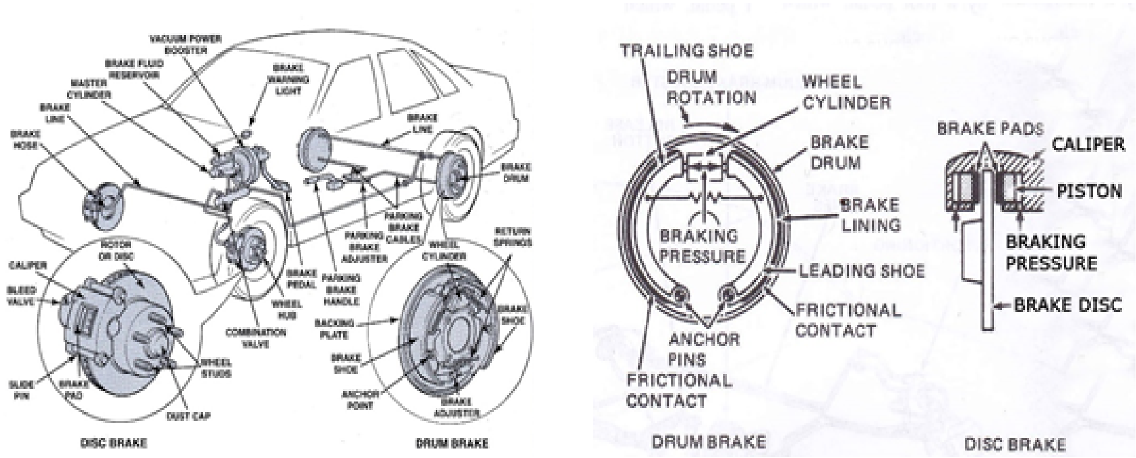

(a) Brake system [21]

(b) Brake disc and drum brake diagram [21]

Figure 2.1: Brake design

Friction is the resistance to motion during sliding or rolling when one surface moves relative to another surface whilst in contact [22]. The brake pad, Figure 2.2a, is usually made from a steel backing plate with a friction material either bonded or pressed on it [23]. The friction material is what is used to generate friction against the brake rotor, as shown in Figure 2.2b. Therefore, a rough brake pad surface can lead to high levels of friction. However, there is a strong correlation between high levels of friction and high wear rate, which is undesirable [23].

(a) Brake pads [24] (b) Brake rotor [24]

Figure 2.2: Brake friction pair

2.2 Thermal and NVH effects

The brake disc or rotor is the counterpart to the brake pads, as they are pressed together to create frictional torque, which is used to slow or stop the vehicle. During this process, kinetic energy from the vehicle is converted into thermal or heat energy, which is then dissipated into the environment [11]. Therefore, a brake disc material needs to be able to withstand high temperatures, different rubbing speeds, high pressures, and to possess wear resistance.

A disc brake is an open system which allows for more air cooling compared to a drum brake, which is a closed system, therefore, difficult to cool and more susceptible to overheating, leading to brake fade. This is the main reason why drum brakes are not often used on the front axle of a passenger car and are mainly used on the rear axle in small vehicles [25]. This is due to weight and cost saving compared to having disc brakes [26].

To increase cooling, vents and vanes are used in a ventilated brake disc, shown in Figure 2.3, to increase surface area, allowing for more airflow to travel through the brake disc compared to a solid brake disc. The extra cooling ability becomes useful, especially when under high load. The geometry and design of the vents in a brake disc can affect the air flow and heat transfer characteristics [27]. Kudal and Chopade. [27] carried out a comparison of a diamond pillar configured vented brake rotor with other arrangements, namely a straight radial vane, a tapered radial vane and a circular pillar. The diamond pillar rotor gave 26% less mass flow rate than the tapered radial vane, but it performed similarly for heat dissipation. In a comparison with the circular pillar, the diamond pillar dissipated 30% more heat. The reason for the diamond pillar brake rotor having a high heat dissipation despite a low mass flow rate is due to the airflow is more uniform with the diamond pillars, resulting in more symmetrical temperature distribution.

Figure 2.3: Vented disc brake [28]

Generally, the frictional forces between two surfaces are reduced as the temperature increases [29]. An ideal brake system should have a high thermal capacity to be able to store the heat generated from converting the kinetic energy of the vehicle. There should also be an effective cooling system, such as vents, so that the heat generated from braking can easily dissipate into the environment in order to allow the brake system to be ready for its next braking application. It is important to understand that there is only so much heat that can be absorbed and dissipated by the brake pads and disc [30]. When the brakes are reaching their thermal limit, they become less able to convert kinetic energy into heat. This leads to the brakes becoming less effective and results in the level of coefficient of friction starting to decrease, which is known as brake fade and commonly occurs over a long duration of braking or a series of repeated high speeds or high load conditions [30]. A thermal overload can lead to the brake fluid boil, cracked rotors, thermal deformation, high pad and rotor wear rate.

Noise, vibration and harshness or NVH, from a brake system is an unwanted phenomenon as it causes uncomfortable feelings to those inside and outside the vehicle and many warranted claims. NVH of brakes is an ongoing challenge for the brake industry, due to the complicity as it can be attributed from various factors such as friction material, brake rotor design and calliper design. Brake squeal and judder are two major categories of NVH in the brake system. Brake squeal occurs when the brake system becomes self-excited and generates friction-induced noise when the brakes are applied. Brake noise can occur even when the brakes are not applied, when the brake pads remain in contact with the rotor after the brake is released and when the pads rattle inside the calliper.

Brake noises have different names based on their frequencies. Figure 2.4 shows the different brake noises and their approximate frequency spectrum with human hearing ranging from 16Hz to 20kHz [31]–[33]. On the high end of the frequency range is brake squeal, which creates an audible noise from 500Hz upto in an excess of 15kHz. Brake judder is a forced vibration that can be felt through the brake pedal and even through the steering wheel, which gives the customer the impression that the vehicle is faulty. Cold and hot judders are the two main types judder. Cold judder can be caused when the rubbing path is non-uniform, such as rotor runout or disc thickness variation (DTV). Hot judder is similar to cold judder in that it is caused by a non-uniformity on the brake rotor surface. However, in hot judder, this non-uniformity is due to thermal distortion and sometimes phase transformation [26], [34].

2.3 Disc brake materials

2.3.1 Brake pad

There are three main types of brake pad friction material: metallic, ceramic and non-asbestos organic (NAO). NAO brake pads are comprised of different organic materials such as fibreglass, Kevlar and other materials which are bound together with resin. This makes it relatively soft and exhibits low brake noise. However, NAO brake pads are not designed for high performance or heavy vehicles due to it more susceptible to thermal

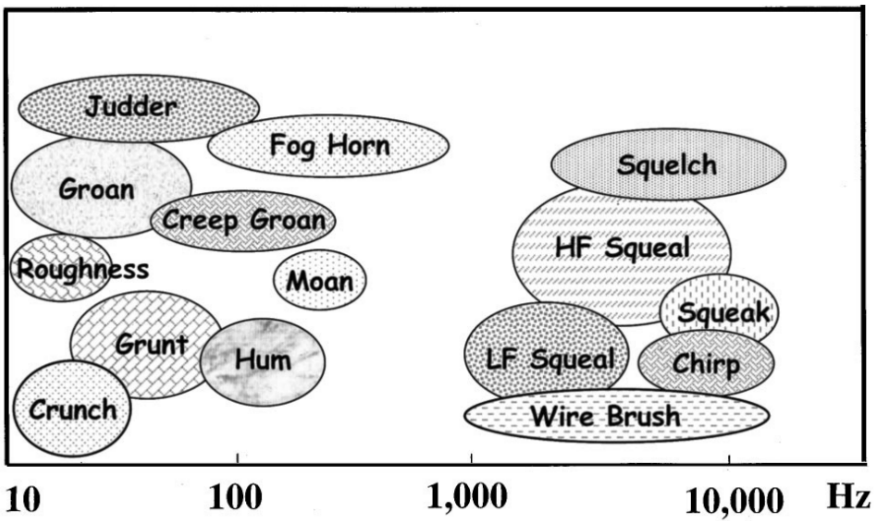

Figure 2.4: Different brake noises and their approximate frequency range [31]

degradation and unable to produce respectable amount of friction at high temperatures [35].

Low-metallic, semi-metallic, and low steel friction materials that have a certain weight percentage of metallic fibres in them, come under metallic brake pads. The different variations of metallic brake pads is dependent on the percentage of metal added to the friction material. Low-metallic brake pads are comprised of organic compounds with 10-30wt%, by mass, of metals [36]. Semi-metallic brake pads have a higher content of metal added, compared to low-metallic, around 30-70% by mass [36], [37]. Metallic brake pads provide a good level of friction at high temperatures, the increase in metallic content makes the brake pad more durable and increases heat transfer. However, metallic brake pads cause more wear on the brake rotor and produce more noise. Most metals are dense materials, which makes them heavy and adding metal fibres or particles to the brake pad composition can increase the overall weight of the brake pad. Metallic brake pads are used for high-performance vehicles or vehicles that undergo extreme braking conditions [36].

Ceramic brake pads mainly consist of ceramic fibres and filler material with small amounts of metal fibres to increase friction and thermal conductivity. Ceramic brakes produces less brake dust compared to NAO, with ceramic material having such a light colour, which helps brake dust to be less visible. Ceramic brake pads produce very little noise, and it also have a low wear rate. But it does have its limitations, due to the high working temperature, it is not used for commercial use, only for higher performance vehicles or racing cars. Also, ceramic brake pads are expensive due to the high manufacturing cost [37]. A summary comparison of organic, ceramic and metallic brake pads is shown in Table 2.1.

Table 2.1: Comparison of common types of brake pads [37]

	Brake pad material type		
	Organic	Ceramic	Metallic
Price	Low	High	Medium
Performance	Low	Medium	High
Noise	Low	Very low	High
Wear	Low	Very low	Medium

The brake pad friction materials are made from a mixture of fibres, friction modifiers, binders, and fillers. Depending on the material composition of the friction material can impact the performance.

The use of fibres is for reinforcing the friction material as they provide mechanical strength. The fibre material used in brake pads can be metallic, ceramic or organic. Fibreglass, rubber or Kevlar are organic materials used in the friction material. Fibreglass is commonly found in most passenger vehicles' brake pads due to its high tensile strength, and it has a high melting point of 1430 °C and it is a low conductor is a heat [23]. Kevlar fibre is thermal-resistant, has good wear resistance and a good stiffness-to-weight ratio. Kevlar fibres are mainly used for reinforcement to support the braking load. The thermal resistance adds some thermal stability at high temperature [23], [38].

Metallic fibres can provide good mechanical strength and structure to the friction material. They also have good thermal properties and the ability to absorb and dissipate heat quickly. Most metallic materials have high strength and hardness, which makes it suitable for reinforcing the brake pad. But this can also be a disadvantage as it can increase wear on the brake. However, metallic fibres can rust quite easily depending on the environment. Steel and brass are common types of metallic fibres used. Most metals have a high density, which makes them quite heavy. This can cause an issue as this adds extra weight, which can affect the performance and economy of the vehicle [39]. Ceramic fibres are used in brake pads as they have high strength, low weight, high thermal resistance and high melting point, with the properties that ceramic fibres possess to make them suitable for reinforcing the brake pad under load. Most metal oxides, nitrides or carbide materials are types of ceramic fibres.

Binders are necessary in brake pad structure as they provide structural integrity by holding all components of the friction material together. Especially when the brake pad is under high loads, the binder must not break down and crumble from the high mechanical and thermal stresses. If the binder starts to break down, it can cause the material component, for example, the reinforcing fibres, to break away, resulting in performance loss. Silicone, phenolic, and epoxy modified resins are common binder materials used in brake pads as they have high heat resistance [23], [40]. Gurunath et al. [41] tested two brake pad materials with different resins. The two NAO brake pads contain the same ingredient, but one contains a phenolic resin, whereas the other brake pads contain a new alternative resin. The new resin performed much better, even at high temperatures. The new resin showed much better suitability in shelf life by not producing emissions of noxious volatiles and very little shrinkage.

A large proportion of brake pad material comes from fillers, which are added to the brake pad to add overall bulk and to reduce cost. Fillers can be metals, alloys, ceramics or organic materials. The use of fillers can provide improvements or optimisation the brake pad performance, for example, aluminium oxide is used to increase the coefficient of friction, or the use of cashew dust or rubber to reduce brake noise [42], [43].

Friction additives or modifiers influence the brake pad's frictional properties and the wear rate. These additives contain a mixture of abrasive and lubricant materials. The lubricants are used to decrease the wear rate and to stabilise the coefficient of friction. Graphite is a common lubricant used in brake pads [23]. Gilardi et al [44] investigated the use of graphite powder in brake pads and focused on the noise performance and heat dissipation. The results indicated that the use of graphite in all tests for thermal conductivity is better than the sample without graphite. The NVH test showed that graphite contributes to noise reduction as well as suppressing some noise frequencies and noise intensity.

Abrasive materials are used to increase the coefficient of friction, by doing this it can lead to an increase in wear rate of the brake disc surface. However, this can be an advantage as it can remove the unwanted materials from the surface of the brake disc, such as iron oxides. Metal oxides and silicates are common materials used for abrasive friction additives, as these materials have a high hardness [23].

2.3.2 Disc brake rotor

Grey cast iron is the most common brake disc material used in passenger vehicles because of its high damping capability, melting point, thermal conductivity, and it is low manufacturing cost. However, cast iron has poor corrosion resistance, high density, and it has a high wear rate [11].

A large amount of research is going into developing alternative materials to replace grey cast iron, such as metal matrix composites, metal alloys, ceramics and carbon fibre. The use of ceramic and carbon fibre brake discs is only meant for high-performance vehicles and aeroplanes and not for passenger vehicles. Despite their attractive properties of high melting point and lightweight, they are not designed for a passenger vehicle. This is because they have poor performance at low temperatures due to their high working temperatures. As they show increase in strength with temperature, unlike other metals that decrease with temperature [45]. Table 2.2 shows the mechanical and thermal properties of some of the alternative materials for disc brakes. Both silicon carbide (SiC) and carbon fibre have a melting point over 2000°C compared with, grey cast iron found, passenger vehicles reaching high temperatures around 700°C and with normal urban use around 200°C [46]. Also, the manufacturing cost of ceramic and carbon fibre disc brakes is far greater than cast iron brake discs [47].

Table 2.2: Mechanical and thermal properties of brake disc [11]

Material	Melting point (°C)	Bulk density (g/cm3)	Thermal conductivity (W/m.K(°C))	Thermal expansion coefficient (µstrain/°C)	Vickers hardness (HV)	Young's modulus (GPa)	Poisson's ratio
Grey cast iron	1200	7.2	50-72	11-13	90-216	80-100	0.27
Aluminium MMC (Al-12SiC)	630	2.8	120-130	17.7-18	91-138	94-98	0.3
Titanium alloy (Ti 6Al-4V)	1600	4.43	8-9	8.7-9.1	332-336	113-115	0.34
Ceramic (SiC/SiC fibre composite)	2150-2500	2.3-2.9	6.8-7.4	2.8-5.2	1900-3500	179-259	0.15-0.23
Carbon-carbon composite (C/C)	3300	1.7	13-35	1.1-8.4	42-46	71-79	0.32

The use of lightweight alloys such as titanium alloys shows promise as it is lightweight with up to 37% reduction in weight compared to grey cast iron, high melting point and low thermal expansion coefficient. However, titanium alloy has been shown to have a higher wear rate compared to cast iron. Also, the manufacturing cost and process of titanium alloys are expensive and difficult to produce [11].

Blau et al. [48] investigated the use of titanium alloys as a replacement for truck brake discs to reduce weight. A variety of titanium alloys were used in this experiment, including two commercial, four experimental titanium-based hard particle composites and a thermally spray-coated titanium alloy. The results showed that the grey cast iron had better wear resistance with titanium alloys and composites. The addition of hard particles did improve the wear resistance of the titanium alloy. The thermal-sprayed titanium alloy measured the highest temperature, and the grey cast iron had the lowest. Overall, the thermal-strayed titanium alloy proved to have the most potential out of the titanium alloys and composite brake disc material.

Metal matrix composition (MMC) is made up of two types of materials, one metal and the other a reinforcement material. The common materials used for the metal part are beryllium, magnesium, titanium, iron, cobalt, silver and with aluminium being the largest usage metal material used. The reinforcement material used is usually a ceramic material due to its desirable properties. Examples of materials include silicon carbide, aluminium oxide, boron carbide, titanium carbide, titanium diboride, graphite and other ceramics [49]. Aluminium matrix composition (AMC) shows promise as it is lightweight. However, there is a drawback with AMC, which is its thermal limitations. AMC has a low melting temperature and high thermal expansion coefficient when compared to grey cast iron. Despite AMC drawbacks, it has been used in a commercial vehicle such as the Lotus Elise S1 and the Volvo V40 as the rear axle brake disc [50]. However, other properties need to be considered apart from having a low weight and good thermal properties Other properties include corrosion resistance, wear-resistance and low wear rate. Gulden et al. [13] investigated four types of aluminium matrix composite brake rotors. Three of the brake rotors had been reinforced with silicon carbide (SiC), and one

Table 2.3: Overview of material concepts [13]

Material Concept	A	B	C	D
SiC (volume percentage)	0	+	++	+++
Type of reinforcement	Without	Foam	Particle	Particle
Fabrication	Rolling	Casting	Casting	Casting
Dimensions (mm)	320*20	320*30	320*30	280*26
Design	Massive	Inside ventilated	Inside ventilated	Inside ventilated
Brake lining	NAO	ECE	NAO	NAO

was not reinforced, material A. The three reinforced brake rotors all contained a different percentage of silicon carbide. However, two of the reinforced brake rotors, materials C and D, contained different amounts of SiC particles. Whereas material B contained an open-pored SiC foam on the friction surface. Table 2.3 shows an overview of the investigated materials. The NAO brake pads material was used in the testing of the aluminium brake disc. After testing the unreinforced aluminium brake disc, showed that it is not a suitable material for a brake disc. The reason for this is that it showed signs of extreme wear, and no tribolayer was observed during the initial testing. After further testing was done, the formation of the tribolayer was confirmed by EDS, but the brake disc did show heavy wear. Both materials B and C show similar friction behaviour throughout the test, but material B showed smaller coefficient of friction values. Material D initially showed low coefficient of friction values, but throughout the test, the coefficient of friction value rose. However, despite its rising coefficient of friction values, the brake disc failed due to cracking. The main wear mechanism for the reinforced aluminium brake disc is thermomechanical fatigue and delamination due to the particle reinforcement. A cast-iron brake disc was also used, as a comparison to the AMC brake disc. The cast-iron brake disc had better coefficient of friction values than the AMC disc. However, the amount of wear was more than the AMC, even with more optimised brake pad material.

Thomas et al. [51] present a simulation of the thermomechanical behaviour of aluminium metal matrix composite brake disc. The simulation consisted of a frictional thermomechanical overload of a 1.0g stop from a velocity of 190km/h to 0km/h. A grey cast-iron brake disc was used in the comparison. During the simulation, the AMC brake disc initially had a lower temperature due to the higher heat dissipation as a result of its higher thermal conductivity. The heat, in the AMC brake disc, was evenly distributed throughout the disc brake due to its high conductivity. However, at the end of the simulation, the grey cast iron had a lower temperature due to it having a higher thermal capacity than the AMC.

Ahmad et al. [52] compared the coefficient of friction and wear rate of aluminium matrix composition and grey cast iron. The results concluded that the AMC disc had less weight loss at different speeds and loads. However, at high loads and speeds, the percentage difference was reduced. The coefficient of friction was similar for both the AMC and cast-iron disc at low speeds, again, at higher speeds the difference in coefficient of friction became more apparent.

Brake coatings

Exploring different materials is not the only method that is used to improve the material in a system. Coatings have been used throughout a variety of applications to reduce wear, increase strength and add a layer of protection. Over the years, various coating applications have been applied to the brake industry. There are numerous coating techniques that have been developed that provide different properties. The main coating techniques that have been used in brake application are High-velocity oxy-fuel (HVOF) and PEO, although other techniques have been explored and used in brakes [11].

High-velocity oxy-fuel is a type of thermal spray process the process involves particle material that is sprayed at high temperature and velocity onto the surface of the substrate material. The sprayed coating adheres to the surface of the substrate, forming a dense coating. HVOF is capable of coating metals, alloys and ceramics to the surface of the substrate material [11], [53].

Demir et al. [54] investigate three GCI with three different coatings brake discs. NiCr, Al_2O_3-Ti_2O_2 and NiCr-Cr_3C_2. The Al_2O_3 was coated by plasma spray, the NiCr-Cr_3C_2 was coated by HVOF and the NiCr was sprayed on as a bonding layer. The HVOF-coated brake shows high temperature during braking, but this did not affect the coefficient of friction, which was 6% higher than the original brake disc. The Al_2O_3-Ti_2O_2 showed the best wear resistance, as there was very little, however, the brake pad material wear rate was increased due to the hardness of the coating and the thermal barrier effect. The thermal barrier effect caused the brake pad to reach temperatures of 700°C. Krelling et al. [55] investigate the wear behaviour of HVOF thermally sprayed WC-10Co-4CR AISI 4140 steel. The hardness of the HVOF coating proved to be excellent wear behaviour.

Plasma electrolytic oxidation, or PEO or micro-arc oxidation is a type of non-thermal spray process [11]. This technique is used to grow a ceramic-like oxide layer on the surface of metals such as magnesium, aluminium, titanium, zirconium, niobium and tantalum. The difference between PEO and anodising process is that PEO uses a higher voltage for the anodic polarisation. The high voltage polarisation affects the oxide layer microstructure and phase composition, which leads the oxide layer to be harder, denser, have a good crystalline structure and have good adherence to the substrate material [56]. The hardness of a PEO-coated aluminium, aluminium oxide or alumina has a value of 1600HV compared to GCI with 500HV. Additionally, the PEO-coated aluminium could be up to 66% lighter [57].

Gulden et al. [50] investigated and compared the braking performance of PEO-coated aluminium brake rotors with grey cast iron. The PEO-coated brake disc consisted of an aluminium 6082 substrate with an oxide layer, alumina Al_2O_3, of about 40 µm thick. The coefficient of friction of the cast-iron brake disc was consistently higher than the PEO-coated aluminium brake rotor. As the brake pressure increased, the coefficient of friction decreased. The coated brake rotor formed a black tribolayer. During the duty formation of spots on the surface of the coated brake rotor was observed. Cracks and pitting were also found on the surface coated brake rotor which were believed to be caused by the differences in thermal expansion. The formation of cracks and pits may lead to an increase in brake pad wear due to the sharp edges on the rotor surface.

Alnaqi et al. [58] carried out a comparison on different 5 small-scale brake discs: PEO-coated aluminium alloy, PEO-coated aluminium MMC, uncoated aluminium alloys, uncoated aluminium MMC and cast iron. During the test, the plain aluminium alloy was unable to complete the test as the formation of scratches formed at low temperature. Both uncoated and coated aluminium MMC brake rotor has similar temperatures. Whereas the PEO-coated aluminium alloy showed a higher brake temperature and lower brake fade as it was able to maintain effective braking performance at high temperatures. The coefficient of friction values for all the brake rotors were similar, around 0.3 with grey cast iron having the highest coefficient of friction. But the uncoated aluminium MMC showed lower friction values, around 0.2. Also, the coated aluminium alloy brake disc experienced a catastrophic failure as it exceeded the surface temperature of 550°C, which is close to melting point of the aluminium alloy.

2.4 Brake testing equipment

After developing new brake material, testing must be carried out before it is placed on a vehicle. However, testing of brake material can be complex as many variables must be considered when it comes to simulating braking conditions. When trying to simulate braking conditions it should be known that it is not possible to simulate every braking scenario. Therefore, testing equipment used to carry out or simulate braking conditions needs to use specific test equipment to simulate braking conditions. However, there is other testing equipment that can be used, which is not designed to simulate braking conditions but to investigate the interactions of the brake pad and disc.

2.4.1 Vehicle scale testing

Vehicle scale brake testing is divided into two methods, the first method is the use of a chassis dynamometer and the second method is on-road testing. The chassis dynamometer uses a real vehicle as part of the test subject. The use of a real vehicle is to simulate, almost, real-world driving conditions [59]. The vehicle is tied down onto a controllable roller which can simulate the road interface. The controllable roller can be programmed to simulate different vehicle inertia and on-road conditions such as uphill and downhill gradients. The roller is also able to be programmed to simulate different driving cycles. On-road vehicle testing method uses a real vehicle, which is tested on an actual road rather than the use of an artificial road surface or a roller that is simulated to act as road.

The main use of chassis dynamometer and on-road testing methods has been focused on exhaust emissions rather than non-exhaust emissions. However, Mathissen et al. [59] measured the brake wear particle emission of a passenger vehicle on a chassis dynamometer. In this study, the use of a chassis dynamometer is a useful and reasonable tool for the investigation of brake wear particles. The chassis dynamometer offers a better understanding of how the vehicle affects the brake wear particle emissions such as the losses at the vehicle wheel and the chassis. There is also the benefit of controlling the environmental parameters. However, the chassis dynamometer is limited by its artificial cooling and ventilation. The cooling and ventilation of most brake dynamometers are quite low, this causes the brake wear particles to accumulate, which increases the background levels of brake particles. The cooling of the brake is limited due to the reduced airflow by the brake enclosure used to capture brake emissions. This creates unrealistically high brake temperatures which may increase the particle emissions. There is also the issue of contamination, the wear particles generated from the tyres can be mixed with the brake particles.

Hagen et al. [60] measured the brake wear particle emission with the uses of on-road vehicle testing method. The outcome of this study recommends that in the investigation of brake wear, emission measurement should be carried out on a scaled dynamometer. The reason for this recommendation is that the scaled dynamometer provides more optimisation regarding particle losses, advanced measurement, comparable test conditions, fewer technical restrictions, higher test-to-test reproducibility and more cost-efficiency.

2.4.2 Brake dynamometer

The brake dynamometer has been used in numerous amounts of studies for testing vehicle brake systems. It is one of the most used pieces of equipment for brake studies and in recent studies, it has been used to carry out brake wear emissions. A brake dynamometer is designed to simulate the braking system and the vehicle in real-world conditions. Depending on the type of brake dynamometer used, it can allow for test components and samples to be from commercial vehicles. The brake dynamometer also provides simulated conditions such as driving cycles and environmental parameters that are close to the real-world conditions. A brake dynamometer can be an enclosed system, allowing for it to be more optimised for particle emission and investigation of airflow. This allows for there to be more development in advanced testing methods and equipment [36], [60], [61].

There are many variations of the brake dynamometer that have been developed over time. However, most of them follow some key bases that are still the same in most cases. The key elements are the electric motor, inertia section and test section; Figure 2.5 shows an example of a basic brake dynamometer. The electric motor is used similarly to the engine in a vehicle, it is used to turn the drive shaft which is connected to the brake system and turns the wheels. The inertia section in the brake dynamometer is similar to a flywheel in a vehicle, it is used to simulate the vehicle's inertia. The inertia of a vehicle is important in a dynamometer as this helps to give a more realistic representation of the vehicle's inertia in real-world conditions. The test section houses the brake system, such as the brake calliper, disc and pad. Depending on the type of dynamometer used and the purpose of the study, it can also be equipped with a tyre to give a better representation of real-world conditions. The test section can also be enclosed, allowing for a more brake wear emission to be captured. The technological advancements in brake dynamometers have become advantageous, and now they are a critical part of the brake dynamometer. The reason for this is that the computer system software can be used to control the electronic motor to simulate the vehicle inertia instead of using weighted disks. Also, the control can be used to implement different driving cycles. In some advanced programs,

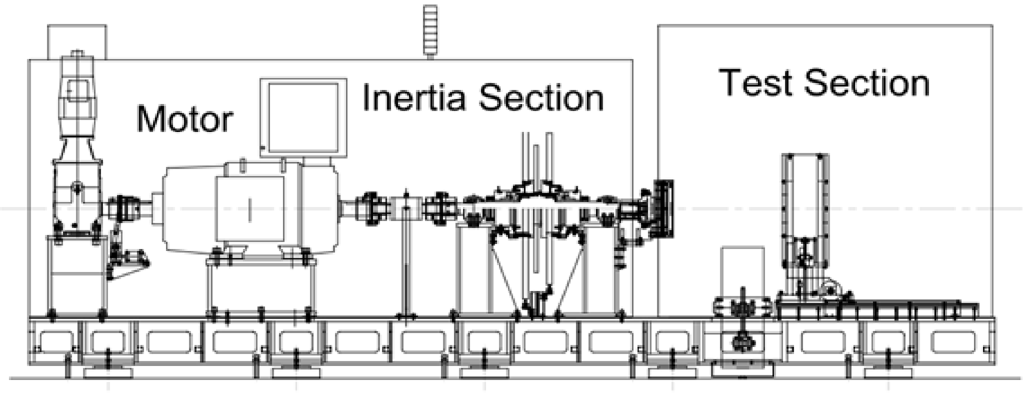

Figure 2.5: Basic sections of a brake dynamometer[61]

the driving cycles can be dependent on specified conditions such as brake temperature, torque and duration [60], [61].

The brake dynamometer can be an enclosed system which can be equipped with a particle capture system. This allows researchers to investigate the particle size and composition of brake wear emissions from different brake materials. Sanders et al. [62], Hagino et al [63], Hagen et al. [64], and Perricone et al. [65] have all used brake dynamometers to investigate the brake wear emissions.

A brake dynamometer has also been used to investigate how new brake materials will perform in real-world conditions. Gulden et al. [50], Hussain et al. [66], Demir et al. [54] used brake dynamometers to investigate the different brake materials and coatings.

2.4.3 Small scale dynamometer

A small-scale dynamometer is a scaled-down version of a dynamometer. A small-scale dynamometer has scaling factors and rules that adopt conditions similar to dynamometers. The use of small-scale tests is to investigate the friction and wear characteristics and their mechanisms. The main benefits of small-scale tests are cost and time effectiveness. The samples that are used in a small-scale dynamometer are smaller than those that are used in a full-scale dynamometer or the actual component [67].

Pin-on-disc (POD) machine is an example of small-scale test equipment. A POD is a type of tribometer, a piece of equipment that is used to measure the tribological properties of a material. The tribological properties that are mainly investigated when it comes to brake application are friction and wear characterisation. This mainly consists of the wear rates, wear-resistance and the coefficient of friction of the brake pad and disc [68]. The use of a pin-on-disc is a relatively simple and cost-efficient piece of equipment that has a wide range of applications.

Figure 2.6 below shows an image of a pin-on-disc tribometer. A pin-on-disc tribometer works by the pin being in contact with the surface of a rotating disc. The pin on the tribometer stays stationary, whereas the disc underneath rotates. This rotation and contract between the pin and disc create a sliding motion. Pin-on-disc works similarly to a conventional automotive brake disc system. A load can be applied to the pin to increase or decrease the contact pressure. This is quite like how the brake pressure can be increased or decreased, resulting in an increase or decrease in the braking force. The shape does not necessarily have to be a pin or spherical shape it can be a variety of shapes. The most common shapes are spherical, cylindrical or flat [68].

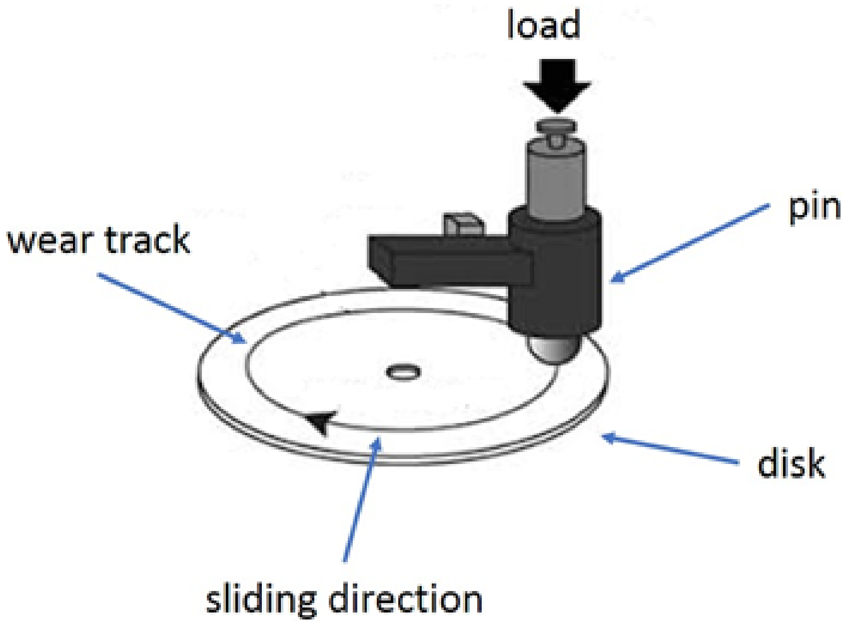

Figure 2.6: Schematic diagram of pin-on-disc [68]

Kukutschová and Filip. [69] produced a report on the “Review of brake wear emissions”. In this report, the authors disused how most researchers and manufacturers first start off using small laboratory equipment such as a pin-on-disc tribometer to understand the friction and wear properties. The pin-on-disc tribometer can also be used to investigate the performance of brake disc material rather than the brake pad. Several brake studies have used a pin-on-disc tribometer to conduct their experiment. A study by Wahlström et al. [70], investigates the concentration and size distribution of airborne wear particles from brake material. The experiment was conducted on a pin-on-disc tribometer which was equipped with particle counting equipment. The Pin-on disc was used to simulate urban driving conditions on eight different types of brake pad material. Lyu et al. [71] investigated the friction and wear of different cast iron, sinter and composite railway brake blocks at low ambient temperatures. This experiment was conducted on a pin-on-disc tribometer. A study that was carried out by Djafri et al. [72] investigated the tribological performances of three different brake disc materials when subjected to humidity and corrosion. Boyna et al. [67] carried out a comparison between a large-scale dynamometer and a small-scale dynamometer. For this comparison, a Bruker Universal Mechanical Tester (UMT) was used with a POD tribology test mode. The sample material of the disc was grey cast iron, as it is the most conventional brake rotor material. The sample material for the pin was cut from the brake pad. An adopted test procedure of the AK master's was used on the small-scale test. From testing, the large- and small-scale dynamometer showed differences in performance. This is believed to be the result of the temperature differences when testing, as it is difficult to have airflow in the UMT due to its design.

Pin-on-disc tests are not the only equipment that is used to carry out small-scale tests. Scaled-down versions of brake dynamometers have been used and developed for brake testing. There are many advantages of using small or reduced-scale dynamometers compared to full-scale dynamometers. The main benefits are related to hardware considerations, the reduced-scaled dynamometers eliminate the hardware effect such as the deflection of the brake calliper and the surrounding components [73].

Chung et al. [74] tested different abrasive components in NAO brake pads to investigate the formation and condition of the third body layer. The friction test was carried out on a

1/5 scaled brake dynamometer, which was based on a modified version of the JASSO C406 test brake dynamometer procedure. P. Sanders et al. [73] compared braking parameters and the frictional characterisation of a full-scale and reduced-scale dynamometer. The reduced-scale brake dynamometer showed excellent similarity in results compared to the full-scaled dynamometer, especially with NAO brake pad material. However, there are areas which the reduced-scaled brake dynamometer could be improved such as scaling factor from full-scale to a reduce scale and airflow around the disc.

2.4.4 Brake duty cycle

The development of brake materials must be tested. This can be in real-world driving conditions to monitor and gain a better understanding of its performance, temperature, wear rate, material stability, emissions and other properties that need to be investigated before they can be used in a commercial vehicle [75]. For this reason in mind, duty cycles or test procedures have been developed and designed to simulate real-world braking conditions and events. There is a wide range of duty cycles that can be used when testing brake systems. This is largely due to a high level of variability that needs to be included when developing duty cycles. These variabilities can consist of environmental conditions, road conditions, vehicle types, driving conditions and other such factors [76]. There are also duty cycles that are used for more specific investigations, such as looking at brake material, both brake pad and disc, monitoring the coefficient of friction over time, extreme temperature, wear rate and others [76].

Drag braking is an example of a duty cycle which is typically used to investigate the endurance of the brake system. Drag braking is when both brake pressure and vehicle speed are constant. Drag braking is typically used to simulate long braking situations, which is mainly situated within large vehicles or trucks going through a long descent [26]. Figure 2.7 shows the characteristic of drag braking. This is not the only reason for this type of duty cycle to be used. With the constant rubbing of the brake pad and disc, a large amount of heat is generated, which needs to be dissipated. The high temperature in the brake disc and or pads reduces the braking performance and increases wear [77]–[79].

During drag braking, the thermal capacity and surface heat transfer can be obtained [26]. Therefore, drag braking can be used to explore the brake thermal performance, as the main factor that limits the performance and increases wear rate is high surface temperature.

A very popular example of the drag braking duty cycle is the Grossglockner descent. Grossglockner is an extreme brake duty cycle that causes the brakes to experience harsh braking conditions. This brake duty cycle is based on the Grossglockner high alpine road in Austria. The duty cycle consists of 23 minutes of constant braking to simulate the vehicle slowing or maintaining a vehicle speed as it descends down the alpine road.

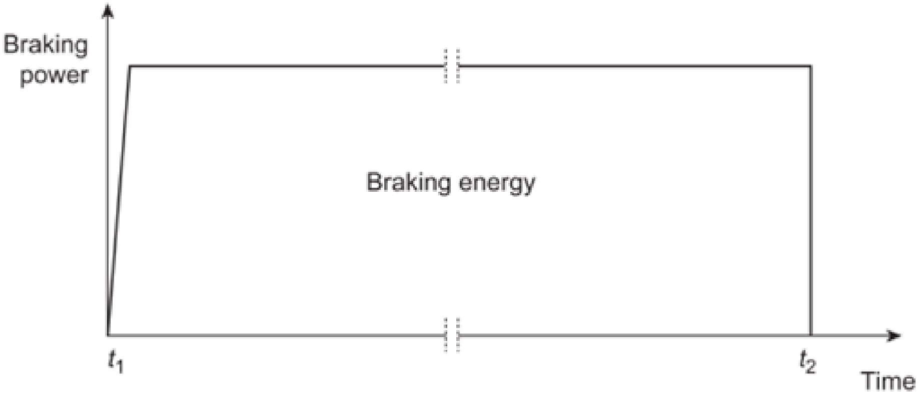

Figure 2.7: Drag braking characteristic [26]

Repeated braking is another type of brake application is braking from set point to set point. This involves the vehicle reaching a specific speed (Speed A) at which the brakes are applied and the vehicle decelerates to a lower specific speed (Speed B, which is usually a lower speed), after which it is then accelerated again to Speed A. This does not necessarily have to be controlled based on speed, but other parameters such as acceleration (g), brake torque, brake pressure, temperature and time. This duty cycle is usually repeated several times. Figure 2.8 shows the characteristic of the repeated braking duty cycle. This type of braking characteristic can be employed to simulate different driving conditions, such as real-world braking conditions. These types of duty cycles are used to develop a better understanding of the brake system, such as the performance, brake emissions, wear rate, surface topography, temperature, noise and others. These are different from the previously stated duty cycles, as these types of duty cycles are designed to put the braking system under extreme braking conditions, which can be unrealistic when compared to real-world use. There is a variety of different types of real-world duty cycles that have been developed.

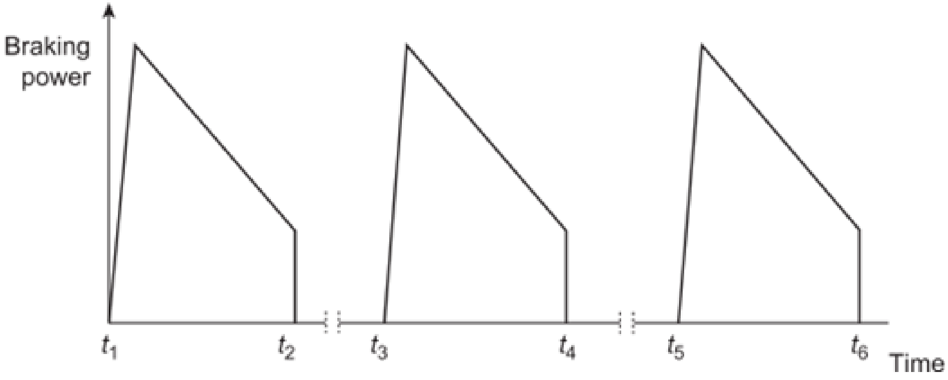

Figure 2.8: Repeated braking characteristic [26]

The Los Angeles City Traffic (LACT) is an example of a duty cycle that was based on real-world driving data records in Los Angeles US database. Therefore, this means that the LACT represents Los Angeles (US) driving conditions. This type of duty cycle was originally developed to measure brake lining wear. Additionally, it is commonly used to measure the NVH in a brake system [80]–[83]. The Mojacar test is another popular brake duty cycle that is used in the industry to measure wear, NVH and development programs. The Mojacar, like the LACT, is based on a driving route in Mojacar, Spain.

There are other types of duty cycles that have been developed to be a standardised test. An example of this is the AK Master. The AK Master is a type of duty cycle that was designed by the ArbeitsKreis (AK) working group [84]. The AK working group represents the European manufacture of friction linings and passenger cars [85]. With the development of the AK Master, it has been reconsidered by the Society of Automotive Engineers (SAE) as a useful test procedure in supporting the improvements of motor vehicle braking systems in overall performance and safety [85]. Therefore, the SAE brake dynamometer test standards committee has made the AK Master a recommended practice and has renamed it SAE J2522. The SAE J2522 test procedure is used to compare and assess the brake pad and disc under different speeds, temperatures, pressures and deceleration [86]. Also, the cooling behaviour of different test standards is taken into account, and the brake fade section is temperature-controlled [85]. Another example of a standardised test procedure by the SAE is the SAE J2521. The SAE J2521 is a test procedure for high-frequency noises and sequels. Other test procedures exist to test different aspects of the braking system.

The latest driving cycle that has been developed for the collection of brake emissions and a more realistic driving cycle is based on the Worldwide Harmonised Light Vehicle Test Procedure (WLTP) driving cycle, which replaced the NEDC test. The WLTP-brake cycle is a new laboratory test that was adopted from the WLTP driving cycle, which is used to measure fuel consumption and CO2 emissions from passenger vehicles. The WLTP-brake cycle consists of 303 braking stops over 10 trips. Figure 2.9 shows the time duration of the full WLTP-brake cycle.

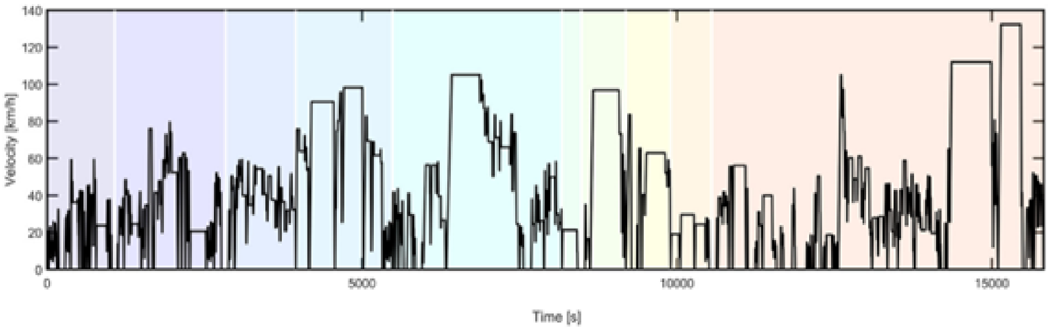

Figure 2.9: WTLP-brake cycle [87]

2.5 Brake technology

In recent years, there have been significant advancements in brake technologies equipped in modern vehicles. One of the earliest major innovations was the introduction of the Anti-lock Braking System (ABS). ABS is a crucial safety feature designed to prevent the wheels from locking during braking, which can cause the vehicle to slip or skid. ABS operates automatically without any input from the driver. It uses sensors to detect when a wheel begins to slip. When a slip is detected, a hydraulic valve reduces the brake pressure applied to that wheel. Once the wheel regains traction and is no longer slipping, the system re-applies the brake pressure. This cycle is repeated rapidly to maintain optimal braking performance while preventing wheel lock-up.

Brake technology has advanced significantly in recent years, with the possibility of shifting from traditional wet or hydraulic systems to dry braking systems such as Brake-by-Wire (BBW) and Electromechanical Brakes (EMB). BBW is a by-wire control technology that eliminates the mechanical and hydraulic components found in conventional brake systems. For example, the brake pedal is no longer connected to the master cylinder but instead to a sensor. This sensor detects the driver's braking input and sends an electronic signal to the motors within the EMB system. Unlike traditional brake callipers, which use pistons and hydraulic pressure, EMB systems utilise electric motors and gear mechanisms to activate the brakes. These innovations offer faster response times, more precise control, and integration with advanced driver-assistance systems (ADAS) [88], [89].

Advancements in braking technology have recently focused more on control systems rather than on the physical brake components themselves. One of the major developments in this area is the implementation of ADAS. ADAS significantly enhance vehicle safety by providing warnings and automatic interventions when potential hazards are detected. These systems help to prevent accidents by supporting the driver during critical moments.

In addition to improving safety, ADAS also enhances driving comfort by offering features such as adaptive cruise control, lane-keeping assistance, and parking assistance [90]. These functionalities reduce driver workload and contribute to a more convenient and relaxed driving experience.

2.6 Tribology of friction brakes

Over the years, tribology has been used in the development of brakes, such as improving performance, reducing NVH and wear. Tribology is the study of friction, wear and lubrication. Friction occurs in a brake system when the brake pad slides against the brake rotor, thus creating friction between the two surfaces. Surface roughness influences the friction generated, the rougher the surfaces are, the greater the resistance is produced. Over time, friction will result in wear. Wear is the progressive damage of a material surface, resulting in loss of material and mechanical performance. Lubrication is used to reduce or minimise friction and wear. This is done by the lubricant separating the two surfaces by reducing the interaction between them [91].

A tribolayer or third body layer is a layer of wear particles that is transferred between the pad and rotor during braking. When braking occurs, wear debris from both the brake pad and rotor is trapped between the mated surfaces and under compression and forms the tribolayer.

The tribolayer is a critical influence on the braking characteristic. The surface of new brake pads and rotors is not smooth due to machining. In order to mate the two surfaces together, a series of light brake applications are used, which is known as the bedding-in or burnishing process. The bedding-in process is not only critical to mate the two surfaces together but also an important part of the development of the tribolayer. During the bedding-in, wear debris from the brake pads and brake rotor is used to form the tribolayer. The tribolayer is part of the real-contact area between the pad and rotor surface, and the formation of the tribolayer plays a key role as it enhances the wear resistance and produces stable and high levels of coefficient of friction [92].

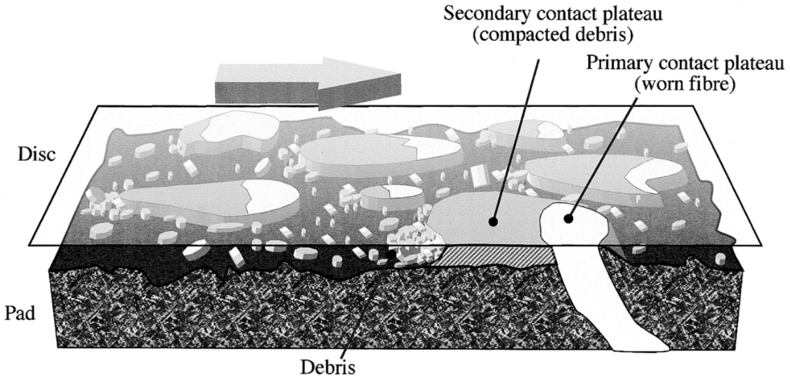

Figure 2.10: Tribolayer formation on the brake pad and rotor [93]

The tribolayer is made up of primary and secondary contact plateaux. The primary plateaux stems from the wear resistance ingredients in the friction material, which can be metal, glass or ceramic fibres [40]. The secondary contact plateaux are formed as a result of the primary plateaux, due to the hardness of the primary plateaux causing them to protrude on the surface of the friction material. The wear debris can become trapped and piled around the primary plateaux under the pressure between the pad and rotor, increasing the real contact area between them. The increased area of the real contact results in an increased level of friction [93].

The influences of brake loading, friction material and temperature all impact the tribolayer. If the brakes are under high load and temperature, it can cause the tribolayer to break down. However, the tribolayer can be rebuilt depending on brake loading and brake temperature and as such, the tribolayer is in a dynamic equilibrium between breaking down and rebuilding itself [50], [94].

A large amount of research has been carried out on tribology and the development of the tribolayer. Eriksson et al. [93] carried out a comprehensive study on the tribology of organic brake pads. This study explains the reason why friction increases during the bedding-in or running-in period. As the brake pad gets worn down, the primary plateaus form, therefore increasing the possible real contact areas—the increase in real contact area results in increased coefficient of friction. A study by Pinto et al. [95] found something similar. Pinto et al. investigated and characterised the contact plateaus on the friction material. It was found that the high value of mean CoF could be attributed to the high percentage and larger plateaus found in the sample.

Oesterle et al. [96] reported that the formation of is likely to consist of different phases of iron oxide from the brake rotor paired with different elements from the pad formulation. The elemental compositions of both brake rotor and pad material have direct impact on the tribolayer layer and its properties. Osterle et al [97] found that a higher lubricant concentration will increase the thickness of the tribolayer and decrease the CoF. The role of oxides on the tribolayer plays an important role. A study by Wei [98] found iron oxide widely dispersed on the tribolayer. A quantitative EDX analysis carried out by Eriksson et al. [93] found that the main component of the secondary contact plateaus is iron oxide.

2.7 Overview of brake wear emission

For a long time, exhaust emissions have been the focus of research as they contribute a large number of harmful emissions into the environment. However, recently, there has been more focus on non-exhaust emissions. The reason for this is that as the brake rotor and pad start to wear, some of the wear particles or brake dust are emitted into the environment, potentially causing harm to humans and the environment. The particle emission generated from brakes is the second-largest source of particulate emission after tailpipe emission from vehicles [99]. It is estimated that 50% of brake wear emissions become airborne, while the remainder is deposited on the road or around the vehicle [36]. Brake wear emissions fall under the non-exhaust emissions category, including emissions from tire and road surface wear.

The brake wear emissions are categorised into particulate matter (PM). PM refers to particles or droplets in the air. There are two main sizes, PM10 and PM2.5. PM10 or coarse PM is when the particle with an aerodynamic diameter of less than 10 micrometres. PM2.5 or fine PM is a particle has an aerodynamic diameter of 2.5 micrometres or less. Figures 2.11 and 2.12 present a size representation of PM10 and PM2.5, and the generation depth inside the human respiratory system.

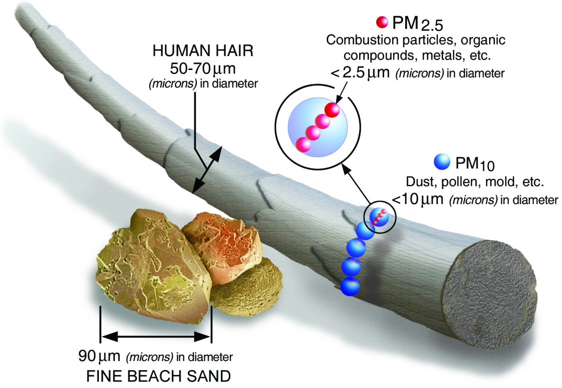

Figure 2.11: Size comparisons for PM particles [100]

The friction material in brakes is made up of different materials, such as copper, iron and brass are used as metallic fibres, and sulphides are also used as fillers [23]. These elements, especially metallic elements, can cause tissue damage and inflammation [101].

Therefore, exposure to fine particles (PM2.5) can enter the lungs and cause cardiovascular and respiratory problems [5].

As cast iron is the most common brake disc material and it is known to oxidise or rust easily. Therefore, if iron oxide particles start to enter the human body and depending on their PM size can lead to a severe health impact, as the small particles can travel into the bloodstream. Studies have been carried out on brake wear emissions and their impact on health effects. A study has found a link between brake wear particles to Alzheimer's disease [102]. This is because the magnetite, a form of iron oxide which is found in the brain of people who have died of Alzheimer's disease, is also found in brake wear emissions. Another study was conducted by Gasser et al. [103], who investigated the toxic effects of brake wear particles on epithelial lung cells in vitro. This experiment involved capturing brake wear particles from two types of braking behaviours (full stop and deceleration) and exposing them to lung cells. The results suggest that the brake wear particles damage tight junction cells and increase pro-inflammatory responses.

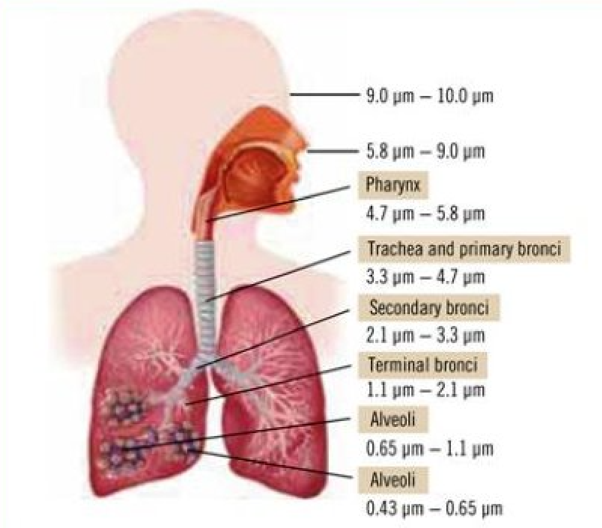

Figure 2.12: Particle size penetration into human respiratory system [104]

The introduction of the Euro 7 regulation is anticipated at the end of 2026. This regulation is expected to positively impact emissions from brakes, as it will be the first legislation to set limits on brake emissions, rather than focusing solely on tailpipe emissions. Historically, Euro regulations have primarily targeted tailpipe emissions. However, as vehicle engines become more efficient and the shift from ICE to EVs occurs, non-exhaust emissions are expected to exceed exhaust emissions.

It is estimated that approximately 55% of total non-exhaust PM10 emissions in urban environments come from brake emissions, while 11% originates from tire dust [7]. Furthermore, research indicates that exhaust and non-exhaust emissions contribute nearly equal amounts of PM10 emissions [99].

The Euro 7 regulation will limit emissions from vehicle brakes. Between 2026 and 2030, the allowed limit will be 7 mg per kilometre for vehicles with an ICE, including hybrids, and 3 mg per kilometre for pure EVs [105]. The test setup and procedures for measuring particle emissions are outlined in Global Technical Regulation (GTR) 24, and the designated drive cycle for these measurements is the WLTP-brake cycle [106].

As a result of the Euro 7 regulation an increase in research on the study of brake wear. Different types of friction material ingredients impact the amount of brake wear emissions. A study by Lyu et al. [107] researched brake pads with and without copper. The inclusion of copper in brake pads provides good thermal stability and aids in the development of the tribolayer. However, in recent years, the industry has been moving away from copper due to its toxicity [108]. Lyu et al. found that copper-free brake pads generated more airborne emissions than those containing copper.

Varriale et al. [109] investigated various pad ingredients and their influence on particle emissions. They found that brake pads containing steel fibres exhibited the highest coefficient of friction (CoF), followed by silicon carbide (SiC), aramid, and graphite. However, the pad containing SiC showed excessive wear, resulting in higher particle emissions. Both aramid fibres and graphite demonstrated low CoF and low particle emission values. In contrast, the pads with steel fibres had high particle emissions for both PM2.5 and PM10 compared to the reference brake pads.

Nogueira et al. [110] examined the impact of different percentages of phenolic resin (4.5%, 6.5%, and 8.5% by weight) on wear and particle emissions. Their findings indicated that the friction material containing 6.5% phenolic resin produced the most favourable results, as the resin had a direct impact on the integrity of the friction material. This also positively influenced the development of the tribolayer, which is formed from wear debris

Candeo et al. [111] investigated the bedding-in behaviour and its impact on the friction layer, CoF and particle emissions. They found that during the bedding-in process, wear gradually increases as wear particles become initially trapped between the brake pad and rotor, forming a tribolayer. The development of this tribolayer is a dynamic process. When the tribolayer breaks down, the trapped particles are released, and some become airborne, leading to an increase in particle emissions. After the bedding-in procedure, the CoF values stabilise, and particle emissions also begin to decrease and reach a stable state. It is believed that the increase in wear and the subsequent decrease in particle emissions are due to the development of secondary plateaus.

Gramstat et al. [112] investigated particle emission from a low-steel and a copper-free Non-Asbestos Organic (NAO) brake pad material rubbing on a GCI rotor. It was found that brake emissions are not only dependent on the coefficient of friction but also on other factors such as temperature, brake pressure and the friction material used. The copper-free NAO pad material produced greater numbers of particles during high-demanding braking tests compared to the low-steel pad material.

Mancini et al. [113] investigated how different brake cycles can affect the chemical composition of brake wear particle emissions. It was found that a more demanding brake cycle produced more brake emissions, such as iron oxides, than the less demanding brake cycle.

Hesse et al. [114] studied the particle emission of different disc brake materials, focusing on particle emissions during the bedding-in procedure and temperature observations. At the start of the bedding-in procedure, particle emissions were particularly high but then started to decrease. This is likely due to the protective coating being removed from the brake disc. Also, surface topography was not yet uniform and the tribolayer had not been fully formed during the initial bedding process. Hesse et al. also found that if a critical threshold temperature is exceeded during braking, this can lead to the formation of more nanoparticles being emitted.

Studies have not been limited to GCI brake rotor material but other novel materials in hopes of reducing brake dust. Lyu et al. [115] investigated the emissions from three types of brake rotors: GCI, high-velocity oxygen fuel (HVOF), and laser cladding. They found that the ultrafine particle emissions from the HVOF brake rotor differed significantly from those of the GCI and laser-cladded rotors. The HVOF rotor emitted needle-shaped particles, while the GCI and laser-cladded rotors produced round and flake-shaped particles. Asmawi et al. [19] conducted a preliminary study on particle emissions from a GCI rotor and a novel PEO-coated aluminium rotor. They discovered that the PEO-coated rotor emitted fewer particles in both number and mass compared to the GCI rotor. However, the performance of the PEO-coated rotor was less consistent and exhibited a lower CoF compared to the GCI rotor. This inconsistency is believed to be due to the unoptimized friction material used in the PEO-coated rotor.

Studies on brake emissions focus not only on quantifying the amount of emissions produced but also on their health effects. A study by Selley et al. [116] compared the toxicity of brake dust and diesel particles using a cellular model relevant to human airways. The findings revealed that, despite differing chemical compositions, both brake and diesel particles had similar effects. Notably, the researchers observed that metals, which are key drivers of toxicity, were present. Some brake pads contain metal fibres, and the majority of brake rotors are made from metal. Grigoratos et al. [36] noted that the most common metals found in brake pads are iron, copper, zinc, and lead. Additionally, it has been reported that some of the elements found in brake materials pose dangers to human health and the environment.

2.8 Corrosion of friction brakes

A vehicle's brake system is intentionally designed to be exposed to the environment to allow for airflow, which helps cool the system. However, this exposure can lead to potential harm or damage, particularly in areas with high rainfall. In such locations, moisture, freezing conditions, and humidity can accelerate corrosion. Rainwater can contribute to this issue, especially if it is slightly acidic, as its acidity can increase the rate of corrosion.

Freezing temperatures can result in icy roads, and de-icing methods often involve using chemical salts like sodium chloride, magnesium chloride, and calcium chloride. These salts can significantly influence the rate of corrosion. For corrosion to occur, an electrolyte must be present in the solution, and the presence of sodium, magnesium, and calcium, which are all electrolytes, enhances the electric current.

Additionally, salt is hygroscopic, meaning it attracts and absorbs water and moisture from the surroundings. When salts are absorbed in water, they create a concentrated chloride solution, which is highly corrosive and can lead to the formation of corrosion pits in metals, even those with protective coatings [15], [17], [117].

Corrosion can affect the material properties, such as causing the material to lose its strength, which can result in the degradation of the material. In the case of ferrous metals and alloys such as iron and steel alloys, corrosion can cause and lead to catastrophic failure. However, this is not always the case in corrosion. In some cases, corrosion can be desirable, for example, the oxide layer can have increased strength and improved the corrosion resistance over the substrate material. Example of this include is aluminium, copper, chromium and nickel, as when these materials oxidise it forms an adherent oxide layer on top the surface material. This oxide layer acts as a hard protective layer, which is used to protect the substrate material reducing the rate of corrosion [118]. Therefore, corrosion cannot be defined as the deterioration of a metal or an alloy. A report by Heusler. [119] defined corrosion as “Corrosion is an irreversible interfacial reaction of a material with its environment which results in consumption of the material or dissolution into the material of component of the material”. This definition includes both the positive and negative effects that corrosion can have on a material.

The common brake disc material used in most commercial vehicles is grey cast iron [76]. Grey cast iron is known to have good thermal and mechanical properties, however, it is also known to be corrosive [120]–[122]. Corrosion of a grey cast iron brake can pose a potential problem as this can lead to the degradation of the material, performance issues and NVH.

Montasell et al. [34] investigated vehicle judder due to corrosion of a cast iron brake rotor. It was observed that most of the corroded layer on the brake rotor was removed after the first snub test. However, even after the completion of the 3rd snub test, there were still traces of corrosion on the rotor. Cho et al, [123] also investigated the correlation between corrosion and brake judder. This study showed that a brake disc with a thicker oxide layer showed higher brake torque variation (BTV) compared with the brake disc with a thinner oxide layer. Therefore, they concluded that an oxide layer formed on the brake disc surface has a strong influence on the BTV.

Hamid et al. [124] investigated the frictional characteristics of a corroded grey cast iron brake disc. This study used two different brake pad materials with different material compositions against two GCI brake discs. The brake underwent a burnishing procedure to transfer some of the friction material onto the surface of the brake discs, after which both brake discs underwent a corrosion process. The results showed that the concentration and thickness of the oxide layer formed on the two burnished brake discs were different. Thus, the composition of the friction material is a factor in the formation of corrosion on the surface of the brake rotor. Montasell et al. [34] also concluded that the thickness of the corroded layer on the brake disc is affected by the material composition of the transfer layer that has been developed on the brake disc surface.

Gulden et al. [125] also looked into the impact that corrosion has on the PEO-coated aluminium brake rotor. It was found that the weak aluminium substrate material caused the opening of cracks in the coating during repeated braking at high temperatures due to the differences in thermal expansion between aluminium and the coating. It was also found that the cracks allowed for the brake dust to fill them, which can lead to further damage to the coating. This depends on whether the brake dust is material contains any metal particles, which could corrode.

Motta et al. [126] investigated corrosion stiction, a phenomenon where brake pads and rotors develop a strong adhesion. This unwanted adhesion can lead to the degradation of both the friction material and the brake rotor, impacting brake performance and potentially causing NVH issues. The study found that friction materials containing copper are more likely to develop galvanic corrosion. Additionally, this corrosion affects the compressibility and stiffness of the friction material, which can influence the contact area between the brake pad and rotor.

2.9 Identification of Knowledge Gaps

In recent years, there has been an increase in research focused on brake wear emissions, largely influenced by the introduction of non-exhaust emission limits in the upcoming Euro 7 legislation. One of the most widely studied methods for reducing brake wear emissions is the use of hard surface coatings on brake rotors. While significant research has already been undertaken in this area, the automotive industry's transition from ICE vehicles to BEVs presents new opportunities and challenges.

Regenerative braking in BEVs offers a potential benefit by decreasing reliance on the friction braking system, which can lead to a reduction in overall brake wear emissions. This change allows for the exploration of alternative lightweight rotor materials that were previously overlooked due to concerns about thermal performance. However, the reduced use of friction brakes in BEVs introduces a new issue: the infrequent application of brakes can lead to corrosion accumulating on the rotor surface. As the surface of the rotor is not being cleaned during braking.

There is a notable gap in the existing literature regarding the relationship between brake wear emissions and corrosion. Previous studies have mainly focused on characterising brake wear emissions from uncoated and coated GCI rotors or on understanding the effects of corrosion on mechanical and chemical properties. Very limited research has directly examined how corrosion impacts brake wear emissions. Additionally, little to no work has been done on investigating alternative lightweight materials in the context of both brake wear emissions and corrosion resistance. Addressing these gaps is crucial for developing more efficient, sustainable, and future-ready braking systems and is therefore the main topic of this thesis.

Chapter 3

Experimental Equipment, Materials and Methodology

"Victory is changing the hearts of your opponents by gentleness and kindness."

Salahuddin ibn Ayyubi

3.1 Introduction

This chapter provides a detailed description of the experimental test rigs, including the brake dynamometer and the salt spray chamber. It provides detailed information on GCI, Al-MMC and PEO-Al brake rotors and friction materials selected for this project. An explanation of the drag testing procedures for brake testing and ASTM-B117 corrosion test procedure. The methods for measuring brake wear, such as airborne, dimensional, and gravimetric loss, are detailed. Additionally, the chapter discusses the post-test analysis techniques used to evaluate the friction materials.

3.2 Brake dynamometer ducting and emissions measurement system

This project used a full-scale brake dynamometer to conduct the brake tests. The brake dynamometer is located at the University of Leeds (UoL) and is equipped with a particle extraction system designed to collect brake emissions.

The UoL brake dynamometer, shown in Figure 3.2a, consists of an inlet duct, an air-tight enclosure, an outlet pipe, a Dekati ELPI+, and a 45 kW DC motor (Leroy Somer LSK1604M04 45), capable of turning the brake rotor at speeds up to 1500 rpm. Figure 3.2b provides a side view of the brake dynamometer without the guards, exposing the shaft. As seen in Figure 3.2b, the 45 kW DC motor is connected via a belt to the shaft, which drives the brake disc. Torquemaster TM 23 torque transducer in-line a maximum torque rating of 500 Nm is installed within the shaft to measure the braking torque. The Torquemaster also measures the rotational speed of the shaft.

The CoF value is calculated using Equation 3.1, which uses the applied pressure and measured torque output as described by Wei-Yi et al. [127].

$$\mu = \frac{(T/R_{effective})}{(2 * P * A_{piston})} \tag{3.1}$$

Here T is the brake torque, which is measured by the brake dynamometer, $R_{effective}$ is the effective or mean radius of the friction ring of the brake rotor. P is the brake line pressure and A_{piston} is the total calliper piston area.

The prototype brake calliper and control system for the brake dynamometer were designed by a previous student [33], [128]. The brake calliper shown in Figure 3.1 is a prototype 4-piston calliper, that allows individual piston pressure control and is modular to allow for different brake rotor sizes. The calliper was developed to suppress brake squeal by varying the leading and trailing piston pressures [128]. The user interface and data acquisition (DAQ) program were developed using LabView. This program independently controls the shaft's rotational speed and the brake line pressure.

Figure 3.3 shows the inside of the brake enclosure. Connected to the brake enclosure are the inlet duct and the outlet duct which are described below. Inside the brake dynamometer enclosure, the prototype brake calliper, a brake disc, and two rubbing thermocouples are shown.

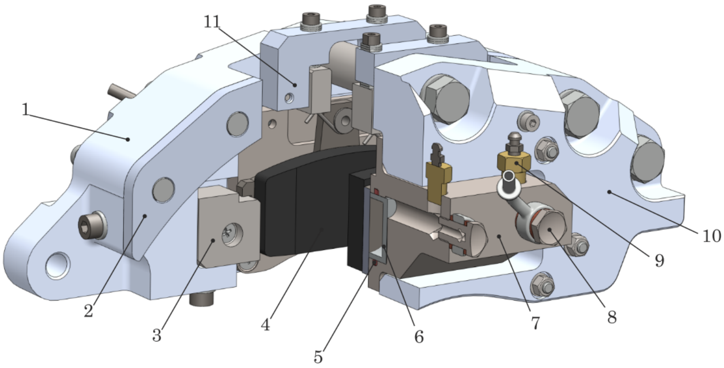

Figure 3.1: Main components of the calliper assembly: 1) calliper body, 2) abutment, 3) brake pad, 4) piston module, 5) pad pre-load assembly [128]

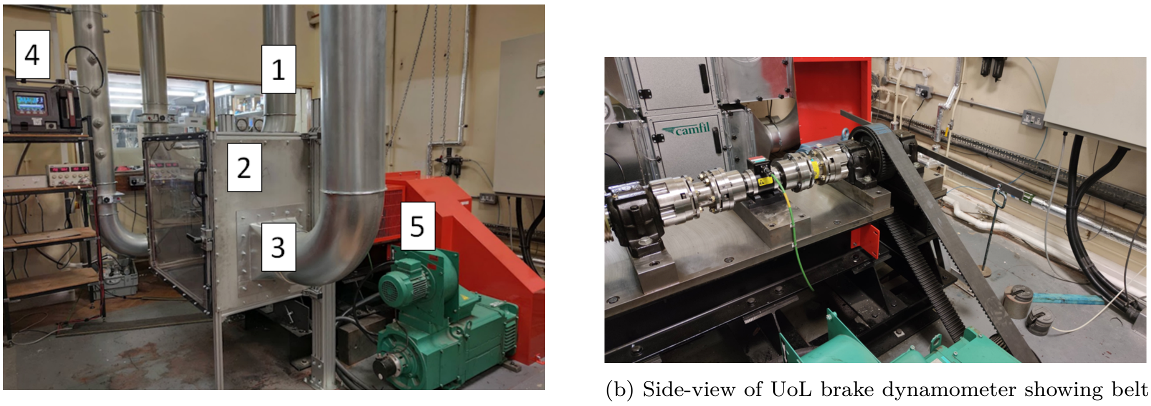

(a) UoL brake dynamometer and ducting system.
1) Intlet duct. 2) enclosure. 3) Outlet duct. 4) Dekati ELPI+. 5) 45kW DC motor.

(b) Side-view of UoL brake dynamometer showing belt drive and torque transducer

Figure 3.2: UoL brake dynamometer

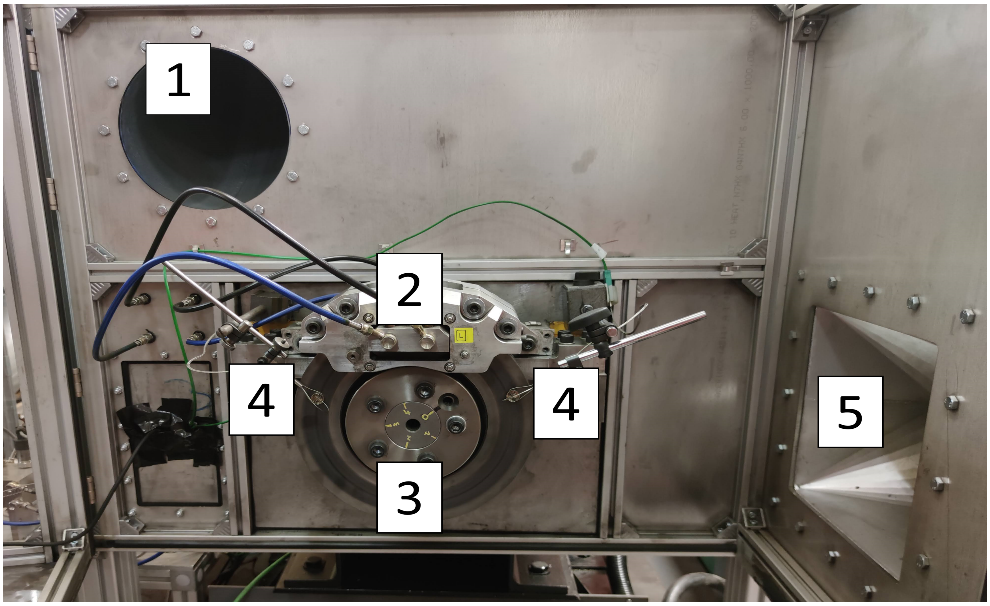

Figure 3.3: Brake enclosure: 1) Inlet pipe. 2) Brake calliper. 3) Brake disc. 4) Thermal couples. 5) Outlet duct

3.2.1 Brake dynamometer ducting system

The hinged brake enclosure which covers the brake system, see Figure 3.2a, constructed from aluminium with Perspex window. When closed the enclosure is air-tight, preventing the laboratory air from leaking inside and contaminating the air inside the enclosure.

Connected to the enclosure are inlet and outlet ducts, where fresh air from the laboratory is drawn into the enclosure and then exhausted through the outlet pipe. A high-efficiency particulate absorbing (HEPA) H14 filter is used to filter the incoming air, reducing the risk of contamination. The outlet duct is also equipped with HEPA H14 filters, and for additional safety, a carbon-activated filter is used to remove any strong odours and harmful gases. The cylindrical ducting pipes, made from galvanised steel sheets as shown in Figure 3.3, have an internal diameter of 225 mm.

A 4 kW fan is used to draw air downstream of the brake inside the enclosure. To control the air speed through the ducting system, which can be adjusted from 6 to 15 m/s. Four tapping and velocity test points are situated along the outlet duct to allow for the collection of wear emissions and to measure the airspeed through the ducting system, as shown in Figure 3.4. An anemometer is used to measure the airspeed in the ducting system.

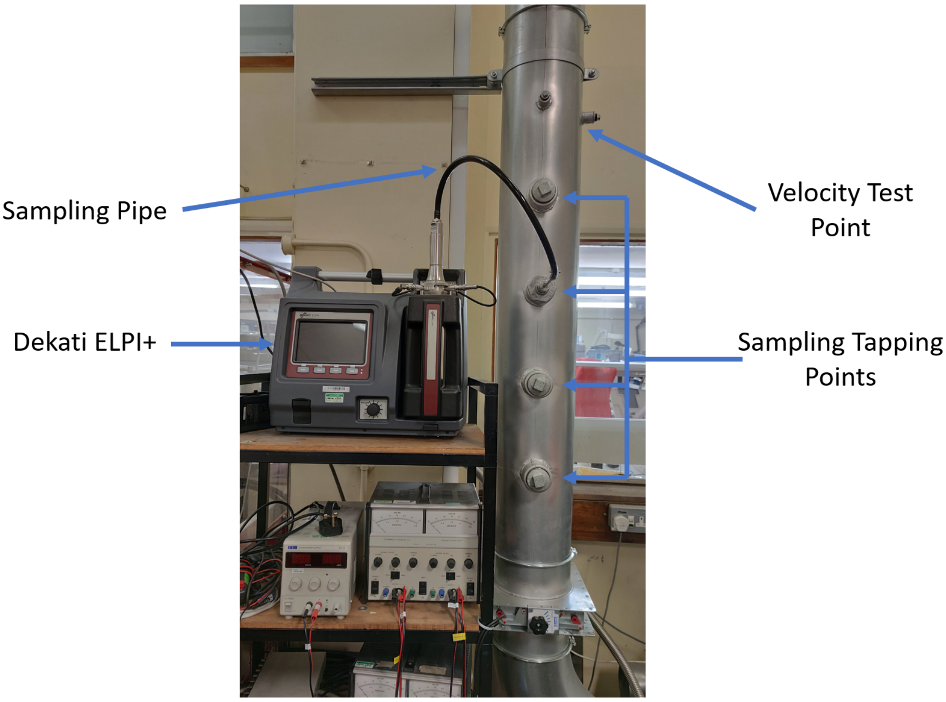

Figure 3.4: Brake dynamometer outlet duct

Achieving isokinetic conditions is important for collecting emissions. Isokinetic conditions occur when there is no divergence of flow around the sampling probe. The velocities of the sampling nozzle and the sampling stream must be equal. If the velocities are too low or too high, there is a risk of under-collection or over-collection of particles [129]. Therefore, an isokinetic sampling concept was employed to ensure an accurate collection of particle wear emissions and avoid biased results and errors in the sampling probe, with the volume flow rate tailored accordingly.

Consequently, two CFD analyses were carried out by a pervious PhD student at the UoL: 1) airflow around the brake dynamometer ducting system, and 2) a detailed simulation of a selected section of the ducting containing the sampling probe [130].

The airflow inside the enclosure, where the brake system is housed, was shown to be complex and extensively mixed. As the airflow enters the enclosure, it splits into two streams, one above and one below the brake system. The two streams interact and mix as the airflow moves towards the outlet duct. A validation study was conducted to compare the CFD results with the experimental system. This involved comparing the velocity profiles of the CFD and experimental data at the same locations in the outlet ducting. The results indicate good agreement between the experimental and simulation results.

The sampling probe is positioned inside the outlet duct, aligned parallel to the free-stream air. The probe is constructed from standard thin-walled 316L stainless steel seamless tubing. The internal diameter ***(d)*** of the probe was determined using equation 3.2, where $\dot{V}$ is the airflow rate in m^3/s and v is the mean velocity at the inlet of the probe in m/s [131]. Based on this equation, the chosen tube had an outer diameter of 6.35 mm and a wall thickness of 0.4064 mm, giving an internal diameter of 5.537 mm, which is within the required limits. When the air velocity at the centre of the ducting is set to 6.92 m/s, the mean velocity within the probe inlet is also set to 6.92 m/s. Figure 3.5a shows all the dimensions of the sampling probe used in this study.

$$d = \sqrt{\frac{4\dot{V}}{\pi v}} \tag{3.2}$$

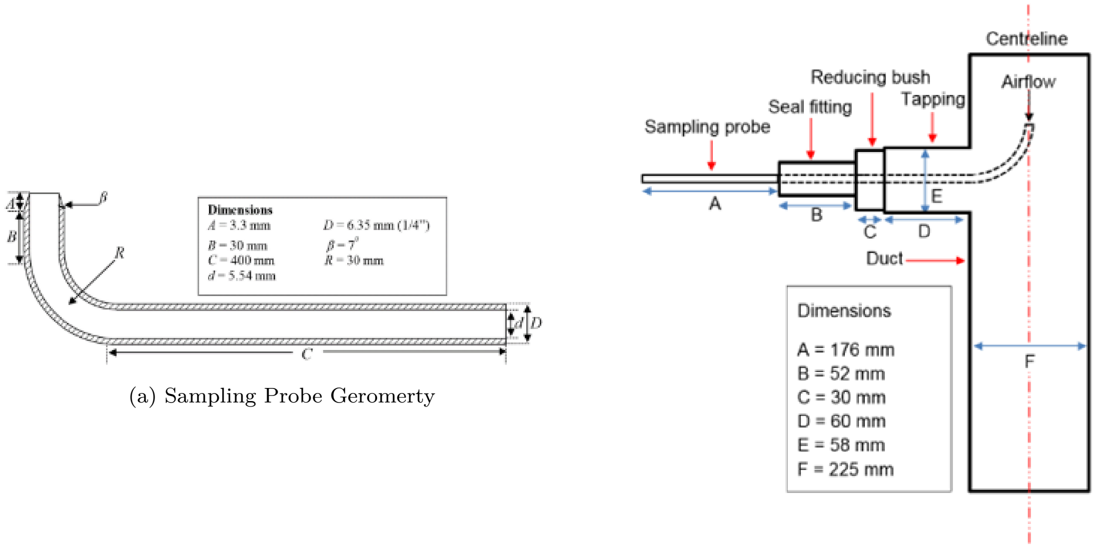

(a) Sampling Probe Geromerty

(b) 2D drawing of fitting sampling probe into the outlet duct

Figure 3.5: Sampling probe [131]

3.2.2 Particle emissions measurements

A Dekati Electrical Low-Pressure Impactor (ELPI+) instrument is used to measure the particle number and mass of brake wear emissions. The Dekati ELPI+ shown in Figure 3.4 is a particle measurement device capable of measuring both the number and mass of airborne particles in real time. The ELPI+ is a cascade impactor that consists of a 14-stage impactor, with an aerodynamic particle size range from 6 nanometres (nm) to 10 micrometres (µm). Additionally, the Dekati ELPI+ includes a 15th stage, used as a pre-separator stage, which is the first stage in the cascade impactor designed to remove particles larger than 10 µm. The 14 stages of the Dekati ELPI+ are impactors, and the final stage, for the smallest particles, is a filter stage. Each of the 14 impactor stages is constructed from three parts: a PEEK™ insulator ring with two O-rings, a jet plate, and a collection plate. Figure 3.6 shows the breakdown of one impactor stage.

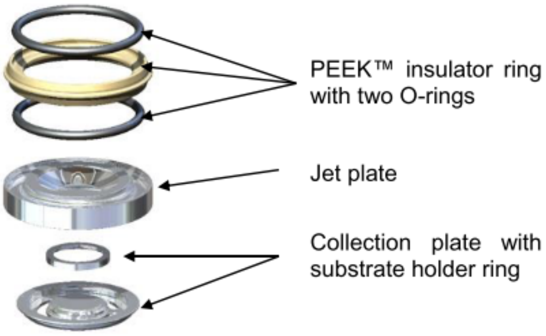

Figure 3.6: Construction of one impactor and filter stage [132]

The PEEK^{TM}insulator ring and two O-rings are used to insulate each impactor stage, as all 14 of these stages have electrical detection. This insulation is essential for measuring the particle mass and number at each stage in real-time. When airborne particles enter the Dekati ELPI+, they are electrically charged to a known level by a corona charger. The impactor stages are electrically insulated to isolate them, aiding in determining the number concentration of the particles in each stage. As the electrically charged airborne particles are collected on an impactor stage, they produce an electrical current recorded by an electrometer. This current is directly proportional to the number concentration of the particles and so can give a real time output of this number at the data acquisition system. The mass of particles collected at each stage can be measured by subsequent gravimetric analysis.

Airborne particles are separated by their aerodynamic particle size by the jet plates. At each stage in the cascade, the impactor jet plates have nozzles that help separate the particles according to their aerodynamic size. These particles land on the collection plate equipped with a collection substrate or foil.

The foils should be 25 mm in diameter, 0.1 mm thick, and poreless. The foil materials can be either aluminium or polycarbonate. Aluminium foils are used for gravimetric measurements, while polycarbonate foils are used for chemical analysis. The foils must be greased to prevent particle bouncing during collection. The grease should have low evaporation properties, even under low pressures, and high viscosity to ensure it remains on the foils. Apiezon-L is recommended due to its purity and low evaporation properties.

A 25 mm circular hole punch is used to cut collection substrates or foils from household aluminium foil, as shown in Figure 3.7. The Apiezon-L grease is dissolved in toluene solvent to allow for the grease to be spread on the aluminium foils. It is recommended to add the toluene solvent drop by drop to dissolve the Apiezon-L grease until the liquid becomes nearly opaque. Once the Apiezon-L grease has dissolved into an opaque liquid, a clean fine brush is used to spread the grease on the foils. It should be noted that the edges of the foils should be kept clean and free from grease, as this part of the foil will be fixed to the collection plate by the substrate holder ring. Once the foils have been greased, they should be set aside to allow the solvent to evaporate, leaving the grease behind. The preparation and greasing of the foils should be carried out in a fume cupboard with appropriate PPE, as hazardous chemicals are involved.

Figure 3.7: Dekati ELPI+ aluminium foil and collection plate [132]

The Dekati ELPI+ requires regular maintenance and cleaning to ensure the instrument functions properly. It is recommended to clean the Dekati ELPI+ on a weekly or monthly basis, although this frequency may vary depending on usage frequency and issues such as zeroing errors, unstable readings, or leaks.

To clean the cascade impactor, it must first be removed from the ELPI+ housing. This involves loosening two impactor tightening screws, disconnecting the zero air pump hose, the charger high voltage, and the trap BNC connectors. The impactor cover, which houses the pre-selector stage containing the corona charger, must also be slid out to expose the cascade impactor. Once the impactor cover is removed, all 15 stages of the cascade impactor are exposed Figure 3.8. Note that stage 15 is only a collection plate. The used foils should then be removed from the impactor collection plates.

Figure 3.8: Removing the impactor cover [132]

All parts of the cascade impactor can be cleaned in an ultrasonic bath, except for the O-rings and the filter stage. A suitable hydrocarbon-based solvent, such as a 50:50 mix of isopropanol and deionized water used in this project, is added to the ultrasonic bath. The disassembled impactor is placed in the ultrasonic bath for 30 minutes and then left to dry. During cleaning and drying, lint-free wipes or tissues can be used, but it was found that some fibres could remain in the impactor stages. Therefore, only compressed air was used to ensure thorough cleaning and drying of the impactor in the present work.

3.3 Salt spray cabinet

The C&W salt spray cabinet, type SF100, is shown in Figure 3.9. The equipment also contains a 114-litre capacity reservoir, shown in Figure 3.9a, which stores the salt solution. Inside the cabinet, shown in Figure 3.9b is an atomising tower from which the salt solution is sprayed.

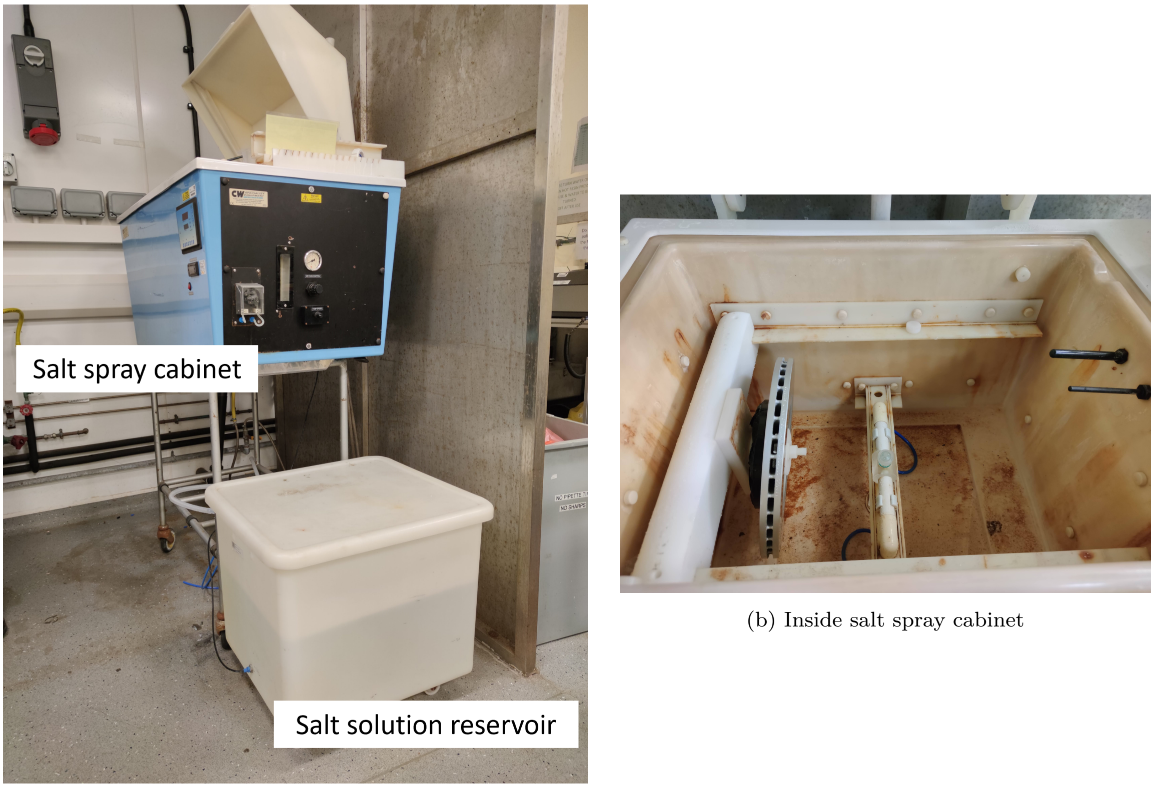

(a) C&W salt spray cabinet and salt solution reservoir

(b) Inside salt spray cabinet

Figure 3.9: Salt spray cabinet

The salt corrosion cabinet is constructed from glass-reinforced plastic in two parts: the outer and inner shells. The blue outer shell, or outer cabinet, houses the control panel, control chassis, humidifier tower, flowmeter, peristaltic pump, pump speed adjuster, and service input panel, as shown in Figure 3.10. The inner cabinet, which sits within the outer cabinet, contains the heater panels.

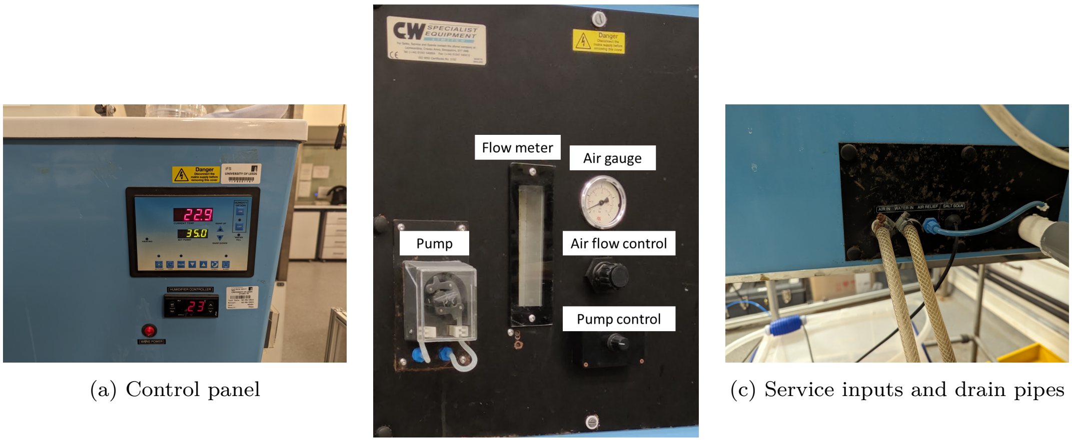

(a) Control panel

(b) Pump and airflow controls and gauges

(c) Service inputs and drain pipes

Figure 3.10: Salt Spray inputs and outputs

Before operating the salt spray cabinet, all pipes should be connected, which consists of air in, water in, salt solution, and drain, as seen in Figure 3.10c. It is necessary to have an air ventilation pipe since the SF100 is capable of generating fog. A T-tube is connected to the waste/drain, allowing for a vertical tube for venting and a horizontal flexible hose pipe to the drainage.

The salt reservoir container is filled with a more than sufficient amount of the desired salt solution. This is to accommodate any increase in the flow rate of the salt solution and to prevent air from being unexpectedly drawn into the cabinet, as the tube connected to the salt solution reservoir container does not sit flush at the bottom but is positioned a few millimetres above it. Intake of unnecessary air or disruption of the flow rate can impact the fog density, collected solution, and pH levels.

When placing the brake rotor into the salt spray cabinet, it mustn't obstruct the nozzle spray path, as this can affect the flow rate and coverage inside the cabinet. It should be noted that this model consists of only one jet nozzle. A water seal is also required around the edge of the lid when closed. This prevents any fog and heat from escaping during the test, allowing consistent fog and humidity levels to be maintained.

When operating the salt spray cabinet, the temperature, humidity, and timer can be found on the control panel, as shown in Figure 3.10a. To control the airflow and pump speed, these controls are located on the side of the salt spray cabinet, as shown in Figure 3.10b. It should be noted that the brake rotor is only placed into the salt spray cabinet after the set environmental conditions are met.

To measure the pH of the solution, the Orion^{TM} Triode^{TM} 3-in-1 pH probe and Orion Star^{TM} benchtop pH meter were used, see Figure 3.11. The Orion^{TM} Triode^{TM} pH probe is equipped with built-in temperature sensors, enabling pH adjustments based on the solution's temperature to ensure more accurate readings.

(a) Orion^{TM} Triode^{TM}

(b) Orion Star^{TM} benchtop pH meter

Figure 3.11: pH probe and meter

The density of the salt solution before and after atomization was measured using a hydrometer (Figure 3.12a). One challenge encountered was finding suitable labware compatible with the small volume of collected solution and the length of the hydrometer. To address this issue, custom-made labware (Figure 3.12b) was created.

(a) Hydrometer

(b) Hydrometer tube

Figure 3.12: Measurement devices for density of salt solution

3.4 Materials

Three different brake rotor materials were used in this study: grey cast iron (GCI), aluminium metal matrix composite (Al-MMC), and a Plasma Electrolytic Oxidation (PEO) ceramic-coated aluminium alloy (PEO-Al) brake rotor. The brake dynamometer is configured for a Rover 75 brake rotor. The GCI brake rotor used is a commercial product obtained from an aftermarket store, specifically the Ferodo DDF1080C model. This front vented rotor has an outer diameter of 284 mm and a cheek thickness of 22 mm. Figure 3.13a displays a new Ferodo GCI brake rotor, which is covered by a protective coating applied by the manufacturer. This zinc and aluminium mixture coating protects the disc against corrosion during storage [133].

The available brake calliper used in this project was the prototype brake calliper shown in Figure 3.1. This calliper was designed to house Lancia Delta brake pads, which means the friction material or brake pad is from Lancia Delta. Similar to the GCI rotor, the brake pads are off-the-shelf products. The brake pads, shown in Figure 3.13b, were manufactured by MACPO and are semi-metallic.

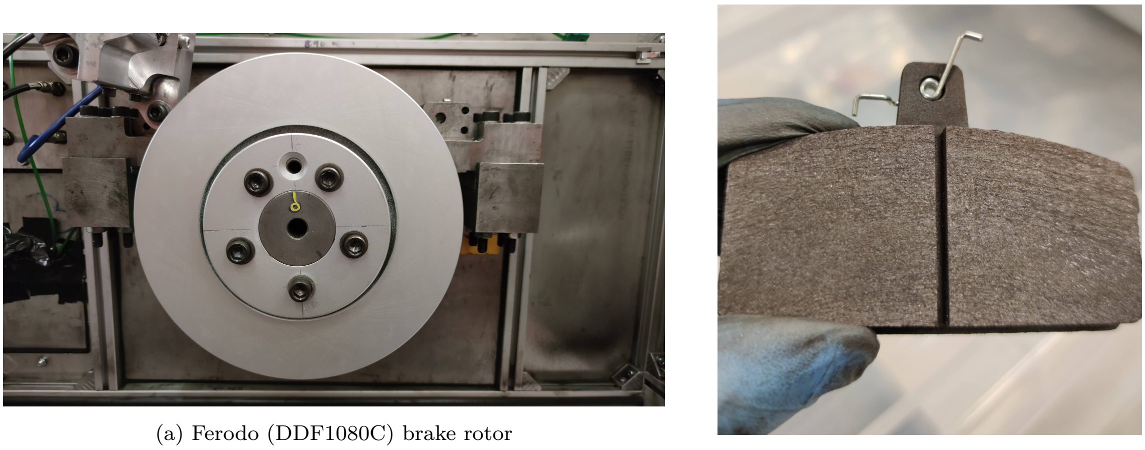

(a) Ferodo (DDF1080C) brake rotor

(b) MACPO Lancia Delta brake pad

Figure 3.13: Brake pad and rotor used in the GCI study

The Al-MMC brake rotor shares its overall geometric parameters with the GCI brake from the Rover 75 vehicle, both having a diameter of 284 mm. The Al-MMC prototype brake rotor consists of a cast aluminium alloy matrix reinforced with 30% SiC (silicon carbide) particles. Figure 3.14 illustrates that, compared with the Rover GCI rotor, the cheek thickness has been increased to enhance thermal inertia, thereby restricting temperatures during repeated high-speed braking [134].

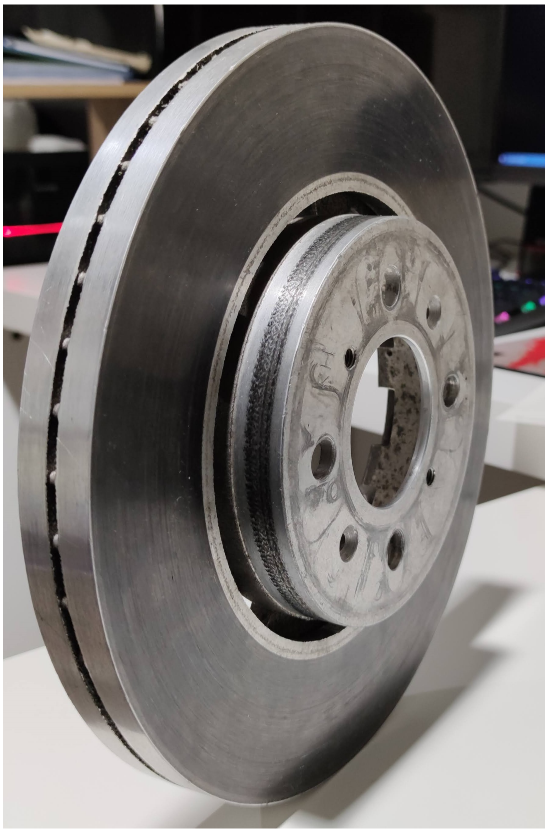

Figure 3.14: Image of aluminium metal matrix composite (Al-MMC) brake rotor

The prototype PEO-Al rotor used in this study was machined from a wrought AA6082 billet into three pieces: two rubbing surface cheeks (one outboard cheek integral with the bell) bolted together with a separate ventilation ring, as depicted in Figure 3.15a. This unique three-piece design was conceived to facilitate easy modification of the vent configuration by simply machining a new ring. Figure 3.15b shows the PEO rotor mounted on the UoL dynamometer before testing. The white/grey surface visible on the brake rotor is the PEO coating. The PEO coating was selectively applied only to the friction surfaces and not the entire brake rotor. This approach maximises heat convection from all uncoated surfaces of the rotor, including the vents, in addition to heat conduction via the hub-shaft mount. A previous study by Alnaqi et al. [135] found that coating the entire brake rotor limits heat dissipation and traps it inside the rotor. More details of the PEO process will be discussed in Chapter 6.

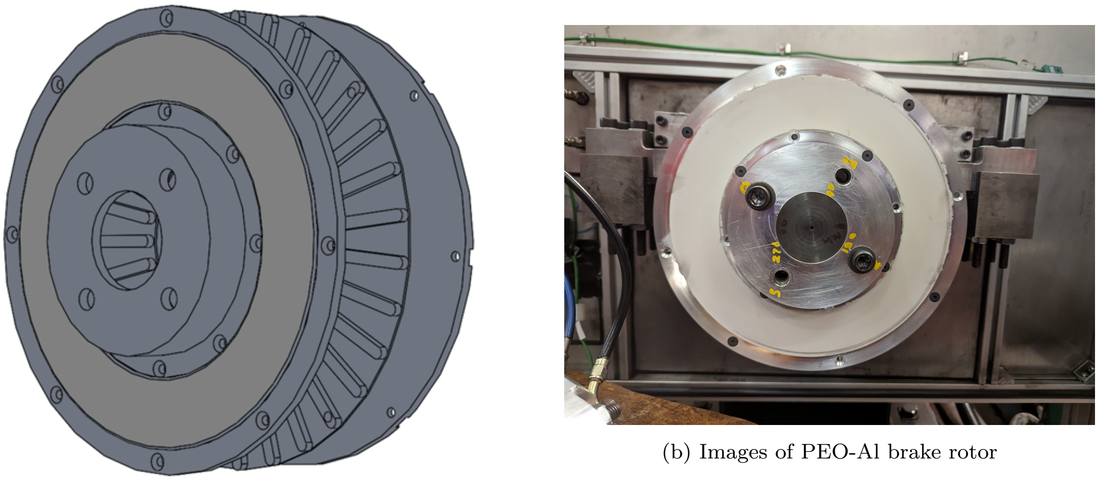

(a) 3D model of PEO-Al brake rotor in exploded view

(b) Images of PEO-Al brake rotor

Figure 3.15: Brake pad and rotor used in the GCI study

The brake pads selected for both the Al-MMC and PEO-Al rotors are aftermarket pads designed for the Lotus Elise S1 sports car, which was originally equipped with Al-MMC brake rotors. These pads use a special formulation reinforced with glass fibre and were specifically developed for use with Al-MMC rotors.

As the brake pads were designed to fit the Lotus Elise S1 brake calliper, some modifications were necessary to ensure compatibility. The rear brake pad from the Lotus Elise S1 is similar to the brake pads for the Lancia Delta, as shown in Figure 3.16a. However, the backplate required modification, trimming the fins of the backplate to ensure the brake pads fit properly inside the calliper, as depicted in Figure 3.16b. Table 3.1 gives an overview of the different brake rotors' dimensions and the friction material they are tested with.

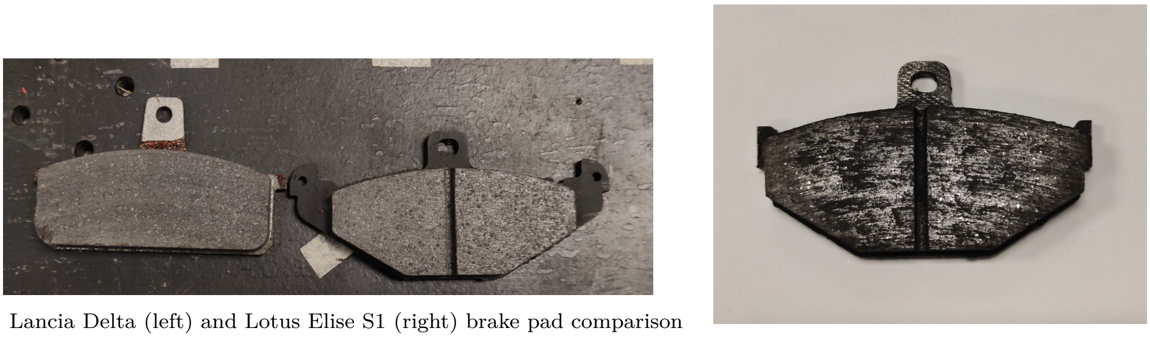

(a) Lancia Delta (left) and Lotus Elise S1 (right) brake pad comparison

(b) Image of Lotus Elise S1 brake pad cut to fit inside brake calliper

Figure 3.16: Lancia Delta and Lotus Elise S1 brake pad size comparison

Table 3.1: Brake rotor dimensions and brake pad selection

Materials	Dimensions (mm)	Mean friction ring (mm)	Brake pad
GCI	284 X 22	254	GCI pad
Al-MMC	284 X 26	254	MMC pad
PEO-Al	280 X 25	250	MMC pad

3.5 Testing Protocol

3.5.1 Brake dynamometer

The chosen brake duty cycle for these comparative brake tests is steady-state drag braking, simulating a vehicle maintaining a constant speed on a long downhill gradient in order to achieve near steady-state temperature conditions [26]. This cycle differs from other duty cycles such as WLTP, Mojacar, LACT, AK Master, and others. It was selected partly due to the non-inertial nature of the current Leeds dynamometer and also to facilitate comparative tests under near-steady-state tribological conditions, including a constant sliding speed and hydraulic pressure, as well as a near-constant surface temperature.

3.5.2 Corrosion conditions

Preparation salt solution

The ASTM B117-11 [136] standard has been chosen for salt spray testing in this study. This document provides a standardised methodology to simulate a controlled corrosive environment using a salt spray cabinet or chamber.

According to ASTM B117, the preparation of the salt solution requires 5 ± 1 parts by mass of pure sodium chloride salt (NaCl) and 95 parts of water. NaCl salt was selected for its high purity and absence of anti-caking agents, as specified by the standard. Deionized water was used for preparing the salt solution. To determine the amount of salt needed, a common formula is used: 0.053 x Mass of Water (g) = Mass of NaCl (g). For instance, to prepare 50 litres of water, 2.65 kg of salt is required following this formula.

Operation conditions

According to ASTM B117, the salt solution in the salt spray chamber must be maintained at a temperature of 35°C ± 2°C. The humidity inside the chamber should be kept at 95% ± 5%, with a spray or collection rate ranging from 1 to 2 mL per hour. Measurement of the collection rate is done using a measuring cylinder attached to a funnel via a rubber bung or stopper. Two such collection devices were positioned inside the salt spray chamber, see Figure 3.17. These devices not only measure the collection rate but also collect the atomized salt solution.

The collected salt solution is further analysed for specific properties such as sodium chloride concentration and pH. The pH of the collected solution should fall within the range of 6.5 to 7.2. ASTM B117 provides a specific density table (see Table 3.2) against which the collected solution should lie 5% ± 1% salt by weight density range.

(a) Collection device 1 (b) Collection device 2

Figure 3.17: Collection devices in salt spray chamber

Table 3.2: Temperature VS density [136]

Temperature	**Density, g/cm^3**		
°C (°F)	4% Salt	5% Salt	6% Salt
20 (68)	1.025758	1.032360	1.038867
21 (69.8)	1.025480	1.032067	1.038560
22 (71.6)	1.025193	1.031766	1.038245
23 (73.4)	1.024899	1.031458	1.037924
24 (75.2)	1.024596	1.031142	1.037596
25 (77)	1.024286	1.030819	1.037261
26 (78.8)	1.023969	1.030489	1.036919
27 (80.6)	1.023643	1.030152	1.036570
28 (82.4)	1.023311	1.029808	1.036215
29 (84.2)	1.022971	1.029457	1.035853
30 (86)	1.022624	1.029099	1.035485
31 (87.8)	1.022270	1.028735	1.035110
32 (89.6)	1.021910	1.028364	1.034729
33 (91.4)	1.021542	1.027986	1.034343
34 (93.2)	1.021168	1.027602	1.033950
35 (95)	1.020787	1.027212	1.033551
36 (96.8)	1.020399	1.026816	1.033146
37 (98.6)	1.020006	1.026413	1.032735
38 (100.4)	1.019605	1.026005	1.032319
39 (102.2)	1.019199	1.025590	1.031897
40 (104)	1.018786	1.025170	1.031469

Calibration

Initial test runs were conducted to monitor the spray rate and adjust it if too high or too low. Modifying the pump speed proved effective in controlling the spray rate. However, measuring the solution density and pH posed more challenges. Differences were observed between measurements taken before atomization and those taken after collection. Initially, the salt solution had a density indicating a salt concentration of 5% by weight. After atomization and collection, the salt concentration increased to nearly 6% by weight.

This increase in salt concentration can be attributed to the solution-heating process. Initially, the salt solution was prepared at room temperature (20°C), but the solution can reach temperatures exceeding 40°C during atomization. This elevated temperature causes some water to evaporate, thereby increasing the salt concentration. While this concentration remains within acceptable limits, an additional 10% of deionized water was added to the salt solution to mitigate this effect.

The pH of the salt solution posed another challenge, as it exhibited fluctuations before and after atomization. Deionized water as used in the solution, having been contained in a sealed unit and not exposed to air, tends to absorb carbon dioxide upon exposure, lowering the pH. Atomization further reduced the pH. Initially starting around pH 7, the solution was found to drop to approximately pH 6 after atomization.

To counteract this pH decrease, small increments of 5 to 10 mL at a time of 0.1 M sodium hydroxide were added to raise the pH. Typically, a drop of about 1 pH unit was observed upon atomization, necessitating adjustments to elevate the initial solution pH to around 8, ensuring it fell within the required range of 6.5 to 7.2 after atomization. Despite initial adjustments, the pH sometimes continued to decrease during testing, underscoring the need for regular calibration every 24 hours to check throughout the experiment.

Before and during the use of the salt spray cabinet, calibration tests and measurement checks were conducted. These include verifying the pH, specific density, and collection rate. Calibration tests were performed before the actual experiment and typically spanned

24 hours. This duration ensures sufficient solution collection and verifies the operational status of the salt spray cabinet.

3.6 Trial brake test

Before finalising the test methodology, trial tests were conducted on the GCI rotor to assess its overall brake performance and ensure that the procedure met the requirements. These preliminary tests involved varying brake line pressures (bar) and speeds (rpm). Initial tests were performed at 5, 10, and 15 bar pressures. Disc surface temperatures were measured using K-type rubbing thermocouples, located just before the leading edge and just after the trailing edge of the outboard brake pad.

Figure 3.18 illustrates the rubbing thermocouple results from the 15 bar test at 150 rpm. The test was abruptly stopped after 1500 s due to the surface temperature reaching over 400 $\circ$C. Disc temperatures above 400°C are undesirable, as this goes against the project's objectives of investigating normal (rather than extreme) braking conditions and may be too harsh on the friction couple. Notably, severe degradation of the brake pads was observed after this 15 bar test. Upon inspection, the pads had become denatured or charred [26], [133]. In light of this, the 10 bar brake line pressure was adopted as the highest pressure for all subsequent tests, replacing the previous 15 bar test. However, it was decided to add an intermediate pressure test of 7.5 bar to the test matrix to give the standard test protocol shown in Figure 3.19.

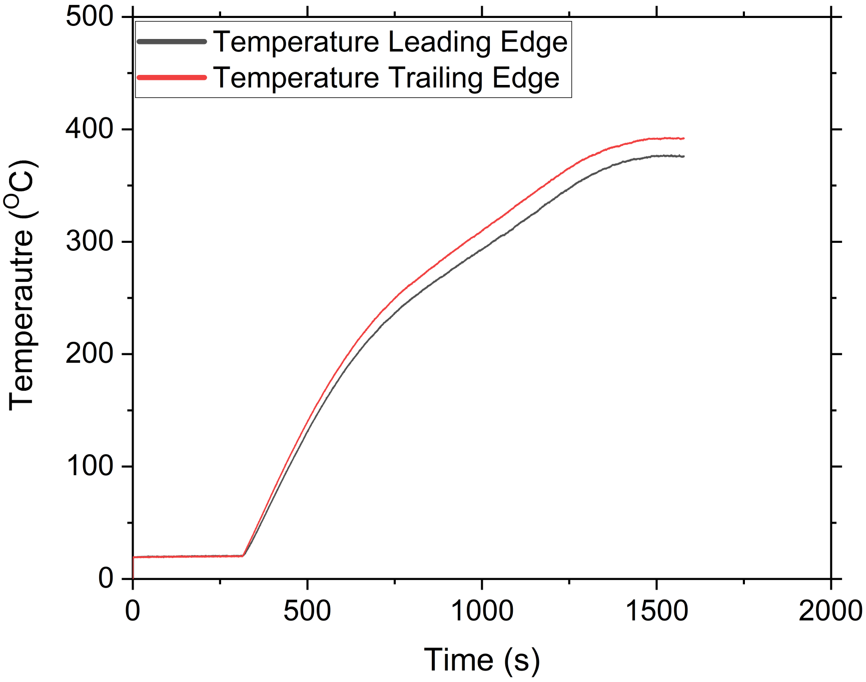

Figure 3.18: Disc surface temperature vs. Time of GCI brake test of 15 bar at 150 rpm

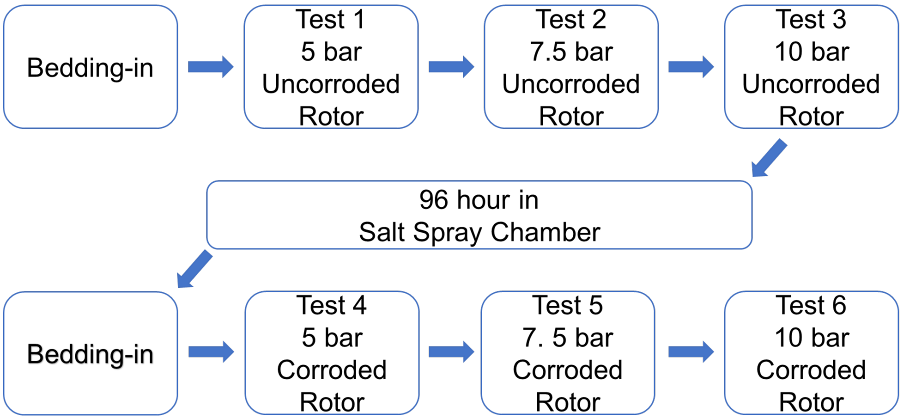

Figure 3.19: Test protocol

3.7 Standardised test protocol

3.7.1 Bedding-in procedure

The first step in this protocol is the bedding-in procedure, which is widely recommended for all brake testing to allow the friction surfaces to mate and form a tribolayer [114].

This procedure was adopted based on manufacturer recommendations for the initial use of new friction materials [137]. Details of the bedding-in procedure are listed in Table 3.3. During the first brake snub test, light braking is applied to gradually bed the surfaces together, avoiding excessive heat or pressure. The 30-second intervals of on and off braking simulate dynamic braking conditions. Once all 15 stops are completed and the brake rotor surface temperature reaches 30°C, the brake snub 2 test can commence. This consists of 15 braking cycles, similar to brake snub 1, but with intensified conditions: 2.5 times the braking line pressure with double the duration while maintaining the same rotational speed and cooldown times. The objective of brake snub 2 is to enhance the procedures initiated in Brake Snub 1 by increasing heat and wear within the brake system in order to further develop and stabilise the tribolayer and CoF.

Brake snub 3, also known as the heat cycle, marks the final phase of the bedding-in procedure. This involves raising the temperature within the brake system to allow any gases to escape from the brake pads. The rotor surface starting temperature as measured by a rubbing thermocouple is set at 30°C, with the brake released when the rotor temperature reaches 100°C. The temperature limit of 100°C is chosen to prevent excessive heat being generated that could potentially glaze the brake pads and discs.

3.7.2 Drag brake testing procedure

The braking conditions that were used in this study are a modified version based on the procedure developed by Asmawi [131]. Asmawi's test protocol was designed to simulate drag braking, resembling constant braking during a downhill descent such as the Grossglockner Alpine route. The test conditions aimed to achieve near-steady-state temperature and brake torque. Therefore, the test protocol involved controlling the brake pressure and rotational speed over a prolonged period. Three brake line pressures of 5 bar, 7.5 bar and 10 bar over 90 minutes. The rotational speed was set at 150 rpm. Assuming tyre dimensions of 245/45 R18, this corresponds to a vehicle speed of 19 km/h.

Table 3.3: Bedding-in procedure

Brake snub	Number of stops	Braking time (s)	Cooldown time (s)	Rotation speed (rpm)	Brake line pressure (bar)
1	15	30	30	200	2
2	15	60	30	200	5
3	8	Variable	Variable	150	5

The fan speed for the extraction system remained unchanged from Asmawi et al study [130], to give an average duct air velocity of 7 m/s, which corresponds closely to the air speed of 6.92 m/s required for isokinetic sampling conditions. More precise setting of the duct air velocity was not possible since this velocity represents only 5% of the total measurement range of the anemometer available for this study.

3.7.3 Emissions testing procedure

Before emissions testing can commence, the Dekati ELIP+ particle measurement device must undergo electrometer zeroing. To zero the Dekati ELPI+, the device should be powered on for at least thirty minutes before zeroing, and measurements should then be taken. The impactor pressure should be set to 40 mbar ± 5 mbar, the charger turned off, and zero air switched ON to allow clean air to flow through the impactor. Once the current values stabilise with no signal drift, zeroing can be initiated through the ELPI+VI software, which typically takes a few minutes to complete. Successful completion of zeroing is indicated by a message on the screen.

To verify successful zeroing, the zero levels should fall within acceptable limits of ±10 femtoampere (fA) based on raw current values with zero air activated. Once values are confirmed within this range and no current drift is observed, zero air is turned off to allow ambient air into the impactor, followed by turning on the charger. It is crucial to turn off zero air before activating the charger to prevent oxidation of the corona charger needle. With the charger operational, the Dekati ELPI+ is ready to measure particle emissions.

The sampling rate of the dekati was set at 1Hz.

Each drag braking application lasted 90 minutes to ensure steady-state conditions. Before initiating braking, no brake pressure was applied, and the shaft remained stationary for the first 5 minutes of each test. Just the extraction fan and Dekati ELPI+ were turned on in order to stabilise the airflow and record background particle measurements without any brake emissions. Subsequently, the motor was activated to rotate the brake rotor at 150 rpm without applying brake pressure for an additional 5 minutes. This step allowed airflow to stabilise further within the ducting system and verified the absence of brake drag. Following these pre-conditioning steps, the 90-minute drag braking test commenced.

After each 90-minute drag braking session, a 5-minute cool-down period was followed during which no brake pressure was applied. This period facilitated the measurement of any residual brake wear particles emitted post-braking. After each test, the Dekati instrument was halted and powered off to prevent additional particles from entering the impactor.

3.7.4 Corrosion testing procedure

As stated above, the corrosion test protocol adhered to the ASTM B117-11 standard [136]. This standard outlines controlled conditions for testing a variety of coated and uncoated materials in a corrosive environment. The salt solution first underwent calibration to ensure it met specified conditions as described above before introducing the rotor into the cabinet. Calibration testing lasted between 16 and 24 hours to monitor and verify the flow rate, pH level, and salt solution density compliance.

During the corrosion exposure of the brake rotor inside the salt spray cabinet, a separate collection device placed away from the rotor monitored pH levels every 24 hours to ensure they remained within the range of 6.5 to 7.2.

Before placing the brake rotors into the salt spray cabinet, the hubs were taped up to prevent corrosion or salt deposits from forming in that area, potentially affecting the rotor's runout when reattached to the shaft. Additionally, steel screws securing the three-piece rotor assembly were replaced with nylon screws, see Figure 3.20, to prevent corrosion contamination from metallic components.

Figure 3.20: Three-piece rotor with nylon screws and tape for corrosion cabinet

A custom-made holder was utilised to mount the brake disc in the cabinet, allowing the disc to be positioned at an angle of ± 15° from the vertical axis. This orientation facilitates runoff of the salt solution to prevent stagnant solution on the brake disc surface. After 48 hours, the brake rotor was reversed within the cabinet to ensure uniform corrosion deposition on both sides of the rotor. The hub of the brake rotor was taped off to protect it from the environment, simulating its protection when attached to a vehicle wheel [34].

Following 96 hours in the salt spray cabinet, the brake rotor was removed and left to air dry for 24 hours under normal laboratory atmospheric conditions before resuming dynamometer testing.

3.8 Post-test measurements and materials characterisation

In between each test, both mass and thickness loss of the pad material were measured following SAE J2986 standards [138]. The standard specifies using a micrometer with a resolution of 0.01 mm, featuring flat surfaces on both sides contacting the brake pad and equipped with a ratchet mechanism, see Figure 3.21a. Measurements were taken at eight positions starting from the outer diameter top leading edge and proceeding clockwise, with position eight at the inner diameter leading edge. Figure 3.21b illustrates these eight measurement positions on the brake pad. Each measurement position should be at approximately dimension ”a” = 5 mm from the edge of the brake pad surface. It should be noted that it was difficult to measure wear on the brake rotor, it was decided that the dimensional wear measurement was excluded.

For gravimetric measurements, a weighing scale with an accuracy of ≤ 0.1 g should be used. The My Weigh Precision Balance, shown in Figure 3.22, has an accuracy of 0.01 g and was employed for the gravimetric measurements of the brake pads.

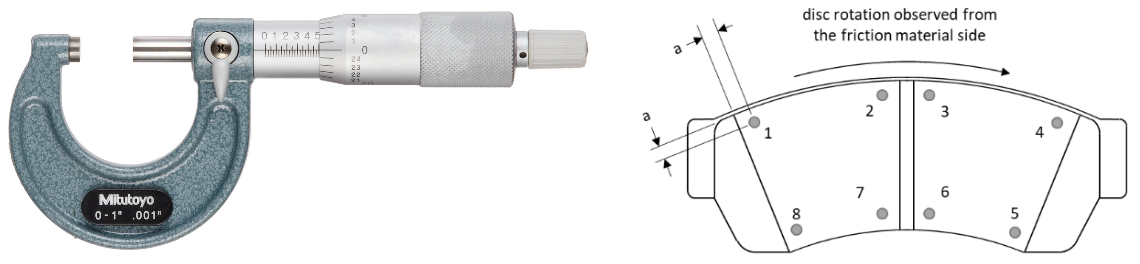

(a) micrometer

(b) Measurement positions for brake pad assemblies [138]

Figure 3.21: Pad wear measurements

Figure 3.22: My Weigh Precision Balance used to weigh brake pad

After the 3 tests at the same brake pressure, post-test analysis of the rotors was conducted. Due to the size and weight constraints of the brake rotor, only a limited number of machines and techniques could be employed. Therefore, Bruker NpFlex (see Figure 3.23) was chosen for 3D surface measurements using white light interferometry (WLI) technology. The Bruker NpFlex is sufficiently flexible to accommodate the size and weight of the brake rotor.

Figure 3.23: Bruker NpFlex

Following the last brake test at low, medium, and high brake line pressures, under both uncorroded and corroded conditions, 3D scans were performed using the Bruker Npflex to monitor and assess wear, pits, crevices, and surface roughness on the brake rotor surface.

In addition to using the NpFlex, we also employed secondary electron microscopy (SEM) and energy dispersive X-ray spectrometry (EDX) techniques. However, due to sample size constraints for both the SEM and EDX, it was necessary to cut the brake rotors and pads. This process was carried out until all testing was complete. The Carl Zeiss EVO MA15 SEM, paired with the AZtecEnergy EDX system, was utilised for both SEM and EDX analyses.

3.9 Summary

This chapter offers a comprehensive overview of the experimental setup used for brake testing, along with the ducting system specifically designed for collecting particle emissions. The particle measurement device, the Dekati ELPI+, is utilised to measure real-time particle mass and number. The section also details the setup and preparation work involved. Additionally, it includes a brief description of the various brake rotor materials and their corresponding friction materials used in the tests.

Due to the limitations of the brake dynamometer, the brake cycle employed was drag braking. The brake testing procedure was based on research conducted by previous students, but it was modified because the high brake pressure previously applied was too demanding and unrealistic for the present tests. For the corrosion portion of the experiment, the equipment and testing procedures were based on the C&W salt spray cabinet and the ASTM B117 standard. A problem arose during calibration tests when the pH of the collected solution dropped significantly. This issue was addressed by increasing the initial pH to counteract the decline.

Both in-test and post-test analyses were conducted on the brake pads and rotors. The in-test measurements included taking images of the surfaces and measuring the wear on the brake rotor and pads after each test. Scanning Electron Microscopy (SEM), Energy Dispersive X-ray Spectroscopy (EDX), and White Light Interferometry (WLI) instruments were all used in the post-test characterisation of the brake rotor surfaces.

Chapter 4

Grey Cast Iron Study

”Man intends one thing, but
The Almighty intends another.”

Khalid ibn al-Walid

4.1 Introduction

This chapter details the performance of the GCI (Grey Cast Iron) brake rotor, which underwent a series of drag brake applications and an aggressive corrosion cycle to assess the impact of corrosion as outlined in Chapter 3. The findings are presented in two sections: pre-corrosion and post-corrosion, followed by a detailed comparison. Key parameters such as the coefficient of friction (CoF), rotor surface temperature, and brake pad wear are examined. Additionally, particle emissions were analysed for both the uncorroded and corroded rotors, with a direct comparison between the two conditions. The chapter also features microscopic images and elemental analyses of the brake rotor before and after corrosion, providing insight into the changing surface conditions. This includes an investigation into the elemental composition of both the rotor and pad surfaces, exploring any potential effects of corrosion on their structure and behaviour.

4.2 Dynamometer test results

4.2.1 Uncorroded rotor

Figure 4.1 displays images of the brake rotor surface following the completion of the three tests at each pressure for the uncorroded rotor. Figure 4.1a shows the new brake rotor, which is covered by a protective coating applied by the manufacturer. This coating, made from a mixture of zinc and aluminium, is designed to protect the rotor from corrosion during storage [133]. Figure 4.1b illustrates that this protective coating was largely removed during the bedding-in process. As shown in Figures 4.1c to 4.1e, the transfer layer on the friction ring of the uncorroded rotor becomes darker and more pronounced with increasing pressures. This development of the tribolayer enhances and stabilises the CoF [74], [139], as demonstrated in Figure 4.3, particularly for the 7.5 and 10 bar tests compared to the 5 bar test.

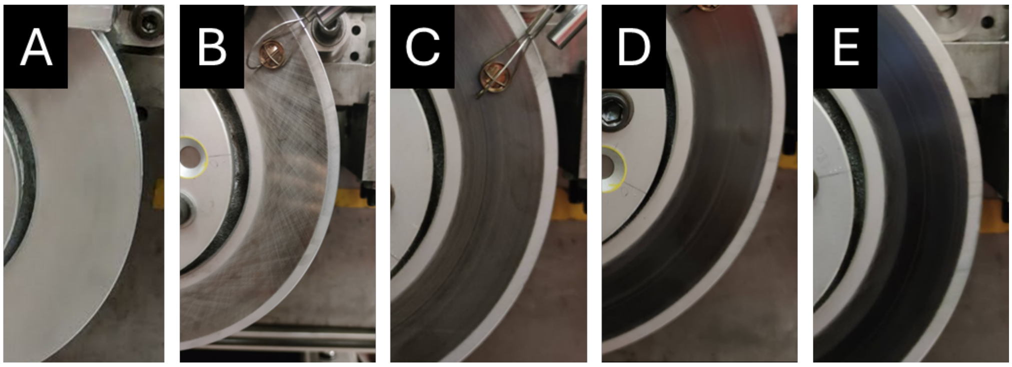

Figure 4.1: Timeline of uncorroded brake rotor: A) New brake rotor, B) After bedding-in, C) After 5 bar, D) After 7.5 bar and E) after 10 bar

Figure 4.2 shows the surface temperature over the duration of the drag brake test, including the pre-conditioning phase, for brake pressures of 5, 7.5, and 10 bar with the rotor in the uncorroded condition. The disc surface temperature was measured using a single K-type rubbing thermocouple, located near the trailing edge of the brake pad, just after the brake calliper. The graph displays all three repeated runs to demonstrate the repeatability of the results under the same conditions.

It can be seen from Figure 4.2 that near steady-state temperatures were achieved for all brake pressures at approximately 2000 seconds after the start of the test. The results also show the expected trend: as brake pressure increases, so does the steady-state disc surface temperature. Specifically, 5 bar produced a steady-state disc temperature of around 200°C, 7.5 bar produced approximately 225°C, and 10 bar resulted in a steady-state temperature near 300°C. Overall, the results indicate good repeatability between runs and clear differentiation between the brake pressures.

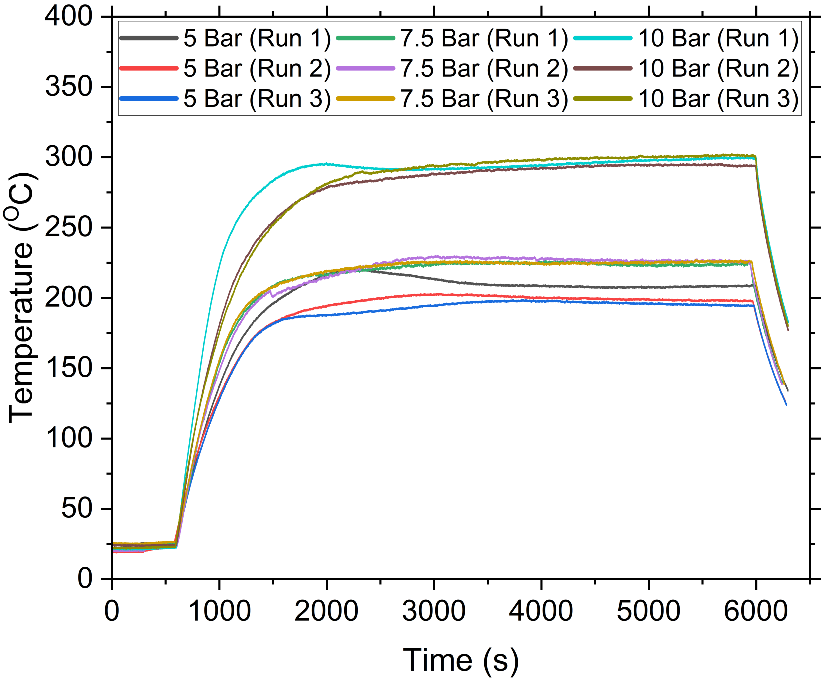

Figure 4.2: Surface temperature vs. Time for 5, 7.5 and 10 bar brake pressure for the uncorroded test

Figure 4.3 presents CoF results at 5, 7.5 and 10 bar in uncorroded conditions. When brake pressure is initially applied, a spike in the coefficient of friction (CoF) is observed across all pressure levels, except for runs 2 and 3 at 10 bar, where a drop occurs instead of an increase. This initial phenomenon lasts for approximately 1500 seconds, after which the CoF stabilises and reaches near steady-state conditions. This initial spike in CoF is likely due to the progressive development of the tribolayer between the brake pads and the disc due to the temperature build-up at the interface [140], [141]. By 2000 seconds, the CoF for all brake pressures and repeat tests stabilises, except for 5 bar run 1, which only achieves near steady-state conditions after 3000 seconds.

As brake pressure is increased, the steady-state CoF decreases, with 5 bar producing the highest CoF and 10 bar the lowest. This reduction in CoF could be due to the brake not yet fully bedded in for the 5 bar tests. As the protective coating can be seen along with the machine marks from the manufacturer, shown in Figure 4.1, which could be an indication of incomplete bedding-in. This produced a higher than expected CoF due to a not fully developed transfer layer.

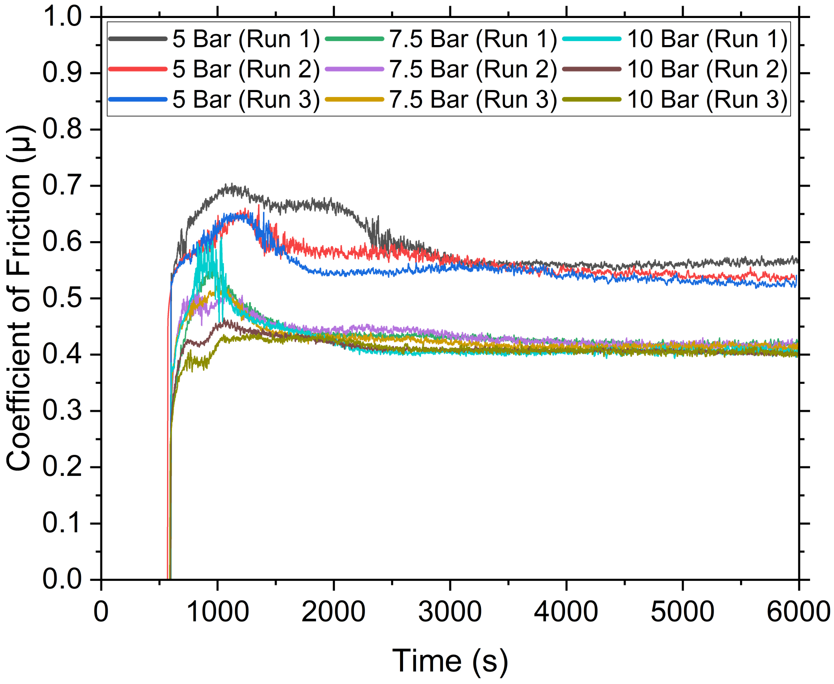

Figure 4.3: CoF vs. Time for 5, 7.5 and 10 bar brake pressure for the uncorroded test

4.2.2 Corroded rotor

Figure 4.4 shows the surface of the corroded brake rotor. Figures 4.4a and 4.4b depict the friction ring and vents of the brake rotor after 96 hours in the salt spray bath. A significant accumulation of corrosion products is evident on the friction ring. Corrosion was also observed inside the vents, despite the protective coating. This could be attributed to differences in thermal expansion between the substrate material and protective coating, which may cause cracks in the coating during brake application [11].

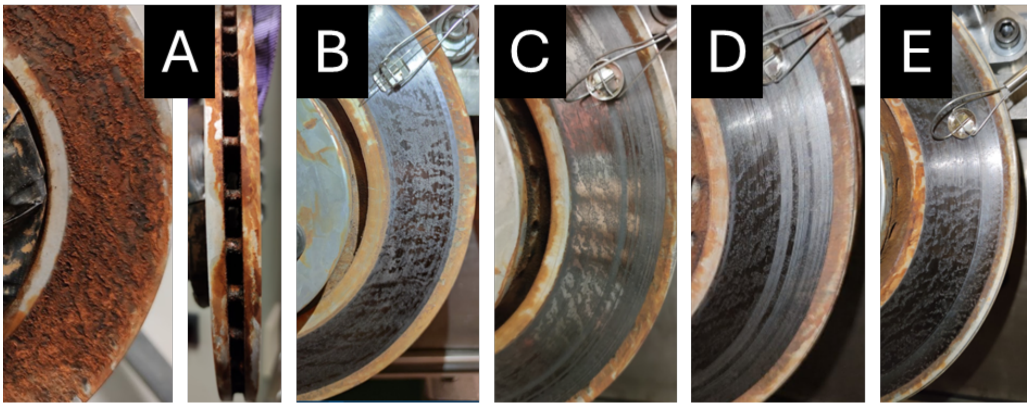

Figure 4.4: Timeline of corroded brake rotor s: A) After 96h in the salt spray brake rotor, C) After bedding-in, D) After 5 bar, E) After 7.5 bar and F) after 10 bar

The results presented in Figures 4.5 and 4.6 show the disc surface temperature and coefficient of friction (CoF) respectively over the duration of the test for each brake pressure, along with the three repeated runs for the GCI disc in the corroded condition.

Figure 4.5 shows that by 2000 seconds into the test, the surface temperature of the corroded rotor for all three brake pressures has stabilised, reaching a near steady-state condition for each test. As before the surface temperature increased proportionally with increasing brake pressure. At 5 bar, the temperature stabilised at around 150°C, at 7.5 bar at around 200°C, and 10 bar, the highest temperature measured was approximately 250°C.

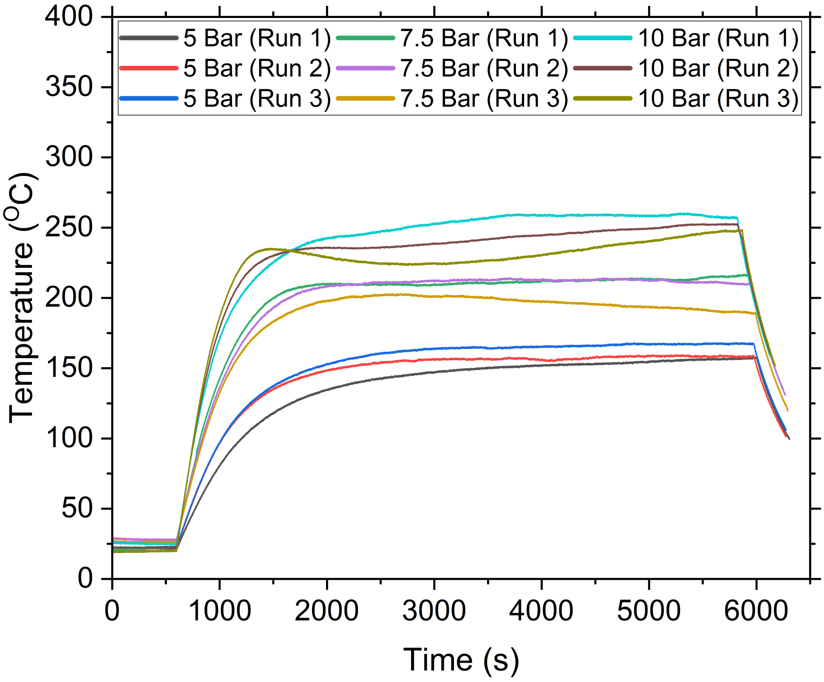

Figure 4.5: Surface temperature vs. Time for 5, 7.5 and 10 bar brake pressure for the corroded test

Figure 4.6 presents the CoF results from the corroded GCI rotor for all test runs at each brake line pressure. The lowest pressure of 5 bar produced the highest CoF, followed by the CoF at 7.5 bar, which closely aligned with the CoF values at the highest pressure of 10 bar. Near steady-state friction conditions were achieved for all brake pressures after 2000 seconds. The measured CoF values for the corroded GCI rotor ranged between 0.3 and 0.45.

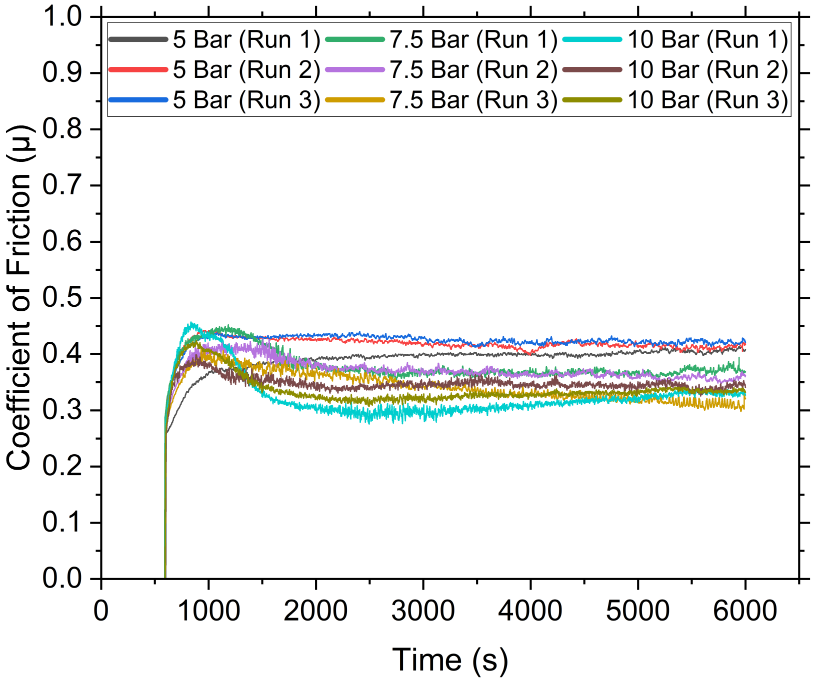

Figure 4.6: CoF vs. Time for 5, 7.5 and 10 bar brake pressure for the corroded test

4.2.3 Comparison

A comparison of the results for the uncorroded and corroded rotor is shown in Figure 4.7 and Figure 4.8 for temperature and CoF, respectively. For clarity, only the final test run results are presented in these graphs

Figure 4.7 illustrates the surface temperature of the uncorroded and corroded GCI brake rotors. The uncorroded rotor displayed a steady-state temperature range between 200°C and just over 300°C, while the corroded rotor exhibited lower steady-state temperatures, ranging between 150°C and 250°C. This may be because the corrosion products remaining on the surface of the corroded rotor produced a greater thermal barrier effect, but also because the CoF (and hence the braking power) was lower than for the uncorroded rotor

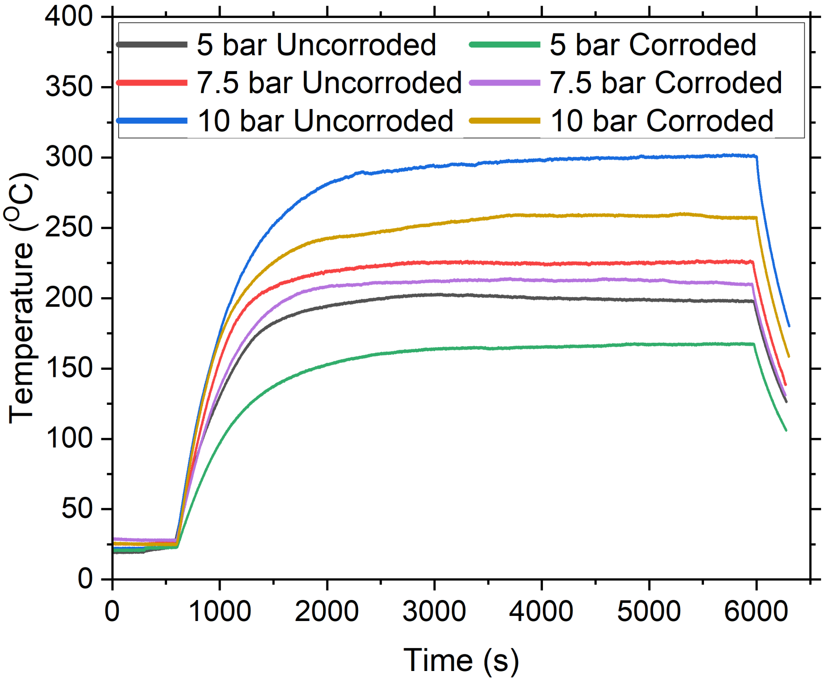

Figure 4.7: Uncorroded and corroded rotor Surface temperature vs. Time at 5, 7.5 and 10 bar brake line pressure

Figure 4.8 compares CoF versus time for both the uncorroded and corroded rotors. It is evident that the corroded rotor did indeed achieve lower steady-state CoF values compared to the uncorroded rotor. Notably, at 5 bar, the corroded rotor exhibited a steady-state CoF of 0.43, whereas the uncorroded rotor produced a steady-state CoF of approximately 0.55. For the 7.5 and 10 bar conditions, similar (although not quite so dramatic) reductions in the steady-state CoF values were seen at pressures of 7.5 and 10 bar.

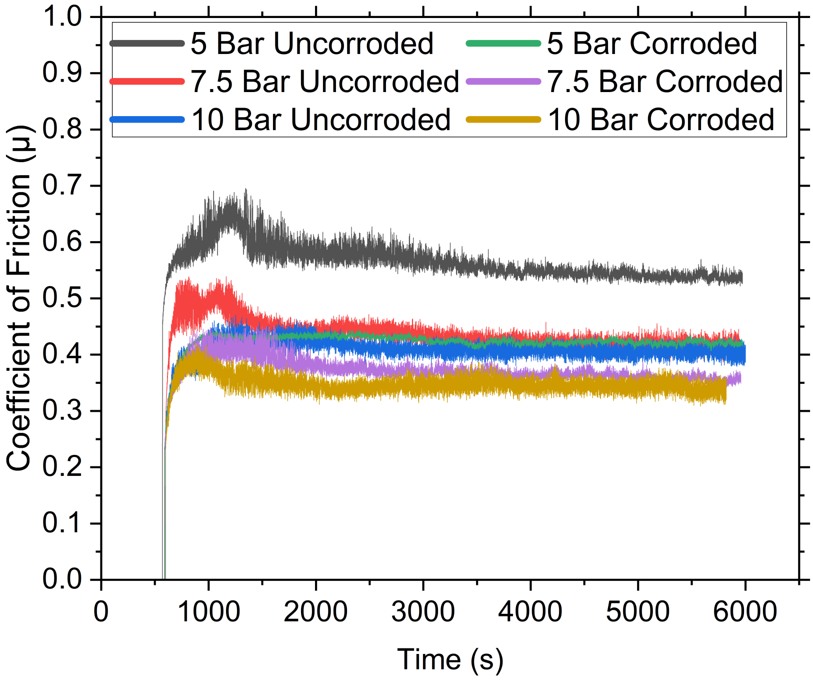

Figure 4.8: Uncorroded and corroded rotor CoF vs. Time at 5, 7.5 and 10 bar brake line pressure

4.3 Particle emission

The particle mass generated from both the uncorroded and corroded rotor tests was measured from the Dekati ELPI+ at each test. For clarity, the brake wear emissions mass presented in Figures 4.9 and 4.10 are categorised into particle size ranges of PM2.5 and PM10, respectively, as these are the two size categories of most concern in the impending Euro 7 legislation.

In the PM2.5 particle size, the uncorroded tests, Figure 4.9 shows that a brake pressure of 5 bar produced the highest PM2.5 particle mass, followed by 7.5 bar, with 10 bar generating the least amount of wear particle mass by a large margin. For the corroded rotor, 5 bar also resulted in the highest PM2.5 particle mass, followed by 10 bar and then 7.5 bar but the differences were smaller.

Regarding the PM10 category, Figure 4.10 shows that 5 bar again produced the highest particle mass in the uncorroded tests, followed by 7.5 bar and then 10 bar, which produced a very small amount. Conversely, 10 bar resulted in the highest PM10 particle mass for the corroded disc, followed by 7.5 bar and 5 bar, which had the lowest PM10 particle mass. It is worth noting that, compared with the uncorroded rotor, the differences in both PM2.5 and PM10 particle mass for the corroded disc across the three brake pressures were relatively minor. In contrast, the particle mass emissions for the uncorroded disc decreased significantly with increasing pressure, despite the fact that the braking power is directly proportional to the applied pressure in these constant rotational speed tests, assuming near constant CoF.

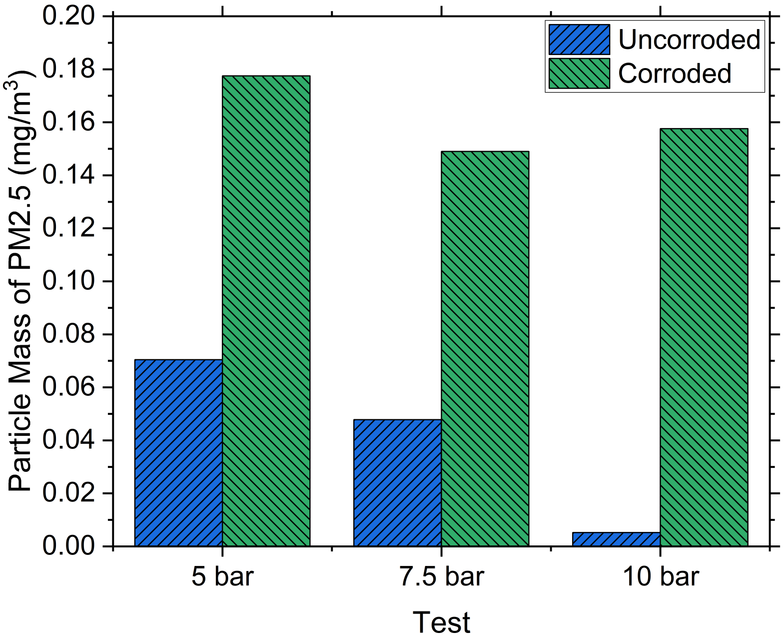

Figure 4.9: PM2.5 particle mass of uncorroded and corroded brake rotor at 5, 7.5 and 10 bar

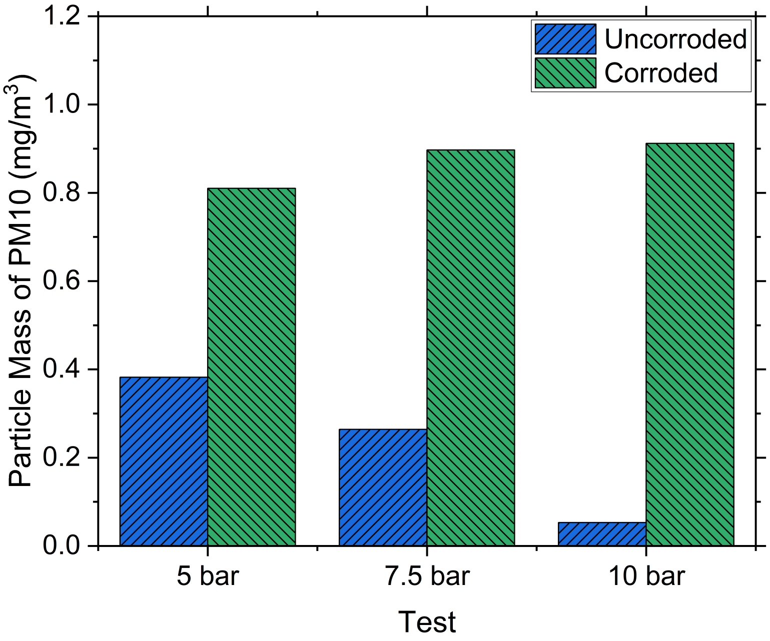

Figure 4.10: PM10 particle mass of uncorroded and corroded brake rotor at 5, 7.5 and 10 bar

4.4 Wear measurements

Figure 4.11 illustrates the average dimensional wear measurements of the brake pads for both the uncorroded and corroded rotor, measured by micrometer at the end of each braking pressure test condition as described in Chapter 3. The error bar represents the upper and lower values.

In the uncorroded tests, it can be seen that 5 bar produced the highest brake pad wear, which correlates with the high CoF observed at this pressure. Conversely, 7.5 bar and 10 bar pressures resulted in lower pad wear, likely due in part to the lower CoF values associated with these higher pressures. The higher pad wear observed at 10 bar compared to 7.5 bar, despite the lower CoF, might be attributed to the higher disc surface temperature measured at 10 bar.

In the corroded rotor condition, 7.5 bar resulted in the highest pad wear, while 10 bar and 5 bar pressures produced slightly lower wear. However, these differences are minimal and likely not statistically significant, unlike the clear distinctions observed in the uncorroded tests. The consistently higher pad wear in the corroded tests may be more influenced by the rough and uneven surface of the corroded rotor apparent in Figure 4.13 rather than variations in CoF and brake temperature.

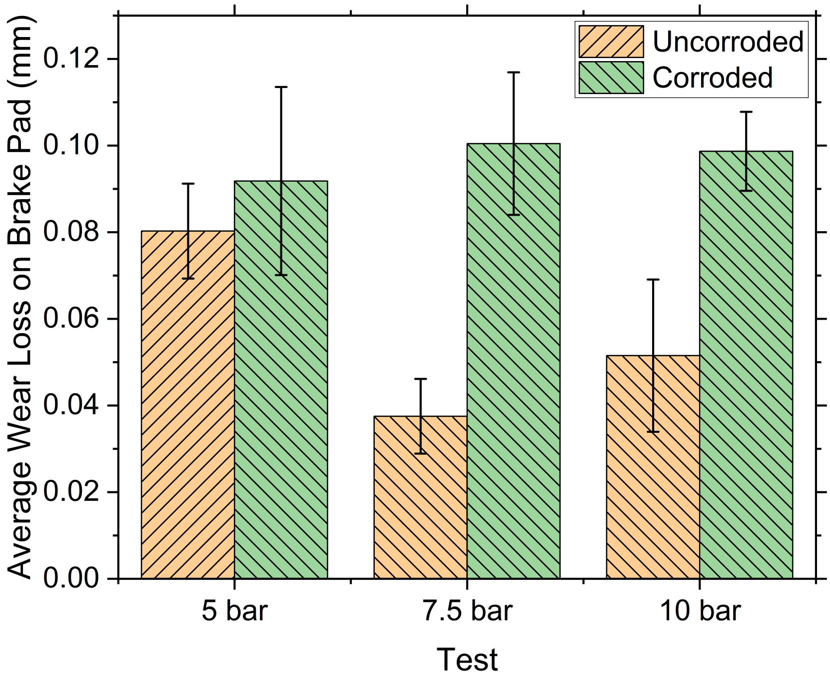

Figure 4.11: Dimensional wear of brake pads at 5, 7.5 and 10 bar brake line pressure for uncorroded and corroded rotor

4.5 Post Test Materials Analysis

4.5.1 White light interferometry

Surface topography images of the uncorroded and corroded brake rotors were captured using vertical-scanning white light interferometry with the Bruker NpFlex, as described fully in Chapter 3. This technique provides non-destructive surface measurements and accommodates the entire rotor without the need for sectioning.

Uncorroded rotor

Figure 4.12 displays the 2D topographic map of the uncorroded GCI brake rotor at the end of the uncorroded brake test procedure. The bottom of the scan image it reveals residual machining marks from the manufacturing process. The surface of the rotor appears relatively flat with high and low spots of ± 2.5 μM, facilitating a large and uniform contact area between the brake pad and the rotor.

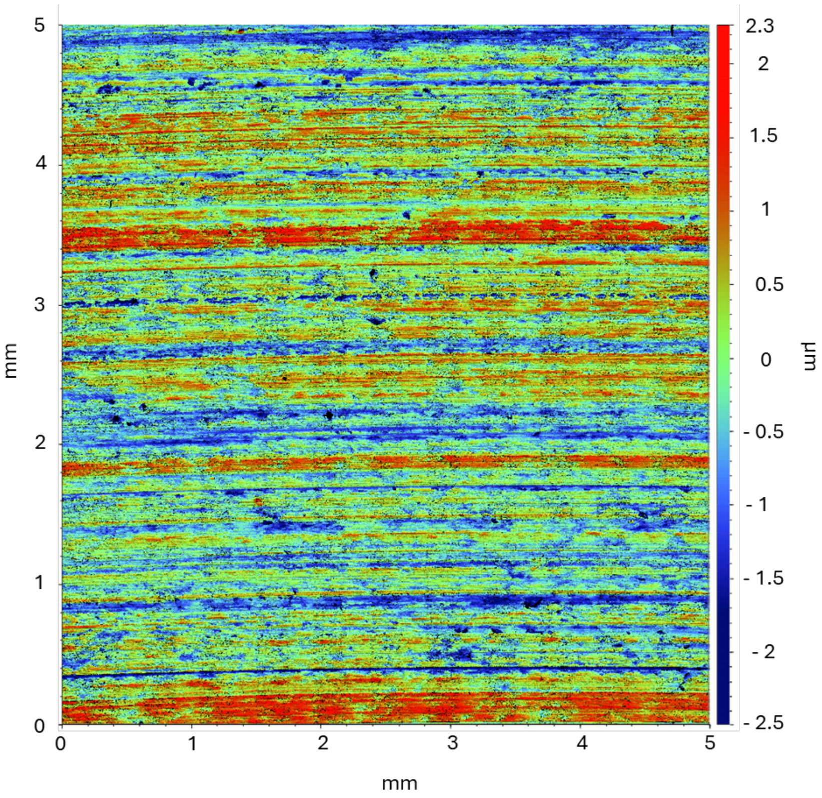

Figure 4.12: Surface topography of uncorroded GCI rotor after the drag brake test procedure

Corroded rotor

The surface topography of the corroded brake rotor was examined after the bedding-in procedure, similar to the uncorroded rotor. Figure 4.13 presents the 2D topographic map of the corroded rotor. The image reveals small cavities and pits on the corroded surface, and the uneven topography suggests a reduced real area of contact with the brake pad. This reduced contact area could explain the lower CoF values observed for the corroded rotor, as shown in Figure 4.8, compared to the uncorroded rotor.

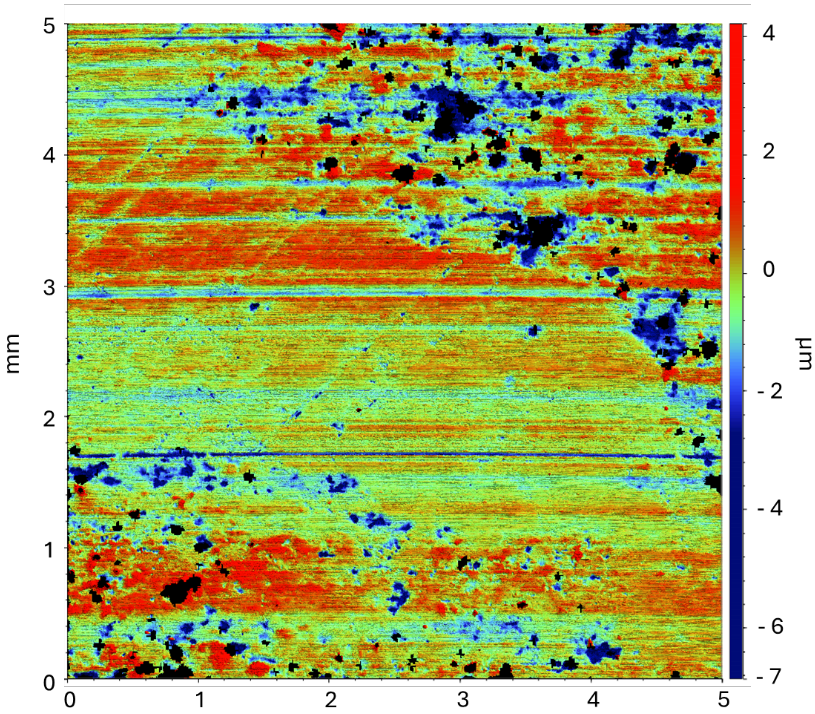

Figure 4.13: Surface topography of corroded GCI rotor after the salt spray treatment and brake bedding-in procedure

4.5.2 Electron microscopy

Uncorroded rotor

The microscope images of the corroded GCI rotor were captured using Scanning Electron Microscopy (SEM) combined with Energy-Dispersive X-ray Spectroscopy (EDX). This microscopy work was conducted at the University of Leeds (UoL) and Keronite Ltd facilities.

The images of the uncorroded rotor were obtained from a trial test sample used to verify that the test procedure met the specified requirements (refer to Chapter 3). The rotor had been subjected to the three brake line pressure tests: 5, 7.5, and 10 bar.

Figure 4.14a presents a cross-sectional image of the tested uncorroded GCI rotor, revealing the graphitic microstructure typical of the GCI material. A closer examination of the contact surface between the pad and the rotor, shown in Figure 4.14b, reveals a deposited tribolayer. This indicates a transfer of material from the brake pad to the rotor surface.

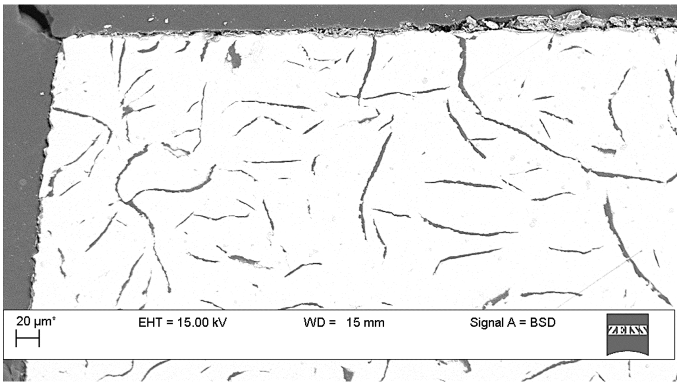

(a) SEM image of bulk material of uncorroded GCI

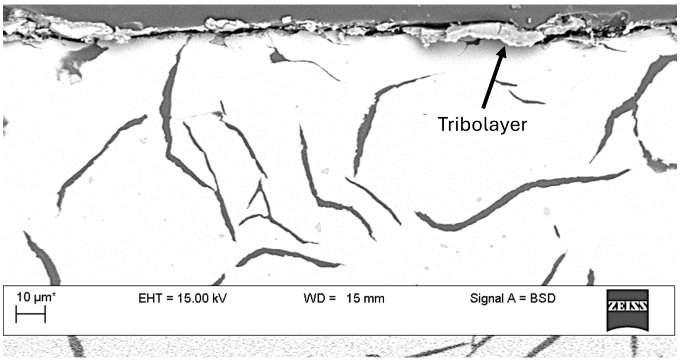

(b) Magnified image of the tribolayer formed on the surface of uncorroded GCI rotor

Figure 4.14: SEM images of uncorroded GCI brake rotor after drag brake testing

Figure 4.15 presents an SEM surface image of the brake pad material tested against the uncorroded rotor. The friction material exhibits scattered flat areas resulting from the pressure and temperature experienced during braking. These flat areas form contact plateaux, which are characterised by both primary and secondary plateaux. The orientation of the wear scars and grooves on these plateaux reveals the sliding direction of the rotor.

Trapped dust is visible around and on some primary plateaux, as highlighted in Figure 4.15. This dust contributes to the formation of secondary plateaux contributing to a tribolayer formed from the worn product [93], [95], [142].

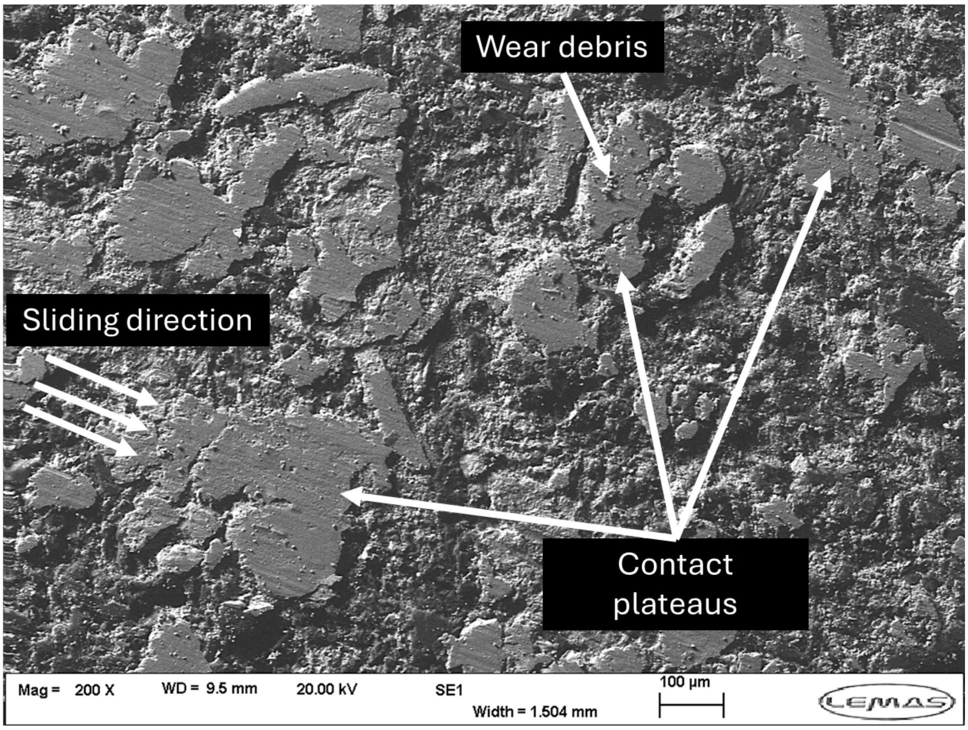

Figure 4.15: Brake pad surface after drag brake testing against uncorroded GCI brake rotor

Figure 4.16 presents an elemental map of the brake pad focusing on the contact plateaux. The map reveals that these plateaux are characterised by high levels of iron and oxygen, indicating that the iron has become oxidised. The detailed elemental analysis, shown in the lower part of the figure, highlights that particular areas, marked by circles, exhibit elevated iron concentrations. These bright areas also show lower levels of oxygen, indicating that the observed material is likely to be an unoxidised iron fibre from the brake pad formulation rather than wear debris.

The large surrounding contact area in the image in Figure 4.16, exhibits higher oxygen content relative to iron, suggesting it represents a secondary contact plateau of oxidised material. The distinction between the primary and secondary contact plateaux provides insight into the rotor's sliding direction. In this image, the rotor slides from left to right over the pad surface, moving in a clockwise direction.

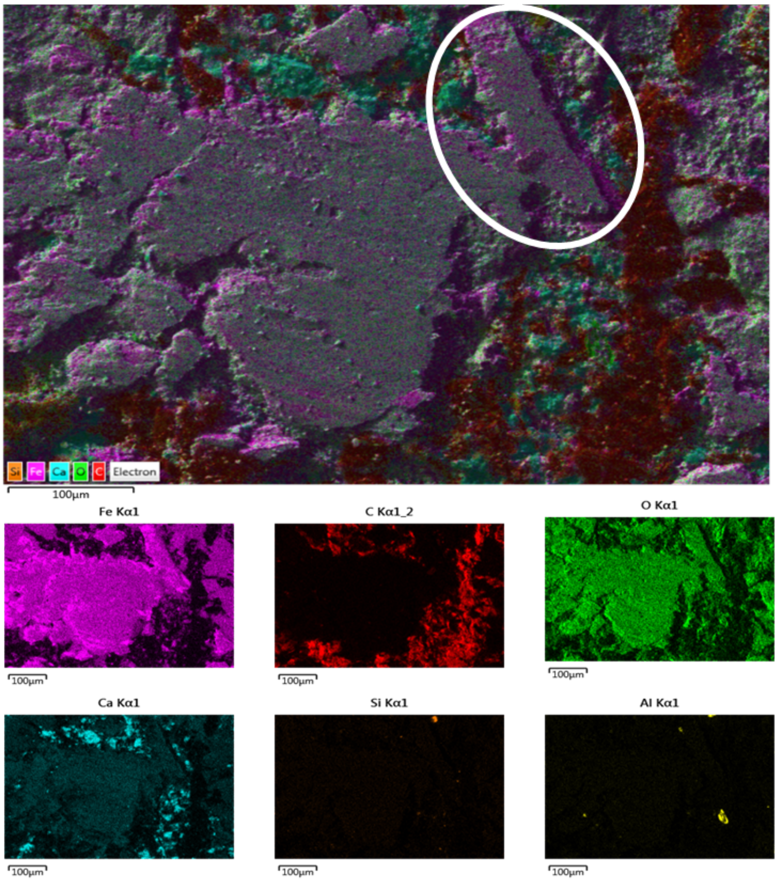

Figure 4.16: Elemental map of brake pad surface after testing against uncorroded GCI rotor

Corroded rotor

Figure 4.17 displays images of the corroded brake rotor following the complete test procedure. The images reveal surface crevices and pits, corroborating the findings from the white light interferometer shown in Figure 4.13. These pits are distributed non-uniformly across various regions of the rotor's surface.

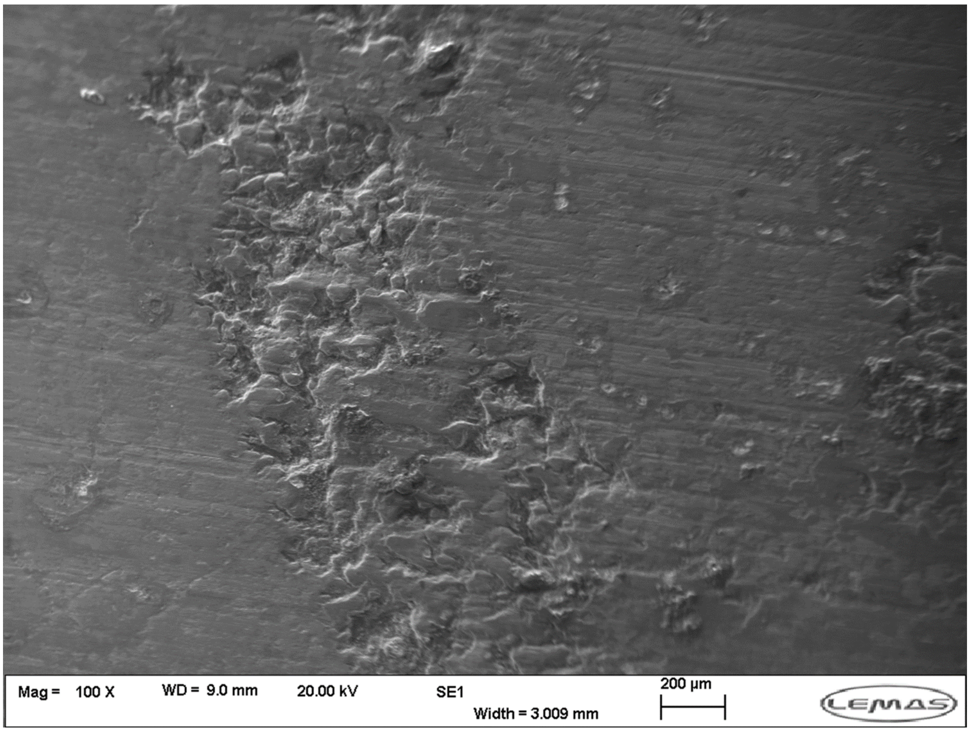

Figure 4.17: SEM image of the damage area on the surface of the GCI brake rotor as a result of corrosion

The elemental map of the corroded brake rotor surface, shown in Figure 4.18, indicates a high content of iron and oxygen, revealing the presence of iron oxide on the rotor's surface. Notably, the crevices on the rotor were found to be carbon-rich. This carbon could either be trapped wear debris from the pad material or exposed graphite flakes from the GCI material.

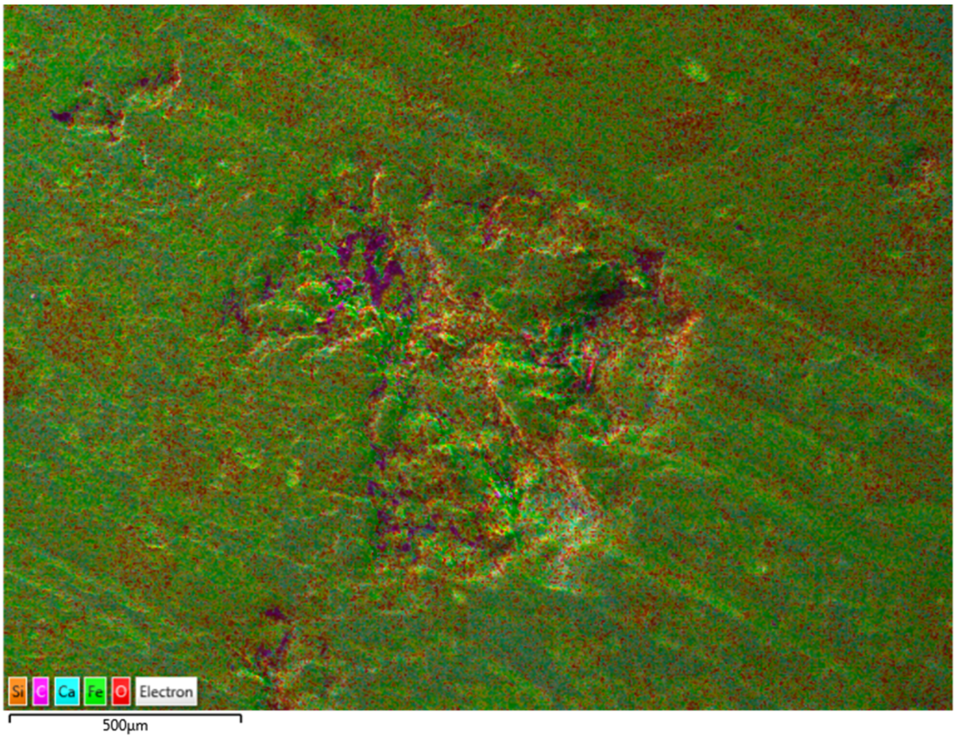

Figure 4.18: Elemental map of the corroded rotor crevices

The cross-sectional image of the corroded brake rotor (Figure 4.19) shows notable differences from the uncorroded rotor (Figure 4.14a). Near the surface, graphite flakes are darker with a grey shadow, whereas deeper in the rotor, the flakes resemble those in the uncorroded rotor, indicating limited corrosion penetration. The image also reveals cracks, delamination, and a potential tribolayer on or near the rubbing surface.

Figure 4.20a highlights the impact of intergranular corrosion on the graphite flakes, leading to material breakdown. Detailed observations (Figure 4.14b) show cracks, delamination, and pits, which expose graphite flakes and explain the high carbon content found in the pits and crevices in the rotor surface.

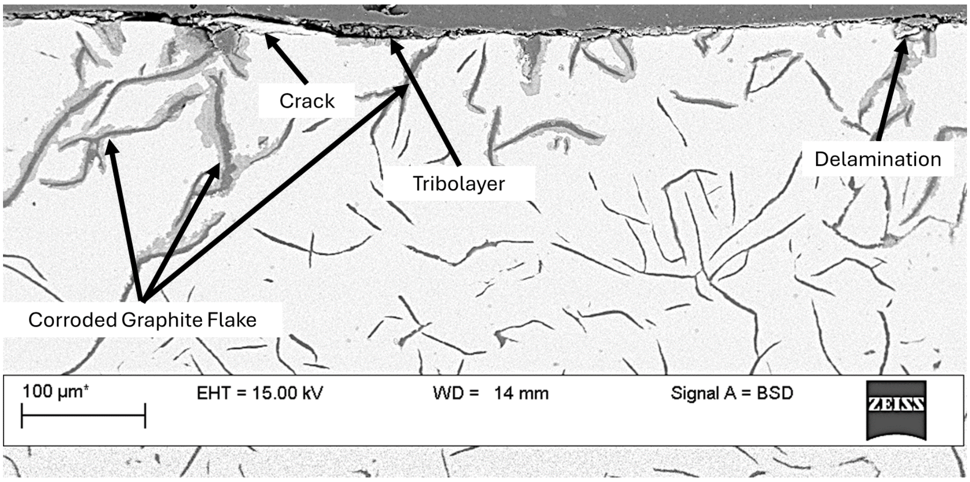

Figure 4.19: Cross section SEM image of corroded GCI brake rotor

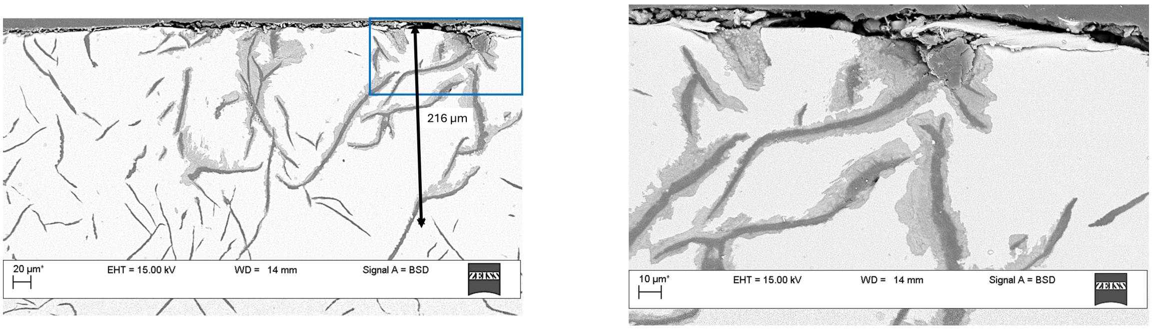

(a) Magnified image cross section SEM image of the corroded GCI

(b) Magnified image of cross section SEM image of crack found on the surface of corroded GCI rotor

Figure 4.20: SEM images of the effect of corrosion on the microstructure of GCI brake rotor

Figure 4.21 shows the surface condition of the brake pad tested against the corroded rotor. The SEM image reveals that the contact plateaux exhibit abrasive wear, resulting in a rougher surface compared to the brake pad tested against the uncorroded rotor (Figure 4.15). This abrasive wear suggests that corrosion pits on the rotor disrupt and degrade the contact plateaux or tribolayer, leading to increased pad wear and particle emissions. Wear debris is also present on the contact plateaux, similar to the uncorroded rotor tests. The wear scars on the plateaux indicate the direction of rotor sliding, which is diagonal as shown in Figure 4.21.

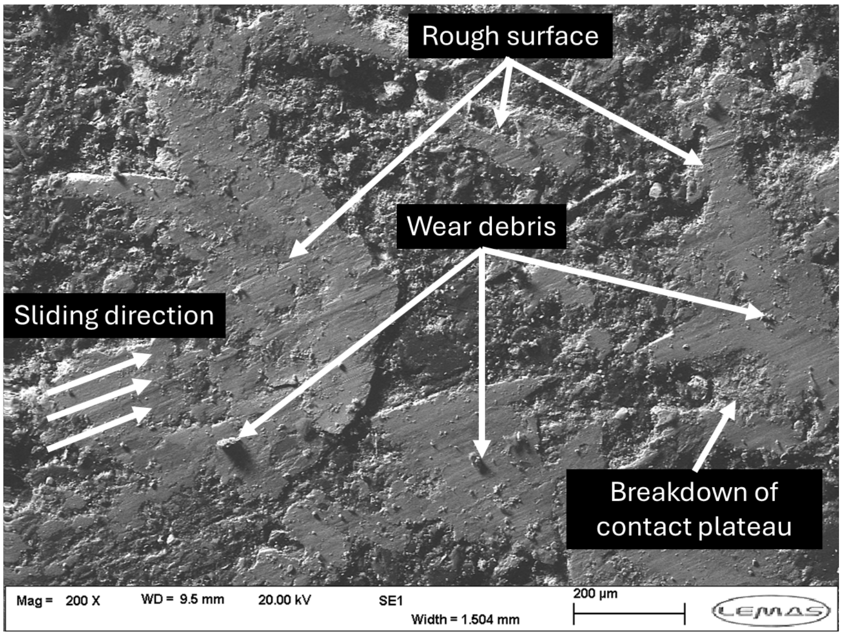

Figure 4.21: SEM image of the surface plateaux and debris found on brake pad tested against corroded GCI

Figure 4.22 displays the brake pad surface after testing against the corroded rotor. The elemental map again highlights that the contact plateaux contain iron oxide. The primary and secondary contact plateaux are distinguished by their iron and oxygen concentrations. The secondary plateaux show higher oxygen levels due to tribological (contact/sliding) stress and elevated temperatures leading to oxidation. In contrast, the primary plateaux exhibit plastic deformation, resulting in a flatter structure [92], [93].

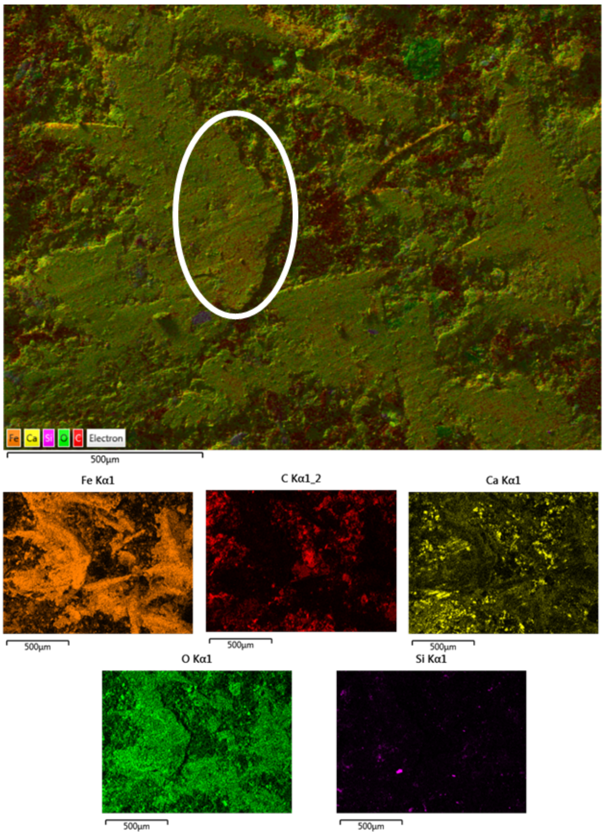

Figure 4.22: Elemental map of contact plateaux on brake pad tested against corroded GCI

4.6 Summary

This chapter examines the effects of corrosion on the performance, wear, and surface structure of a grey cast iron (GCI) brake rotor and a standard low metallic friction material. The adopted test procedures are detailed in Chapter 3. The results indicate that increasing brake pressure leads to higher surface temperatures and generally reduced CoF values. Notably, after a severe corrosion exposure, the GCI rotor exhibited inferior braking performance compared to the uncorroded rotor, with lower CoF values. Despite the lower CoF, pad wear was notably higher against the corroded rotor compared to the same rotor when in the uncorroded condition. Importantly, the corroded rotor emitted at least twice the mass of particles in both the PM2.5 and PM10 categories at the lower brake pressures and almost an order of magnitude more mass at the highest pressure of 10 bar.

Corrosion was found to affect not only the performance and wear emissions but also the surface topography of the brake rotor. The corroded rotor showed surface pits and changes in the GCI microstructure, which may have reduced the true contact area between the pad and the rotor. This may explain the decrease in both CoF and surface temperature in the subsequent drag braking tests as well as the very significant increase in wear emissions. This highlights the susceptibility of cast iron rotors to corrosion effects and explains the drive to either provide a hard and wear-resistant coating to the GCI and/or seek alternative rotor materials.

The following chapter explores the performance of an aluminium metal matrix composite (Al-MMC) brake rotor, which underwent the same testing procedure as the GCI rotor.

Chapter 5

Aluminium Metal Matrix Composite Study

> *"Some are born great, some achieve greatness, and some have greatness thrust upon them"*
>
> *William Shakespeare*

5.1 Introduction

This chapter presents the testing of an aluminium metal matrix composite (Al-MMC) brake rotor. The performance analysis begins with surface temperature and CoF measurements, both before and after the rotor was exposed to a corrosive environment. A discussion of brake pad wear and airborne particle emissions follows this. The chapter also includes a detailed surface analysis, featuring images of the rotor after each testing stage and an examination of its surface topography. Additionally, microscope images and chemical analysis of the brake pad material, both before and after testing, along with post-test analysis of the brake rotor, are provided. A thorough explanation of the findings from the tests and post-test analysis is also included.

5.2 Brake rotor and friction material

The Al-MMC prototype brake rotor consists of a cast aluminium alloy matrix reinforced with 30% SiC particles, shown in Figure 5.1. Choosing the correct friction material to rub against the Al-MMC rotor proved to be a challenge, as Al-MMC rotors have not been used on many road vehicles, especially in the last decade. As the Al-MMC contains hard SiC particles, it was thought desirable to use a friction material specifically developed for hard coatings. Upon testing, this friction material was deemed to be incompatible with the Al-MMC, as it resulted in severe wear on both the rotor and pads. This led to the brake rotor surface needing to be re-machined, as the friction ring had developed deep wear grooves, perhaps due to the hard SiC particles being released due to the abrasive nature of the friction material. Thus, another friction material was used, which was specifically developed for the Lotus Elise S1. It was originally sold with Al-MMC brake rotors. The brake pads were purchased through the Lotus aftermarket store and, therefore, should be compatible with the Al-MMC brake rotor material.

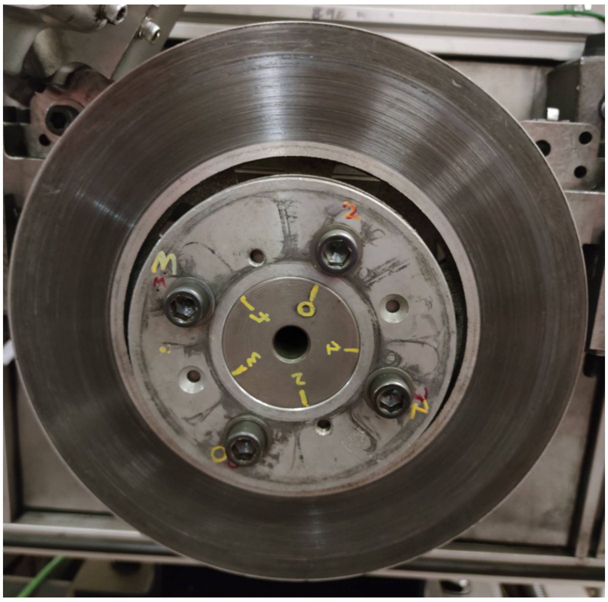

Figure 5.1: Image of aluminium metal matrix composite (Al-MMC) brake rotor

Figure 5.2 below shows the aftermarket Al-MMC brake pads for the Lotus Elise S1. The brake pad selected is for the rear axle calliper of the Elise. This was done so that the brake pad could fit inside the brake calliper on the UoL brake dynamometer. The content of the friction material is outlined later in this Chapter.

Figure 5.2: Image of Lotus Elise S1 MMC rear brake pads

5.3 Dynamometer test results

The brake testing on the Al-MMC rotor followed the methodology described in Chapter 3 and is similar to the testing carried out on the GCI rotor. Three tests were completed for each pressure and generally good consistency between these test results was seen. The exception is the 10 bar test which showed some difference between the three test results.

Included in this section are in-test images of the condition of the brake rotor surface in-between tests of both uncorroded and corroded brake rotor shown in 5.3 and Figure 5.6.

5.3.1 Uncorroded Al-MMC rotor

Figure 5.3 presents surface images of the Al-MMC rotor during the uncorroded tests. Figure 8A shows the virgin surface of the rotor, while Figure 8B highlights the blackened friction surface, indicating the formation of a tribolayer during bedding-in. As shown in Figures 5.3 C, D, and E, the tribolayer continues to develop, becoming darker and more prominent with increasing pressure. By the end of the uncorroded test, the surface of the Al-MMC rotor displays a radial, groove-like pattern around the friction area.

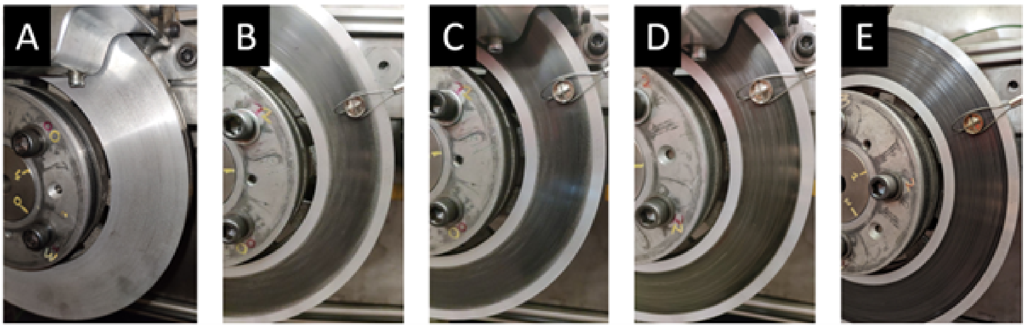

Figure 5.3: Images of uncorroded Al-MMC rotor: A) new brake rotor, B) after bedding-in, C) after 5 bar, D) after 7.5 bar and E) after 10 bar

Figures 5.4, 5.5 display typical surface temperature and CoF time history plots of the uncorroded and corroded rotors under 5, 7.5 and 10 bar of hydraulic pressure. Figure 5.4 illustrates that as the brake line pressure increases, the surface temperature of the brake rotor also increases. The temperature reaches over 300°C at 10 bar, around 200°C at 7.5 bar, and approximately 150°C at 5 bar. Near steady-state conditions were achieved more quickly at 5 and 7.5 bar pressure. At 10 bar run 1 and run 3 achieved a near steady-state after around 4000 s test duration. But for run 2, steady-state conditions were never quite achieved.

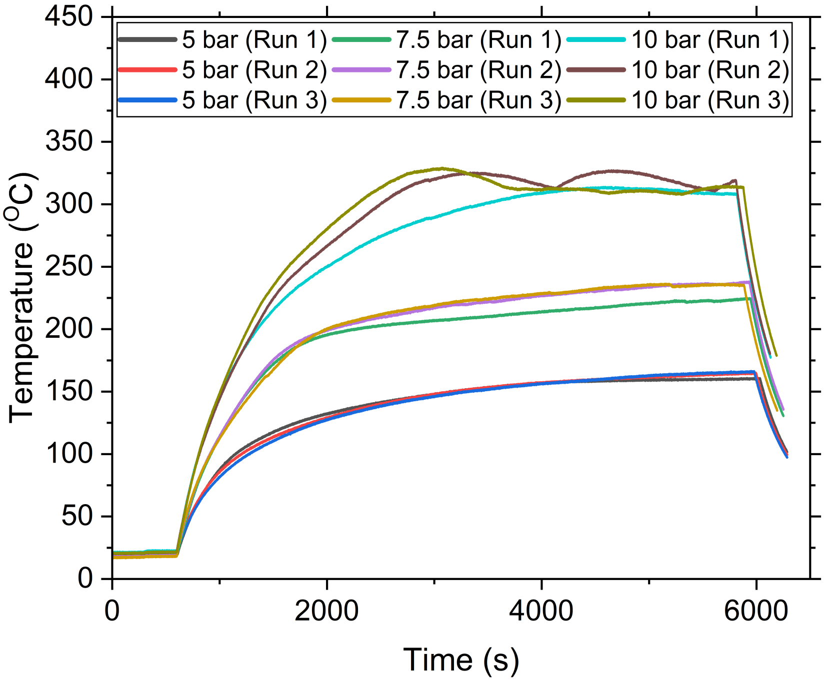

Figure 5.4: Surface temperature vs. Time for 5, 7.5 and 10 bar brake pressure for the uncorroded test

The uncorroded Al-MMC rotor coefficient of friction (CoF), as shown in Figure 5.5, reached near steady-state conditions after 2000s. It was observed that the CoF stabilised more quickly at 5 bar compared to the two higher pressures. At 10 bar, run 2 and run 3, both surface temperature and CoF values fluctate. The steady-state CoF value remained consistently between 0.4 and 0.5 across the different brake pressures, which is considered an acceptable range for this type of brake.

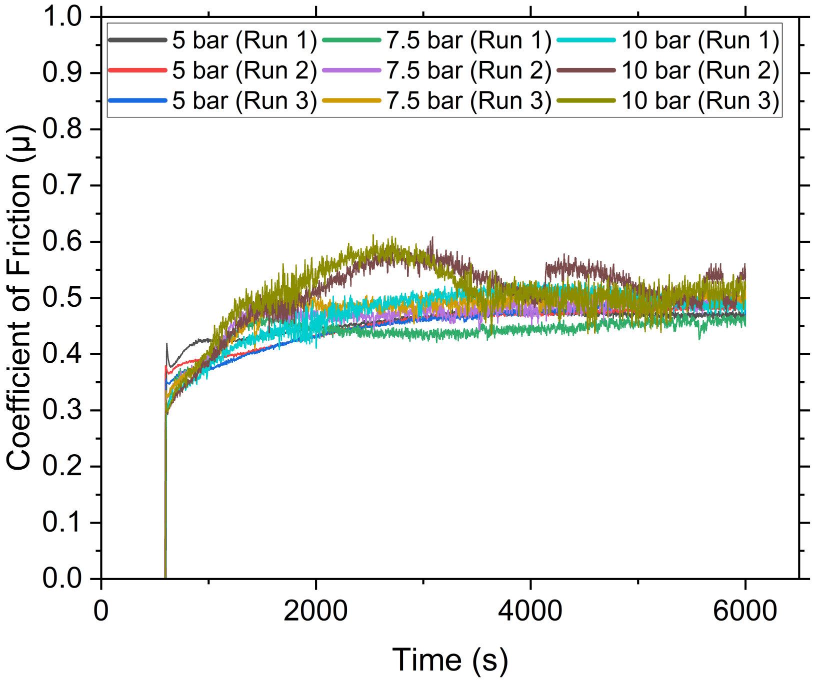

Figure 5.5: CoF vs. Time for 5, 7.5 and 10 bar brake pressure for the uncorroded test

5.3.2 Corroded rotor

Figure 5.6 illustrates the condition of the Al-MMC rotor's friction ring after 96 hours in a salt spray chamber and after different stages of drag brake testing. In Figure 5.6A, the corroded rotor shows dried salt crystals on its surface, which are quickly removed during the subsequent bedding-in process, as shown in Figure 5.6B. Throughout the drag brake test cycles, the rotor surface appears to become smoother and more uniform, as depicted in Figures 5.6C and D. However, underlying pits, caused by corrosion, remain visible after the 10-bar tests, as seen in Figure 5.6E. A groove-like pattern, similar to that observed during the uncorroded 10-bar test, is also present on the friction surface at the end of testing.

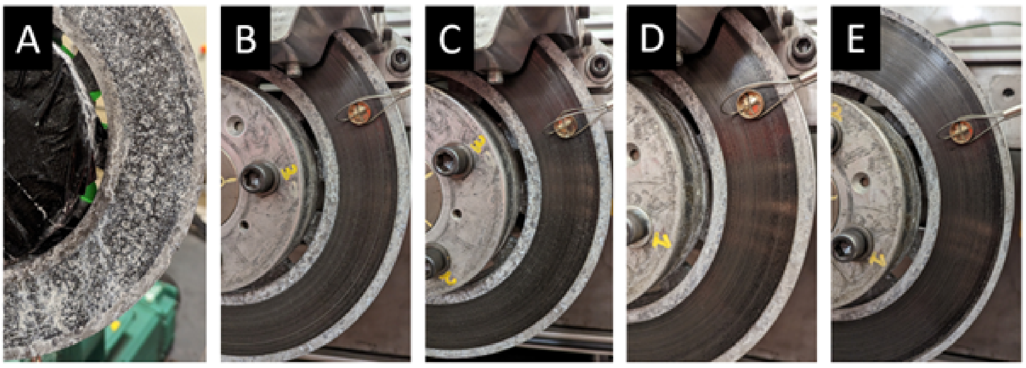

Figure 5.6: Images of corroded Al-MMC rotor: A) after 96h in the salt spray brake rotor, B) after bedding-in, C) after 5 bar, D) after 7.5 bar and E) after 10 bar

Figure 5.7 presents a microscope image of a tested Al-MMC brake pad, captured after the completion of testing. The image reveals the presence of glass fibres on the surface of the brake pad, surrounded by wear dust. This indicates that the glass fibres function as primary plateaus, while the surrounding dust represents the secondary plateaus. Additionally, several wear scars are observable in the radial direction. Overall, the surface structure of the brake pad appears to exhibit no visible damage.

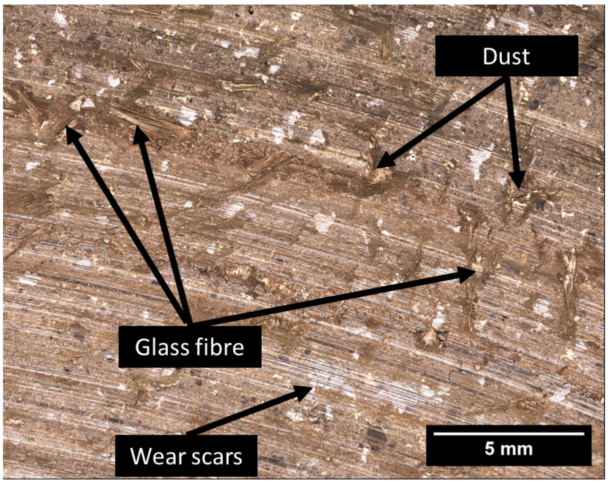

Figure 5.7: Microscope image of Al-MMC brake pad at end of testing

The surface temperature of the corroded Al-MMC rotor, as shown in Figure 5.8, indicates that near steady-state conditions were achieved after about 2000s under all brake pressures. At 5 bar, the steady-state temperature was around 125°C, at 7.5 bar it was around 240°C, and at 10 bar was 275°C. It is evident from Figure 5.8 that at 10 bar, the surface temperature fluctuates and becomes more stable towards the end of the braking application. The results were generally consistent between the 3 tests conducted at 5 bar and 7.5 bar pressure conditions. Whereas, at 10 bar, Figure 5.8 shows that it fluctuated more.

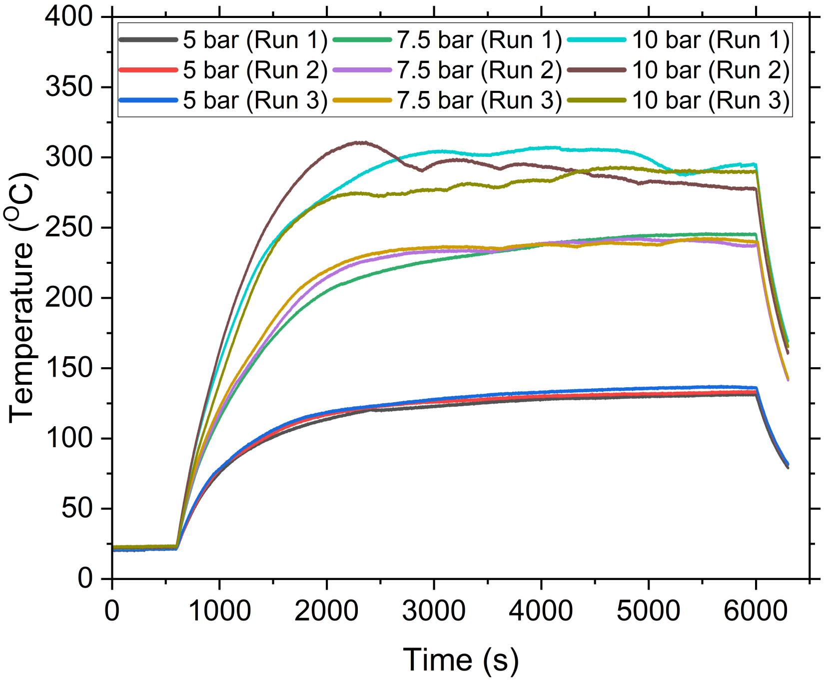

Figure 5.8: Surface temperature vs. time at 5, 7.5 and 10 bar brake pressure for the corroded rotor

The CoF of the corroded Al-MMC, as depicted in Figure 5.9, indicates that near steady-state conditions were achieved at 5 bar much earlier compared to the two higher brake pressures of 7.5 and 10 bar. At 7.5 bar brake pressure, stabilisation occurred after about 3000s with minimal fluctuation in value. However, at 10 bar brake pressure, fluctuations in CoF persisted, eventually stabilising towards the end of the test.

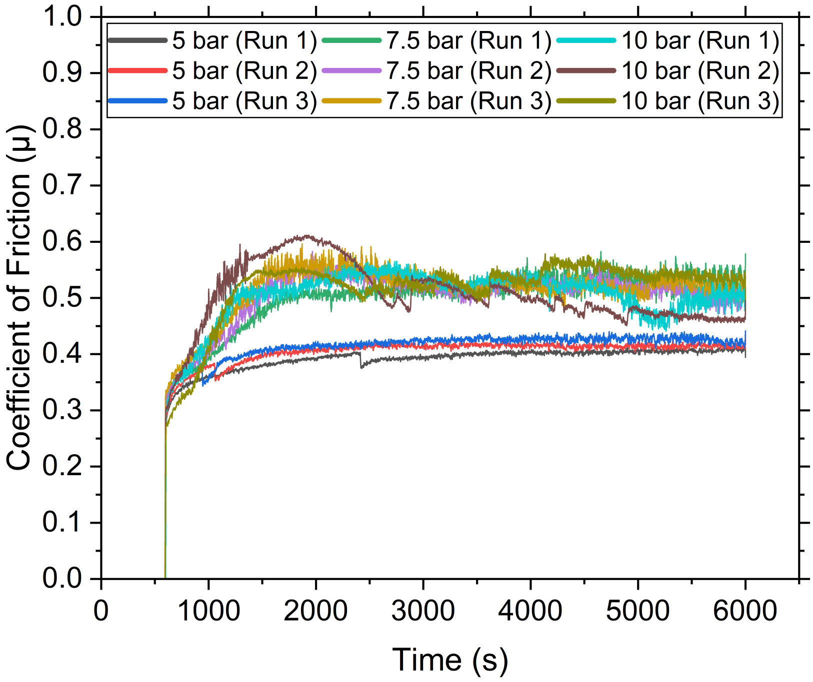

Figure 5.9: CoF vs. Time for 5, 7.5 and 10 bar brake pressure for the corroded rotor

5.3.3 Comparison between uncorroded and corroded rotor test

The typical temperature results shown in Figure 5.10 illustrate that, as brake line pressures increased, the surface temperature increased for both the uncorroded and corroded tests. Generally, the steady-state surface temperature is lower for the corroded rotor in the 5 bar and 10 bar tests. However, at 7.5 bar, the corroded rotor displays a slightly higher surface temperature. Additionally, the corroded rotor exhibits more fluctuations in temperature compared to the uncorroded rotor, particularly in the 7.5 and 10 bar tests.

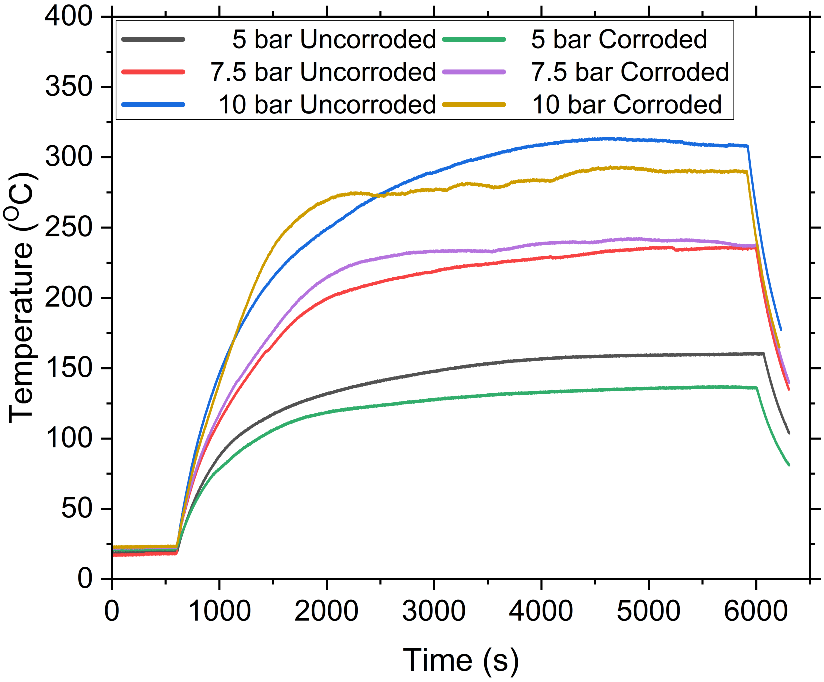

Figure 5.10: Typical rotor surface temperature vs. time for uncorroded and corroded at 5, 7.5 and 10 bar brake pressure

As illustrated in the typical CoF results shown in Figure 5.11, the CoF decreases slightly as brake pressure increased for the uncorroded rotor, likely due to brake fade in the friction material caused by the elevated rotor surface temperature reaching 300°C [143]. In contrast, the corroded rotor exhibited a higher CoF during the 7.5 bar and 10 bar pressure tests. Moreover, the CoF for the corroded rotor fluctuated more throughout the test compared to the uncorroded rotor.

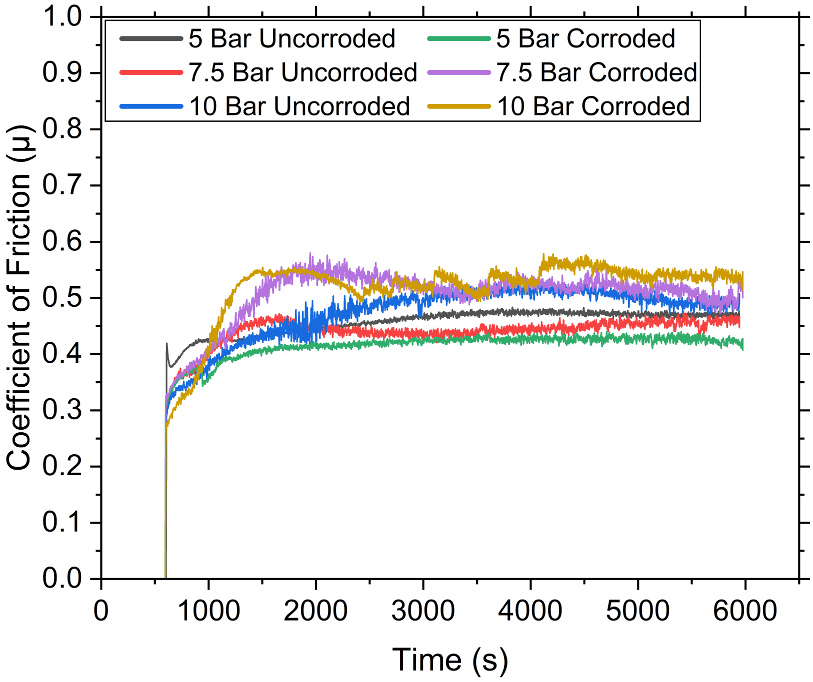

Figure 5.11: Typical coefficient of friction vs. time traces for uncorroded and corroded rotor at 5, 7.5 and 10 bar brake pressure

5.4 Pad wear measurements

The average dimensional and gravimetric wear measurements of the brake pads at each brake pressure for both uncorroded and corroded rotor conditions are shown in Figures 5.12 and 5.13. As expected, both the dimensional wear and pad weight loss increase with rising brake line pressure for both rotor conditions. At 5 bar pressure, the dimensional and gravimetric wear loss for the pad in both uncorroded and corroded conditions was very similar. However, at 7.5 bar the corroded rotor exhibited greater dimensional pad wear and weight loss compared to the uncorroded rotor under the same test conditions. In the high-pressure test of 10 bar the differences between the uncorroded and corroded rotors test results were again small.

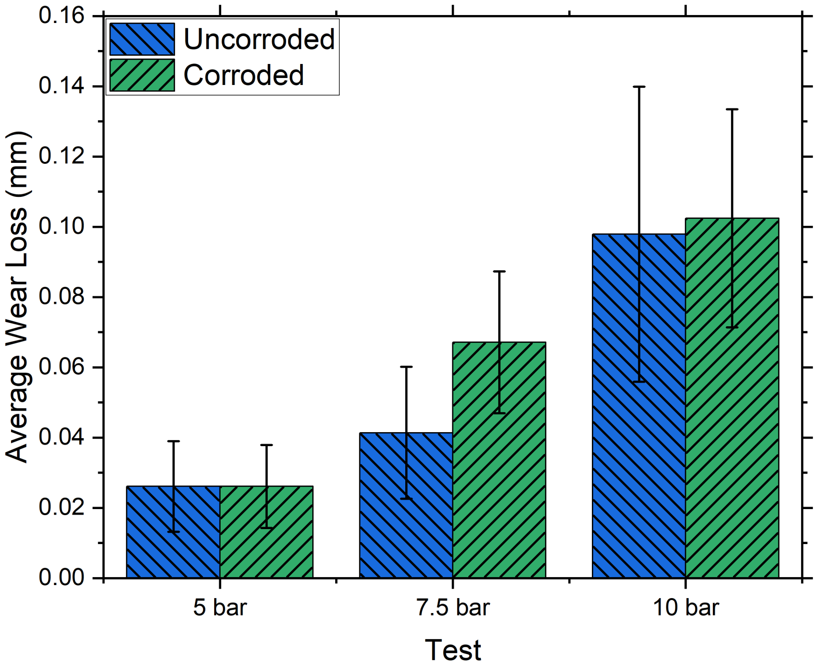

Figure 5.12: Dimensional wear loss of brake pads at 5, 7.5 and 10 bar brake line pressure for uncorroded and corroded rotor

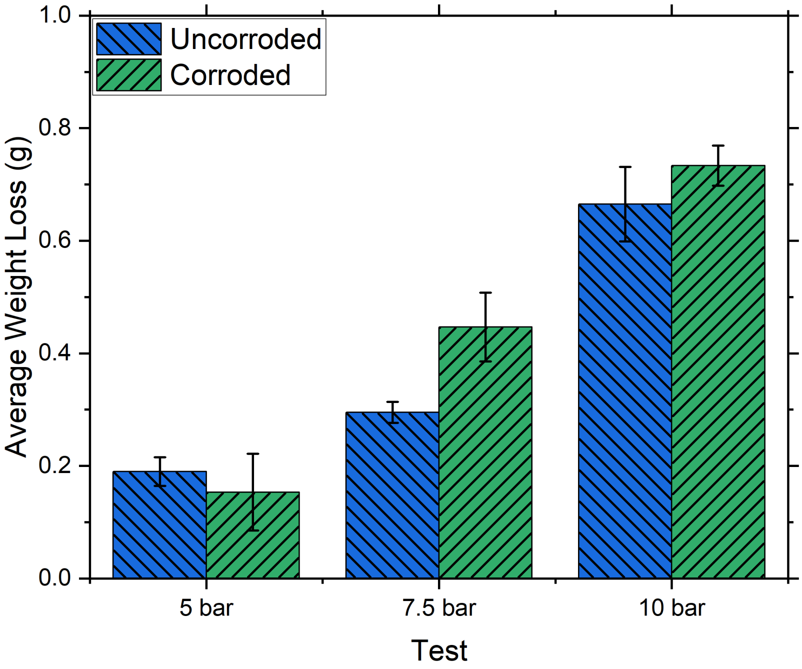

Figure 5.13: Gravimetric wear loss of brake pads at 5, 7.5 and 10 bar brake line pressure for uncorroded and corroded rotor

5.5 Particle emissions

The particle mass emissions from the uncorroded and corroded rotor tests are shown in Figures 5.14 and 5.15, illustrating PM2.5 and PM10 emissions respectively. Figure 5.14 demonstrates that, at 5 bar, the corroded rotor produced approximately 2.5 times higher PM2.5 emissions than the uncorroded rotor. At 7.5 bar, PM2.5 emissions from the corroded rotor were roughly 50% higher, while at 10 bar, the uncorroded rotor emitted slightly more PM2.5 particles compared to the corroded rotor.

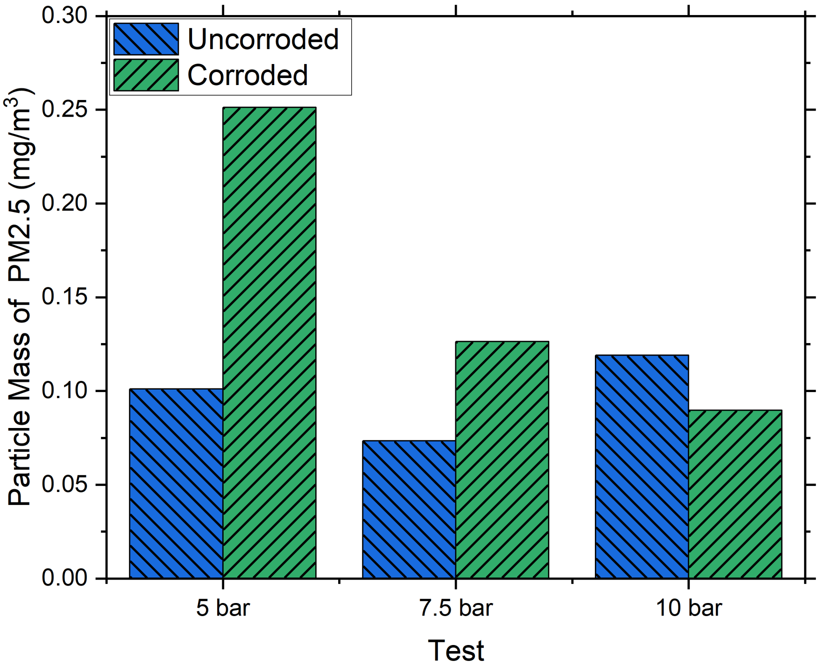

Figure 5.14: Uncorroded and corroded test PM2.5 particle mass at 5, 7.5 and 10 bar brake line pressure

The coarse PM10 particle mass results, shown in Figure 5.15, reveal a similar trend in particle emissions across different brake line pressures for both the uncorroded and corroded rotors. At 5 bar, the corroded rotor generated approximately 3.5 times more PM10 emissions than the uncorroded rotor. At 7.5 bar, the increase was around 60%. However, at 10 bar, the difference in PM10 emissions between the uncorroded and corroded tests was minimal and unlikely to be statistically significant.

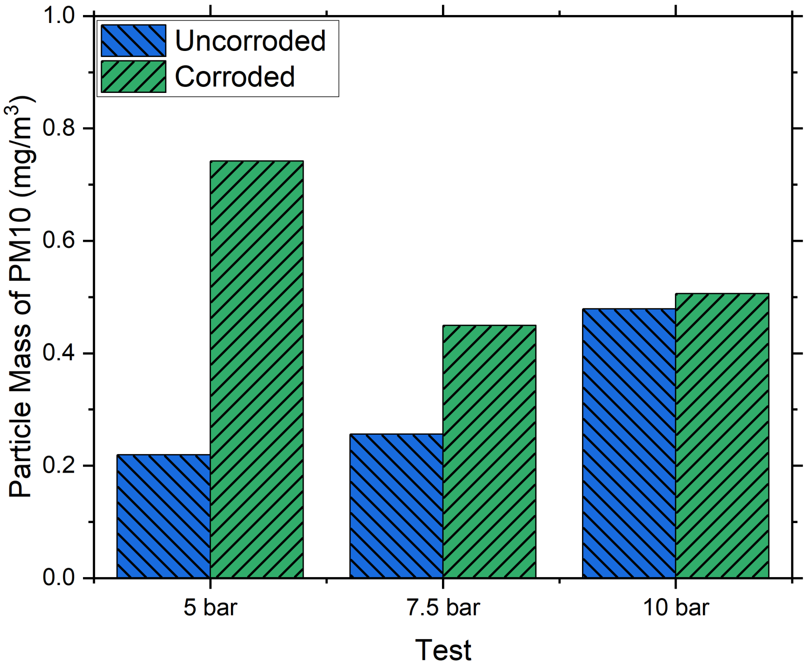

Figure 5.15: Uncorroded and corroded test PM10 particle mass at 5, 7.5 and 10 bar brake line pressure

5.6 Surface analysis

5.6.1 White light interferometer

Figure 5.16 displays the surface topology of the Al-MMC rotor prior to brake testing. Since this rotor had undergone previous testing, the surface had been skimmed by removing any previous transfer layer. The circumferential machining lines, shown in the image, suggest that some silicon carbide (SiC) particles may have been dislodged due to the machining process.

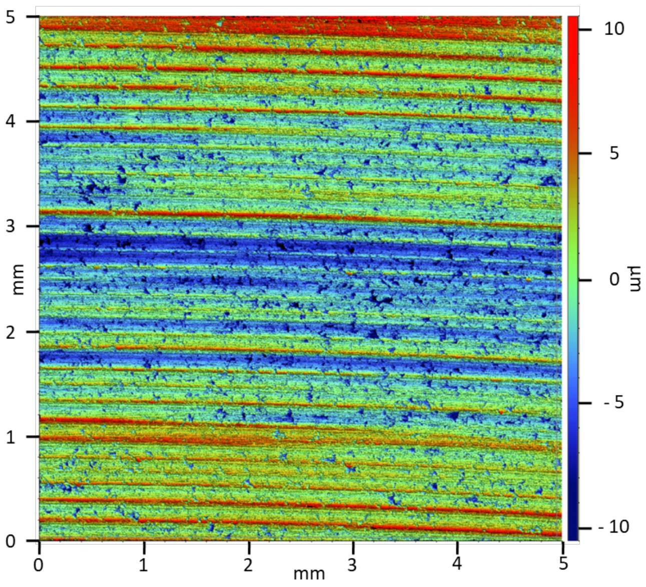

Figure 5.16: Surface topography of Al-MMC rotor after machining

Figure 5.17 shows the images of a section of the friction ring surface of the uncorroded Al-MMC brake rotor after testing at 5, 7.5 and 10 bar. After 5 and 7.5 bar testing, the surface of the rotor was fairly flat in roughness and had few wear scars. However, after 10 bar testing, the rotor's surface shows deeper wear scars than the two lower brake pressures, emphasising the circumferential groove pattern on the rotor surface.

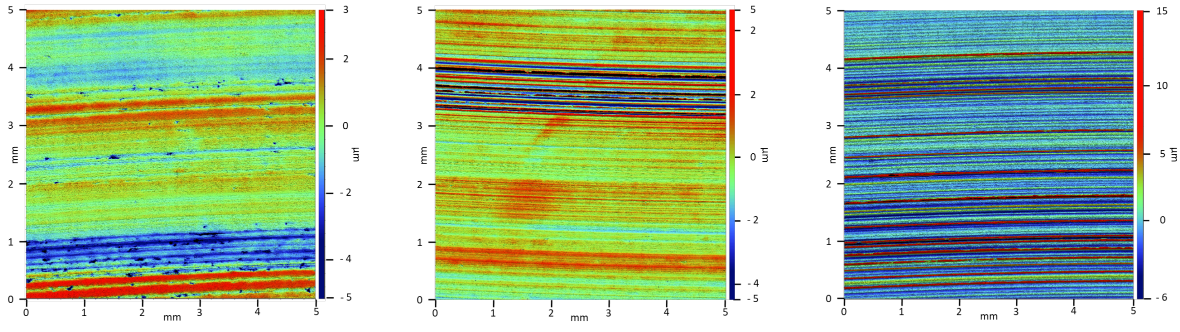

(a) 5 bar

(b) 7.5 bar

(c) 10 bar

Figure 5.17: Surface topography of uncorroded Al-MMC rotor after 5, 7.5 and 10 bar test

Figure 5.18 shows the Al-MMC rotor following 96 hours in the salt spray chamber and the subsequent brake bedding-in procedure. The rotor's surface exhibits deep pits resulting from corrosion. However, the circumferential wear scars on this corroded surface still resemble those observed before corrosion, as depicted in Figure 5.17c.

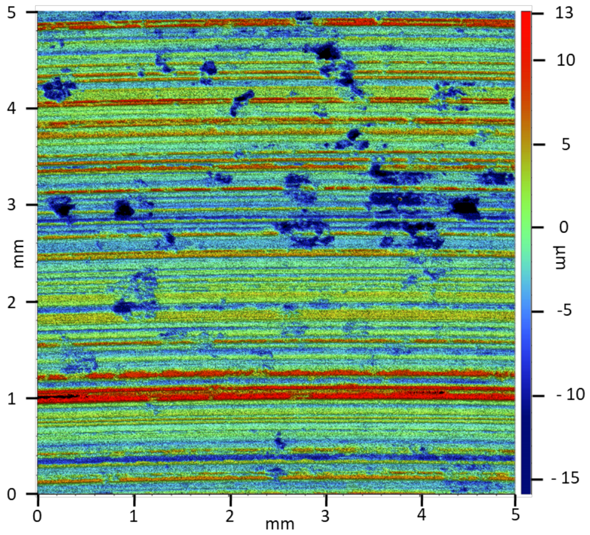

Figure 5.18: Surface topography of corroded Al-MMC rotor after bedding-in procedure

After each brake test, surface topography images were captured of the corroded rotor, similar to those taken during the uncorroded tests, as illustrated in Figure 5.19. The pits present on the rotor surface persisted throughout the corroded rotor tests, as visually indicated in Figure 5.6. After the 10 bar test, the corroded rotor surface exhibited deeper wear scars compared to the lower pressures of 5 and 7.5 bar as for the uncorroded rotor.

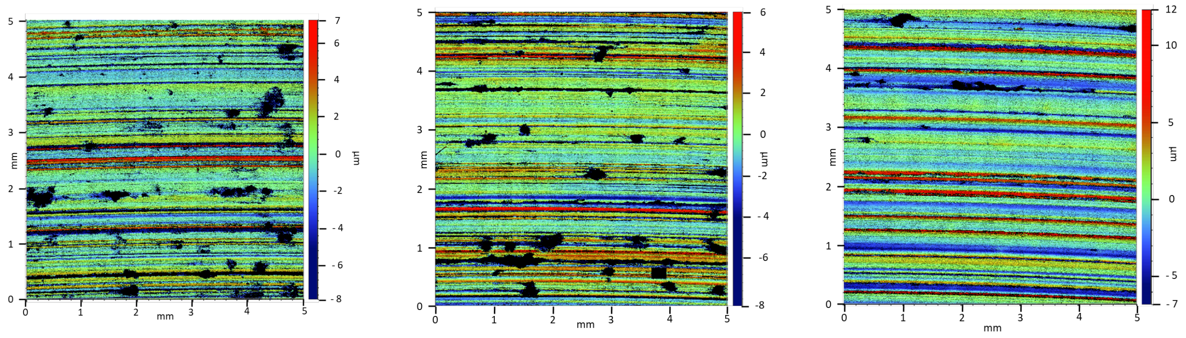

(a) 5 bar

(b) 7.5 bar

(c) 10 bar

Figure 5.19: Surface topography of corroded Al-MMC rotor after 5, 7.5 and 10 bar test

5.7 Post-test analysis

5.7.1 Light microscope

In Figure 5.20, the surface of an Al-MMC rotor is shown at the end of the full test protocol. The image highlights one of the pits observed on the rotor. Surrounding the pit, severe wear marks and damage to the rotor surface are evident. Small silicon carbide (SiC) particles are also visible in the vicinity, indicating that a significant amount of both aluminium alloy and SiC material has been dislodged and removed. The wear scars appear aligned with the sliding direction, which implies that the hard SiC particles may have caused the damage when they were pulled out.

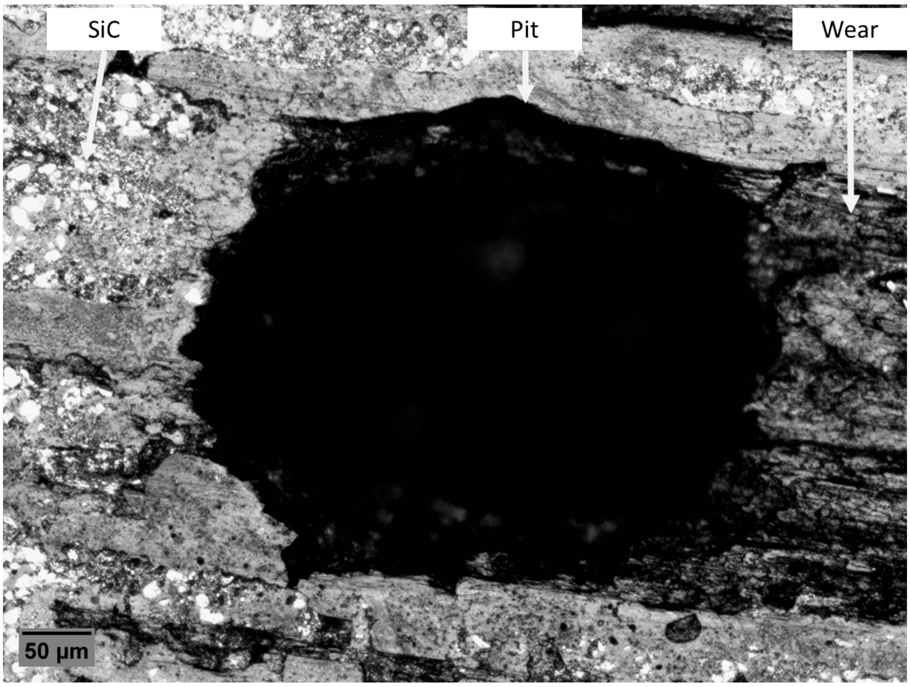

Figure 5.20: Surface image of corroded Al-MMC brake rotor at end of testing

5.7.2 Secondary electron microscope

Figure 5.21 presents cross-sectional images of the Al-MMC brake rotor after the full cycle of brake and corrosion testing. In Figure 5.21a, the cross-sectional SEM image reveals multiple pits at varying depths below the material rubbing surface. A closer examination of these pits, illustrated in Figure 5.21b, shows that significant amounts of SiC particles have been dislodged from the aluminium alloy matrix. The formation of the pits, assumed to be due to the removal of SiC particles exacerbated by the severe corrosion conditions, adversely affects the contact surface, leading to disruptions in the tribological conditions between the brake pad and rotor surfaces.

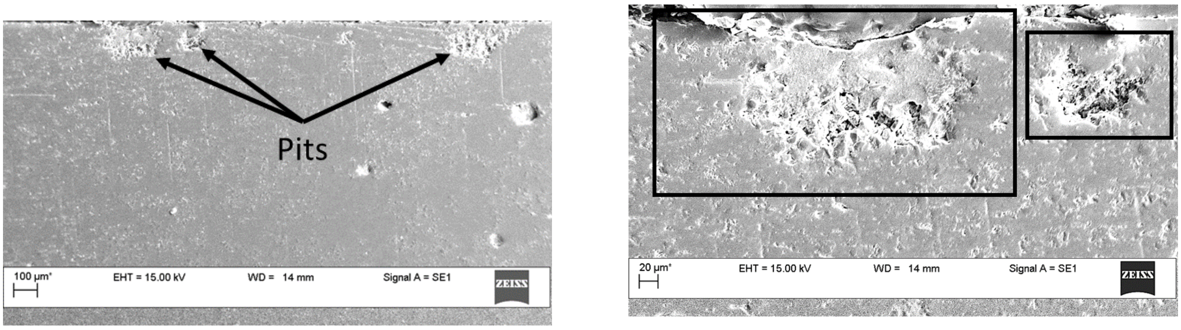

(a) SEM image of tested Al-MMC brake rotor

(b) Close-up SEM image of pits found on Al-MMC brake rotor

Figure 5.21: Cross-sectional SEM images of the Al-MMC brake rotor after testing

5.7.3 Energy dispersive X-Ray

Figure 5.22a presents an EDX map of the brake pad material's surface alongside a SEM micrograph of the pad surface. Table 5.1 details the weight percentages of the key elements identified on the surface. Both carbon (C) and oxygen (O) are likely to be present on the brake pad surface; however, their concentrations are not quantified in Table 5.1 due to their low atomic numbers and the carbon coating applied to the microscopy samples.

Figure 5.22b provides a cross-sectional view of one of the brake pads, highlighting the presence of various elements within a tested pad. Notably, a small tribolayer can be observed near the top of the image.

From the percentage elemental composition shown in Table 5.1, it can be seen that these special aftermarket brake pads are not Cu-free, and the relatively high percentages of barium (Ba) and silicon (Si) indicate the inclusion of abrasive particles and glass fibres, respectively.

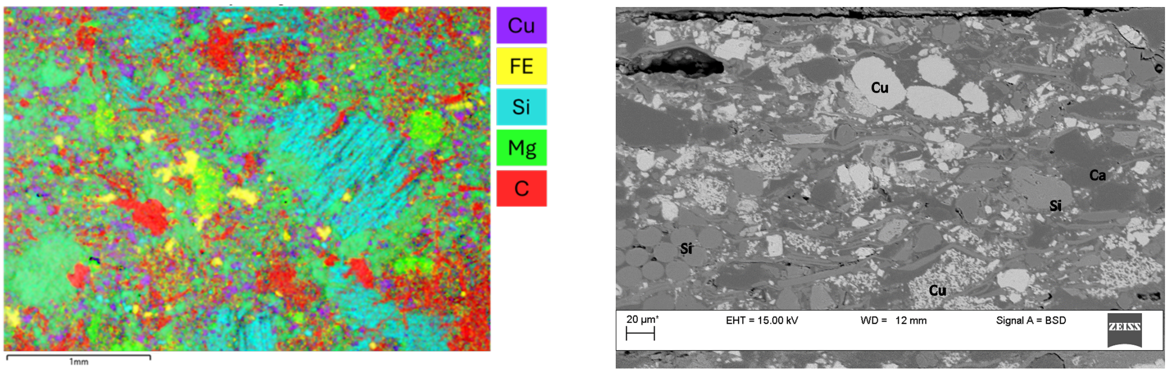

(a) EDX plan view MMC brake pad

(b) Cross section of MMC brake pad

Figure 5.22: Elemental analysis of MMC brake pad

Table 5.1: Elemental composition of the investigated Al-MMC brake pad obtained from EDX

Element	Weight (%)
C	-
O	-
Ba	14.4
Si	12.8
Cu	10
Mg	8.7
Ca	7.4
Al	5.7
Fe	5.3
S	3.8
K	2.1
Zn	0.4

5.8 Summary

The uncorroded Al-MMC rotor successfully withstood high surface temperatures of 300°C during prolonged drag braking conditions, achieving steady-state CoF values ranging from 0.4 to 0.6, despite exhibiting signs of significant surface grooving.

However, after being exposed to 96 hours in a salt spray chamber, the rotor's surface changed, and corrosion pits formed, perhaps due to dislodging of SiC particles as a result of corrosion of the Al matrix. Thus the corroded Al-MMC rotor demonstrated less stable friction, lower surface temperatures, and increased wear loss. Additionally, brake wear emissions in both PM10 and PM2.5 categories rose following the corrosion exposure at both 5 and 7.5 bar pressure. However, at the higher brake pressure of 10 bar, the corroded rotor produced lower PM2.5 emissions and similar emissions in the PM10 category.

Overall the Al-MMC rotor performed quite well and was less affected by the corrosion cycle than the GCI rotor, the results for which are described in Chapter 4.

The following chapter reports the results for the PEO-coated brake rotor under the same test matrix conditions using the same pad material as for the Al-MMC rotor.

Chapter 6

Plasma Electrolytic Oxidation - Aluminium (Al-PEO) Study

"Measure what is measurable, and make measurable what is not so"

Galileo Galilei

6.1 Introduction

This chapter firstly details the plasma electrolytic oxidation (PEO) coating process applied to a unique three-piece rotor design, machined from a wrought billet of Al-6082 alloy. The results of the braking performance and particle wear emissions are presented and evaluated. The impact of subjecting the Al-PEO rotor to 96 hours in a corrosive environment was investigated, focusing on how this exposure influenced braking performance, wear and coating durability. Surface analysis techniques, including light microscopy, secondary electron microscopy, and white light interferometry, were employed to comprehensively assess changes to the surface during the testing proposal.

6.2 Plasma electrolytic oxidation (PEO) coating process

The prototype Al-PEO rotor used in this study was machined from a wrought AA6082 billet and assembled as a three-piece unit comprising two rubbing surface cheeks (one integrated with the bell) bolted together with a separate ventilation ring, as shown in Figure 6.1. This innovative three-piece design was developed to enable straightforward modifications to the vent configuration by replacing or machining a new ventilation ring.

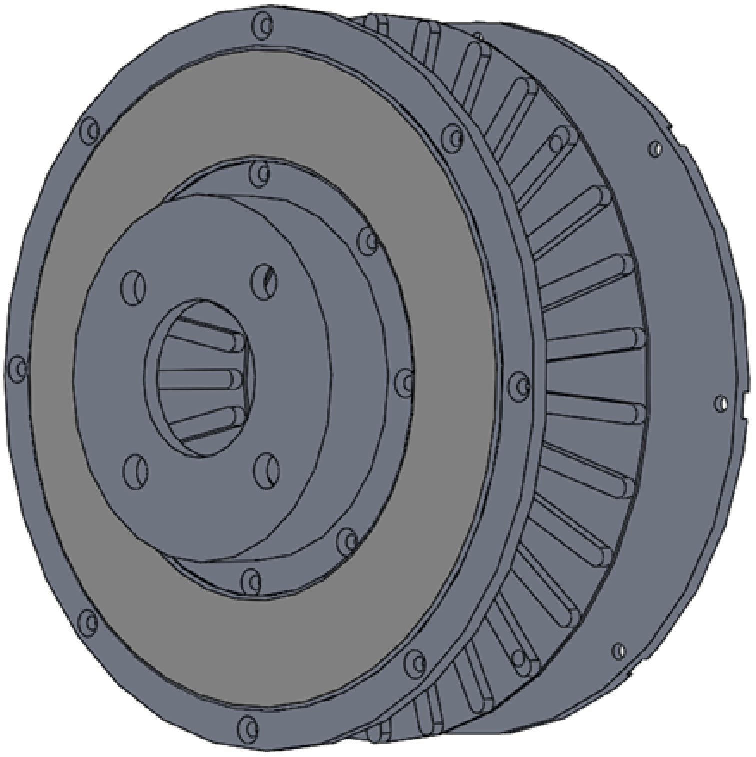

Figure 6.1: 3D model of Al-PEO brake rotor in exploded view

The two rubbing surface cheeks of the uncoated Al-PEO rotor are shown in Figure 6.2. These components represent the sections of the Al-PEO brake rotor that underwent PEO treatment. Specifically, the raised area, elevated by 2 mm, corresponds to the brake pad contact region on the rotor. Isolating and PEO treating only the rubbing surfaces is a more efficient approach than coating the whole rotor. This study focused on investigating the tribological properties, braking performance, and the effects of corrosion on the PEO coating.

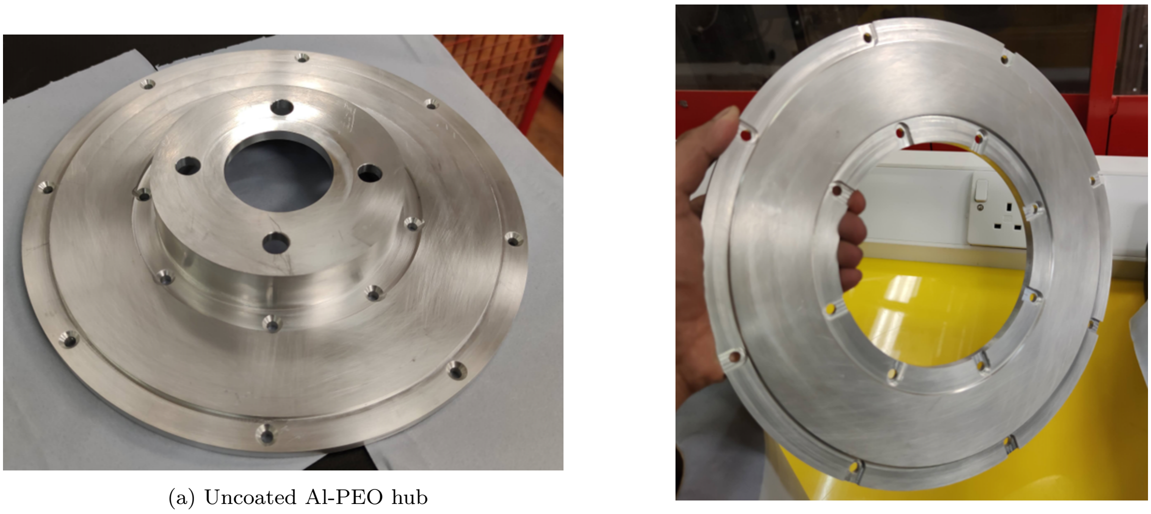
(a) Uncoated Al-PEO hub

(b) Uncoated Al-PEO back-plate

Figure 6.2: Uncoated Al-PEO rotor hub and backplate

To isolate and coat only the friction ring a specified wax, Suprawax 114, was applied to mask areas that were not intended to be PEO coated. The raised friction ring facilitated the precise application of the wax, keeping it away from the desired coating area. Figure 6.3 shows a masked, uncoated Al-PEO rotor. The wax application was performed using a paintbrush inside a fume cabinet while wearing gloves. Once one side of the rotor was coated with Suprawax 114 and had dried, the other side was similarly coated. Multiple layers of Suprawax 114 were applied to ensure a thick and uniform mask, preventing unwanted exposure to the PEO treatment. It is worth noting that one screw hole on each piece was intentionally left unmasked to allow for an electrical connection during the PEO process.

The masked halves of the Al-PEO rotor were sent to Curtiss Wright-Keronite Ltd for the plasma electrolytic oxidation (PEO) surface treatment. The process involved submerging the components into a 1000-litre bath containing a low-concentration alkaline electrolyte solution. During the process, the Al-PEO rotor acted as the anode, while the stainless steel bath served as the cathode. The parameters for the treatment were controlled by Keronite and remain proprietary.

An electrical connection to the Al-PEO rotor was established through a jig connector via the unmasked screw hole. A high voltage was applied to the rotor, generating an intense plasma discharge on the unmasked surface area. This plasma discharge created a durable oxide layer on the surface, composed primarily of crystalline alumina (Al_2O_3) [131].

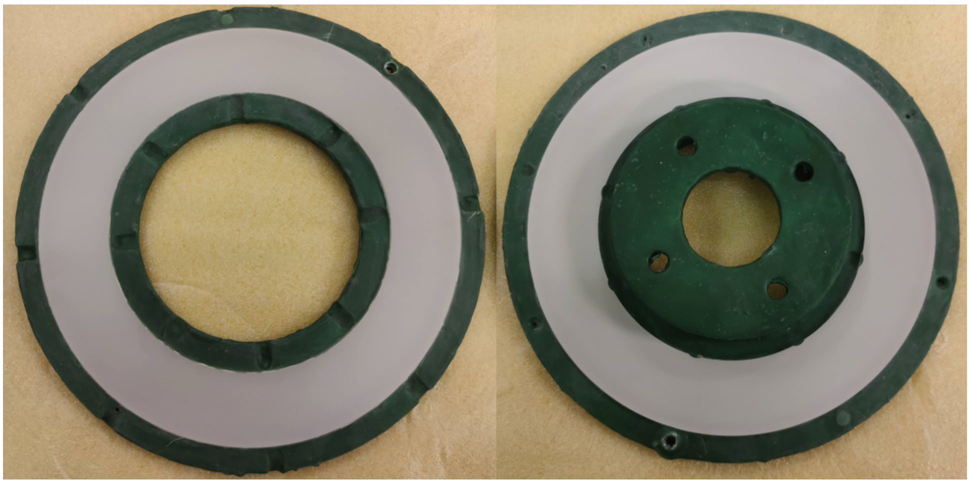

Figure 6.3: Al-PEO rotor masked in Suprawax 114 ready to undergo PEO coating process

After the PEO treatment, the two pieces of the Al-PEO rotor were taken out of the electrolyte bath, and the coating thickness was measured using an ultrasonic thickness gauge. The desired coating thickness was between 45μm and 50μm. The coating thickness points were checked across the different locations of the friction ring to ensure an even coating was applied. The measured coating thickness was between 48μm and 45μm.

After PEO treatment, the rubbing surfaces were cleaned with isopropanol and lightly abraded with 800-grit sandpaper before the assembled three-piece rotor underwent run-out testing on the Leeds dynamometer. The maximum run-out was measured to be no more than 0.08 mm, which was deemed satisfactory. Figure 6.4 shows the PEO rotor mounted on the UoL dynamometer before testing. The white/grey surface visible on the brake rotor is the PEO coating.

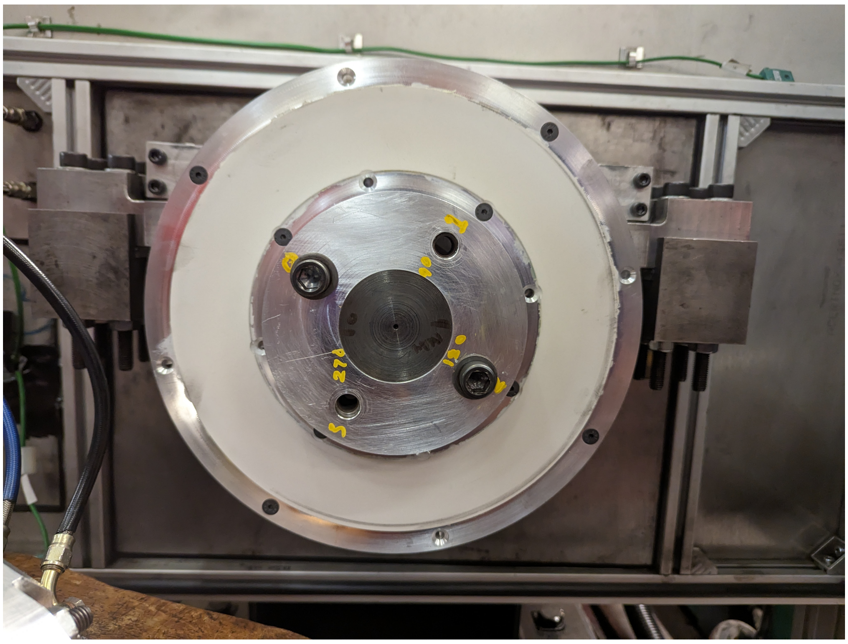

Figure 6.4: Image of PEO coated Al brake rotor

6.3 Dynamometer test results

The results associated with the brake dynamometer such as the rotor surface images, surface temperature and CoF during each test of both uncorroded and corroded rotors, are presented in this section.

6.3.1 Uncorroded Al-PEO rotor

Figure 6.5 presents surface images of the uncorroded Al-PEO rotor during the braking tests. The surface of the rotor after bedding-in, Figure 6.5B, shows slight discolouration compared to the newly coated rotor, Figure 6.5A. This darkening progresses throughout the brake tests until after the 10 bar test, the surface of the rotor has become almost black. The change in the rotor surface colour is likely to be due to the material transfer from the brake pad to the rotor.

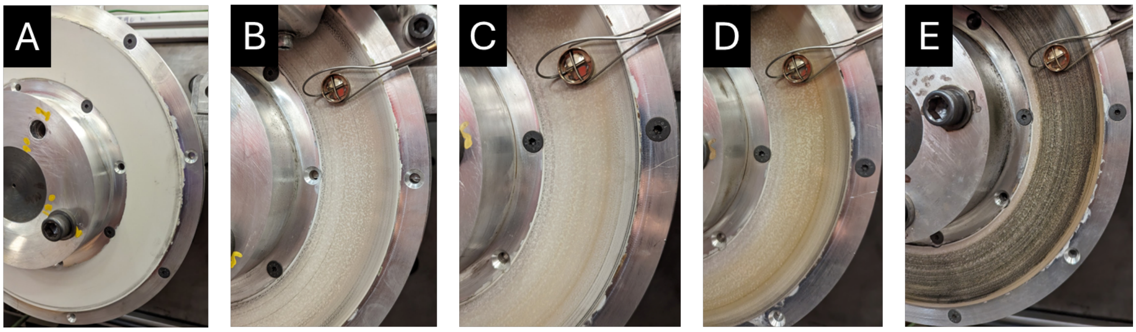

Figure 6.5: Images of uncorroded Al-PEO rotor: A) newly coated brake rotor, B) after bedding-in, C) after 5 bar, D) after 7.5 bar and E) after 10 bar

Figure 6.6 shows the surface temperature of the uncorroded Al-PEO rotor during the repeated runs at each brake pressure. The surface temperature across the three pressures achieved steady-state conditions after about 2000s, with 7.5 and 10 bars results showing more stability than for the 5 bar test. There is a clear increase in surface temperature from 5 bar to 7.5 bar, however, there is an overlap between the temperatures at the higher brake pressure of 7.5 and 10 bar. It is clear that the Al-PEO rotor reached and survived surface temperatures of at least 300°C.

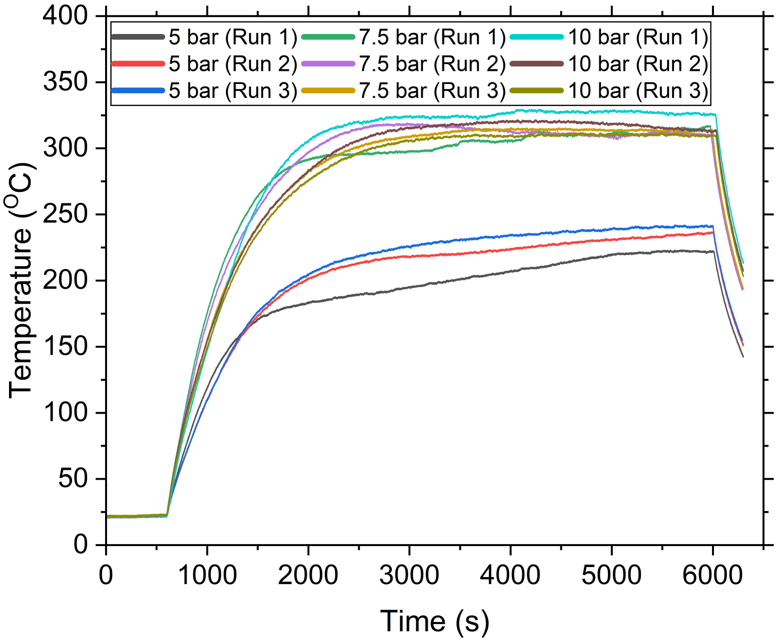

Figure 6.6: Surface temperature vs. time at 5, 7.5 and 10 bar brake pressure for Al-PEO uncorroded test

Figure 6.7 show the CoF of the uncorroded rotor. Near steady-state conditions were met after about 2000 seconds for some of the tests, whereas the final 10-bar run 3, which took nearly 3000 seconds to reach steady-state. The first 5-bar tests, which took even longer at about 4000s to reach steady state. The 5 bar test produced the highest CoF values at about 0.65, followed by the 7.5 bar test and finally the 10 bar test, where the CoF was significantly reduced to about 0.5. At each brake pressure, good consistency can be seen between the repeat tests.

The CoF for the 5 bar run 1 test initially dips and only reaches a near steady state conditions towards the end of the test. This effect can be linked to a lack of bedding-in prior to this very first proper test. This initial dip in CoF also applies to the first test at a brake pressure 7.5 bar.

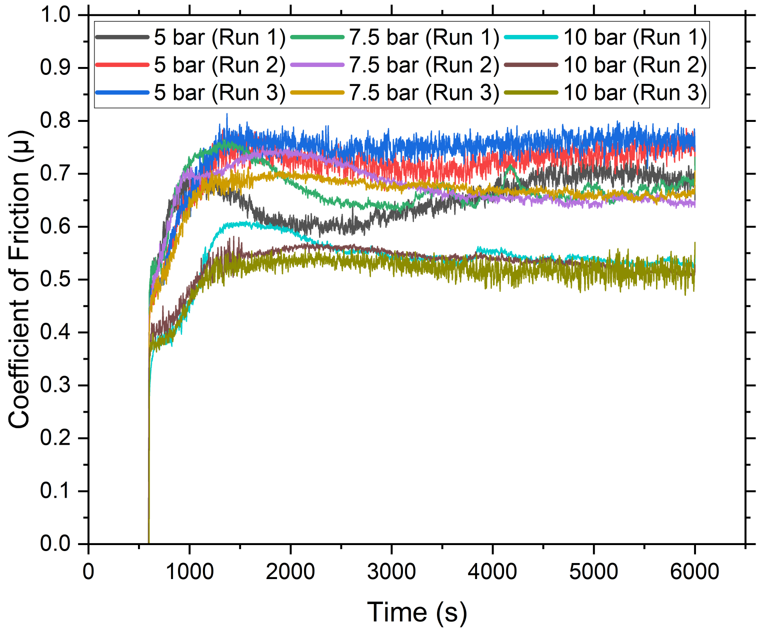

Figure 6.7: CoF vs. Time for 5, 7.5 and 10 bar brake pressure for the uncorroded test

6.3.2 Corroded Al-PEO rotor

Figure 6.8 shows images of the friction ring from the Al-PEO rotor after it was subjected to 96 hours in the salt spray chamber and at different points during the subsequent braking tests. In Figure 6.8F, the corroded Al-PEO rotor appears to have dried salt crystals on its surface. The colour of the friction ring changed from black to brownish, and some white rust (salt crystals) was also found. However, these crystals were quickly removed and the discolouration changed during the bedding-in procedure, as seen in Figure 6.8G. During the drag brake test cycles, the surface of the corroded Al-PEO rotor appears to become smoother and flatter, as shown in Figure 6.8H and I. The surface of the friction ring at the end of the 10 bar test, Figure 6.8J, seems similar to that at the end of the uncorroded test, Figure 6.5E.

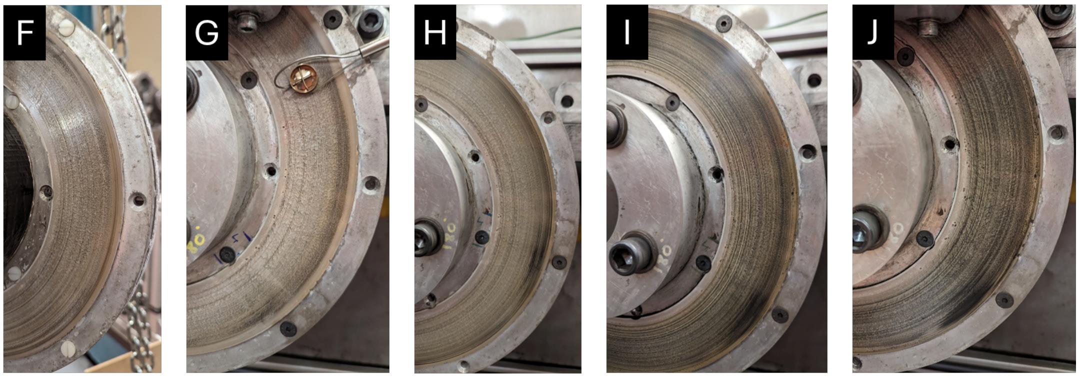

Figure 6.8: Images of corroded Al-PEO rotor: F) after 96h in the salt spray brake rotor, G) after bedding-in, H) after 5 bar, I) after 7.5 bar and J) after 10 bar

Figure 6.9 shows the surface temperature for the tests with the corroded rotor. The surface temperature increases with the brake pressure in all cases. For the majority of the test runs, steady-state conditions were achieved after about 3000s, with 5 bar run 1 stabilising later at around 4000s. This is likely due to the lack of complete bedding-in after the rotor was corroded.

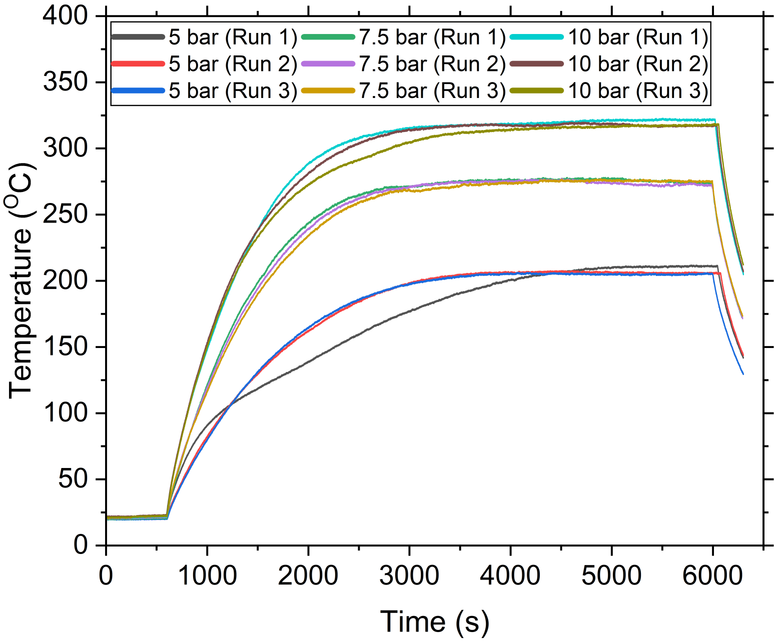

Figure 6.9: Surface temperature vs. Time for 5, 7.5 and 10 bar brake pressure for Al-PEO corroded test

Figure 6.10 shows the CoF of the corroded rotor at 5, 7.5 and 10 bar brake pressure. The CoF for 5 bar run 1 initially reduce significantly and only becomes steady-state towards the end of the test, which is correlated with the surface temperature result. Again this could be due to the lack of full bedding-in process after the corrosion treatment. The rest of the CoF results show good consistency between runs and near steady-state conditions were eventually achieved in all cases.

Figure 6.10 shows that the corroded Al-PEO rotor attained high levels of CoF, with the lowest value being 0.5 and the highest around 0.7, similar to those for the uncorroded rotor.

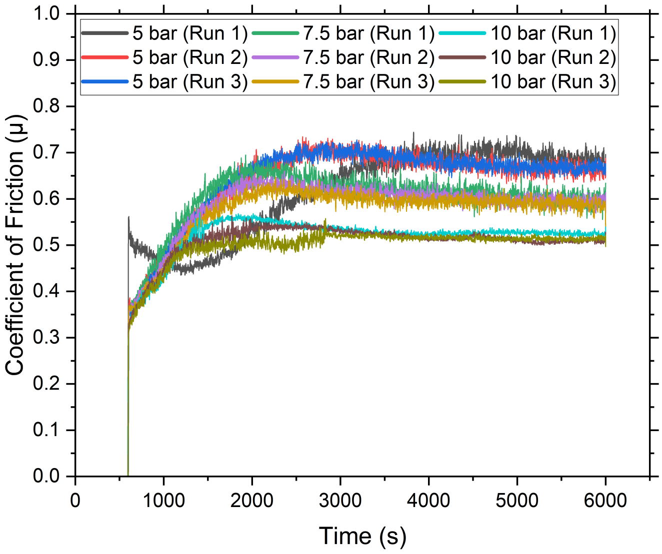

Figure 6.10: CoF vs. time at 5, 7.5 and 10 bar brake pressure for Al-PEO corroded test

6.3.3 Comparison between the uncorroded and corroded Al-PEO rotor dynamometer results

Figure 6.11 illustrates typical surface temperature measurements for the two rotor conditions. The uncorroded rotor consistently achieved higher surface temperatures compared to the corroded rotor, except at a brake pressure of 10 bar, where both the uncorroded and corroded rotors exhibited similar surface temperatures.

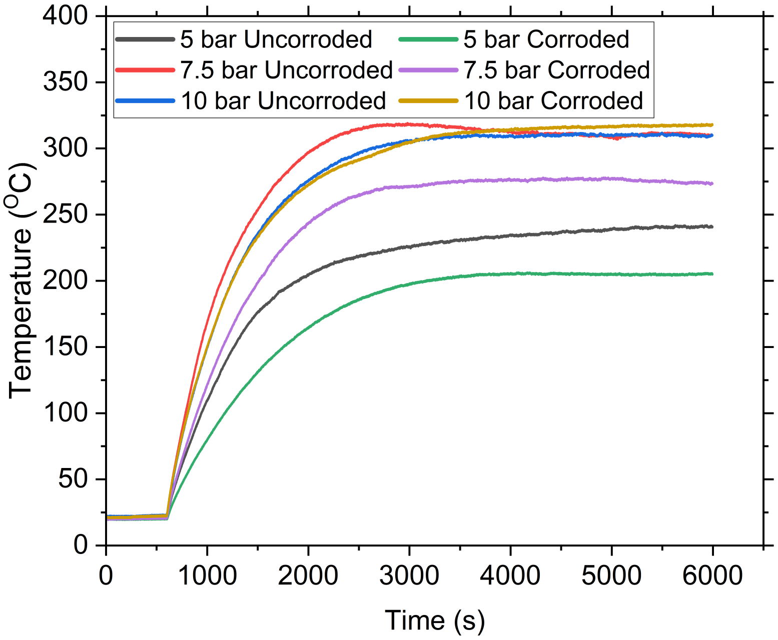

Figure 6.11: Uncorroded and corroded Al-PEO rotor surface temperature vs. time at 5, 7.5 and 10 bar brake pressure

Figure 6.12 presents typical CoF results for both uncorroded and corroded rotors. Similar to the surface temperature results, the uncorroded surface produced higher CoF values compared to the corroded rotor at both 5 and 10 bar. However at 10 bar, both the uncorroded and corroded rotor produced very similar values of CoF.

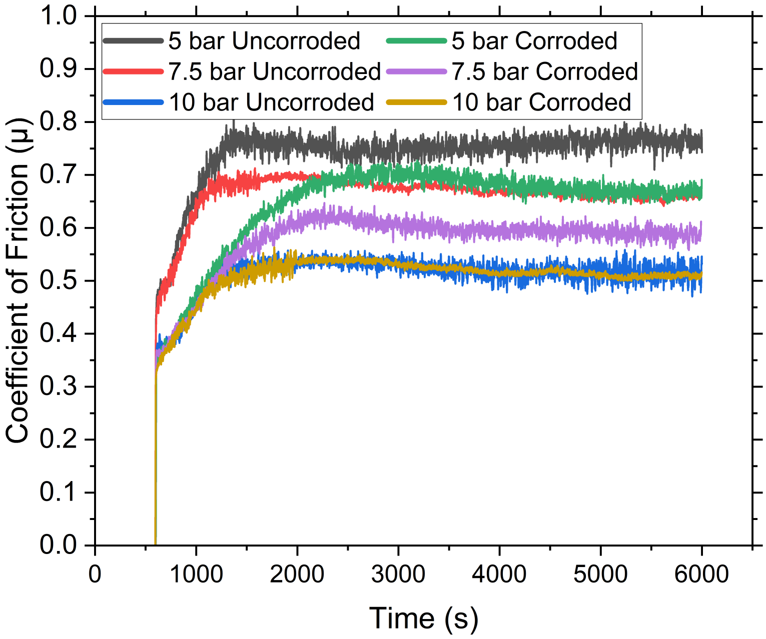

Figure 6.12: Uncorroded and corroded Al-PEO rotor CoF vs. time at 5, 7.5 and 10 bar brake pressure

6.4 Pad wear measurements

The dimensional wear loss of the brake pads against the uncorroded and corroded Al-PEO rotor is presented in Figure 6.13. It can be seen that increase in brake pressure resulted in increased pad wear as would be expected. The corroded rotor produced higher pad wear than the uncorroded rotor except at the highest brake pressure of 10 bar where the uncorroded rotor surface produced higher wear of the brake pads than the corroded surface.

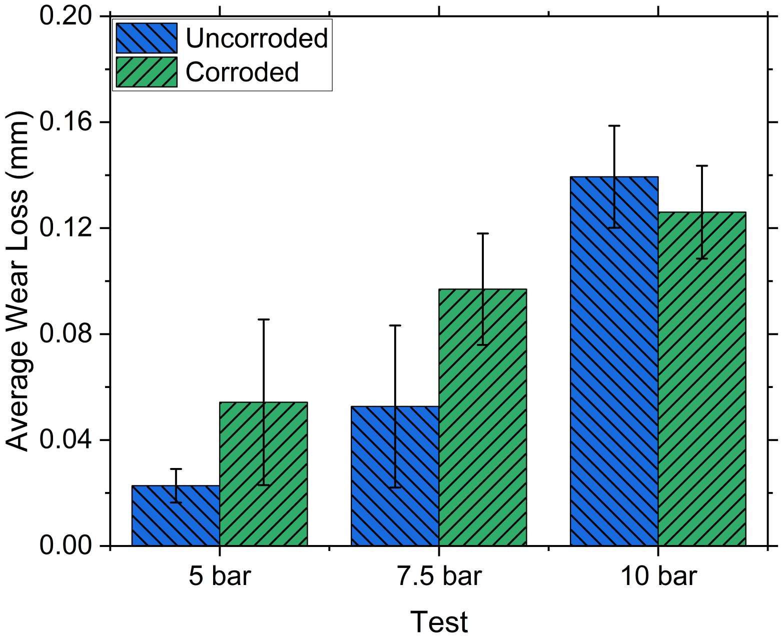

Figure 6.13: Dimensional wear loss of brake pads at 5, 7.5 and 10 bar brake line pressure for uncorroded and corroded AL-PEO rotor

The gravimetric wear loss of the pads is shown in Figure 6.14. The corroded rotor can be seen to have created more gravimetric wear of the pad than the uncorroded rotor, except at 10 bar where the pad wear results are virtually the same. This trend is similar to the dimensional wear results.

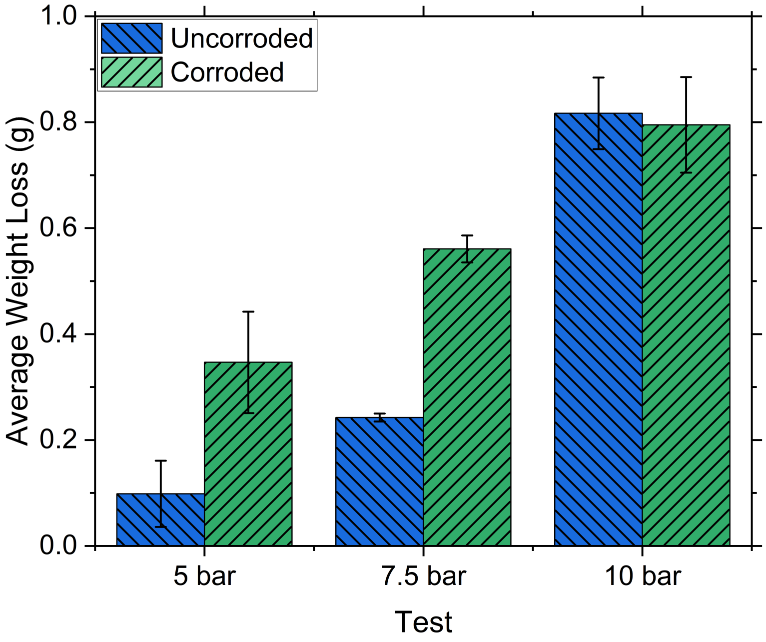

Figure 6.14: Gravimetric wear loss of brake pads at 5, 7.5 and 10 bar brake line pressure for uncorroded and corroded rotor

6.5 Particle emissions

The gravimetric particle wear emissions from the uncorroded and corroded rotor tests are presented in Figure 6.15 and Figure 6.16 for aerodynamic particle diameter sizes of PM 2.5 and PM10 respectively.

It can be seen that, at 5 bar, the corroded rotor generated slightly lower PM2.5 and PM10 emissions than the uncorroded rotor. The PM2.5 results were very similar for the two rotor surface conditions at pressures of 7.5 and 10 bar whilst, at 10 bar, PM10 emissions were significantly higher (by a factor of about 2.5) for the corroded rotor.

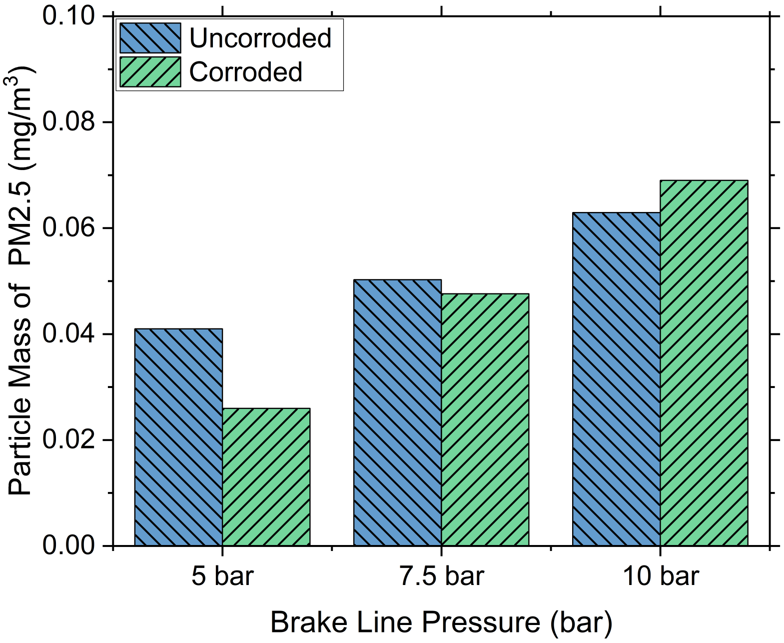

Figure 6.15: PM2.5 particle mass emissions at 5, 7.5 and 10 bar brake line pressure for uncorroded and corroded Al-PEO rotor

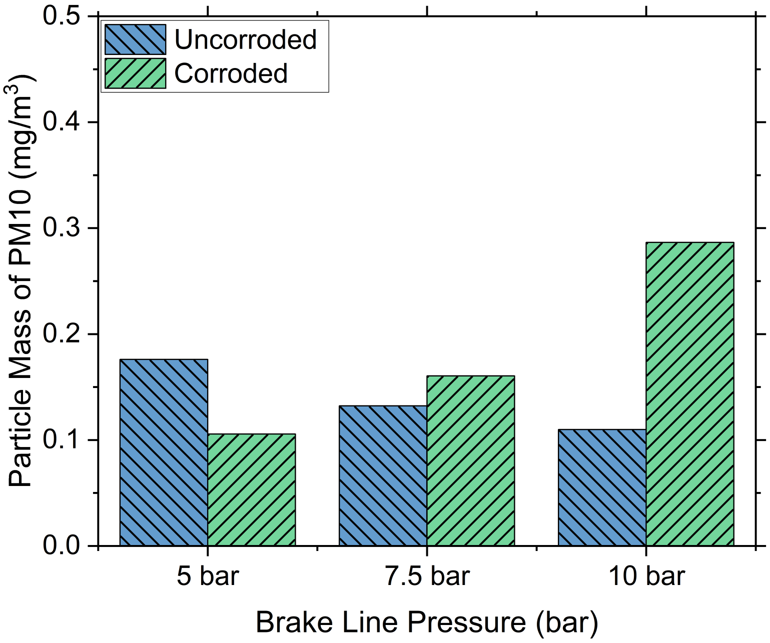

Figure 6.16: PM10 particle mass emissions at 5, 7.5 and 10 bar brake line pressure for uncorroded and corroded Al-PEO rotor

6.6 Surface analysis

6.6.1 White light interferometer

Uncorroded rotor

Figure 6.17 shows that the surface of the newly coated Al-PEO rotor prior to testing is mainly flat with just a few high and low spots, which can be attributed to the porous and uneven nature of the PEO coating.

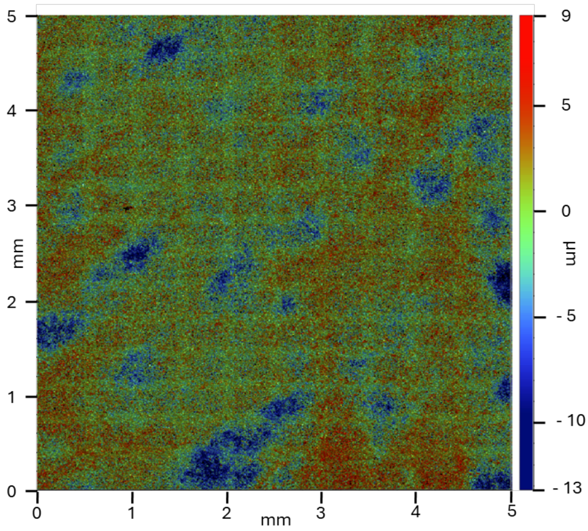

Figure 6.17: Surface topography of Al-PEO rotor after newly coated

Following the 5 bar test, the surface of the uncorroded Al-PEO rotor, as depicted in Figure 6.18a, appears largely similar to that of the untested rotor. However, after the 7.5 bar test, noticeable changes in the Al-PEO rotor's surface topography can be seen in Figure 6.18b. Hairline cracks are visible on the surface; however, these cracks do not appear to penetrate deeply into the coating or expose the underlying substrate material. After the 10 bar test, the uncorroded rotor remains relatively flat, with no significant wear scars evident on the surface, 6.18c.

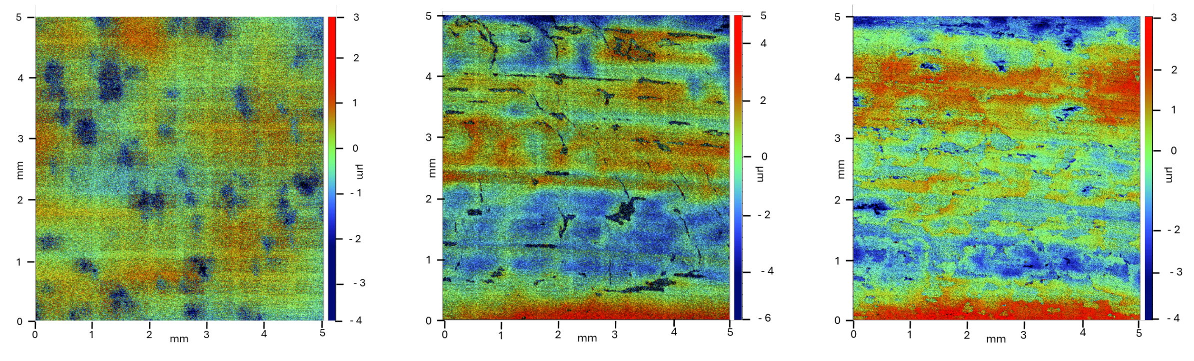

(a) 5 bar

(b) 7.5 bar

(c) 10 bar

Figure 6.18: Surface topography of uncorroded Al-PEO rotor after 5, 7.5 and 10 bar test

Corroded rotor

Figure 6.19 shows the surface topography of the corroded rotor after the 5, 7.5 and 10 bar tests. After the 5 bar test, the corroded rotor appears to have a wear scar and pits on the surface. This is likely due to the effects of corrosion. More pits can be seen on the surface of the corroded rotor after the 7.5 bar test as shown in Figure 6.19b. White light interferometer data shows that the pits are about 45μm deep. Indicating that they may have gone through the coating to the aluminium substrate since the coating thickness is generally 45μm to 50μm.

Figure 6.19C shows that, after the 10 bar test, the friction ring itself still shows flat areas with some micro-cracks on the surface. This is similar to what can be seen after the 7.5 bar test on the uncorroded rotor in Figure 6.18b.

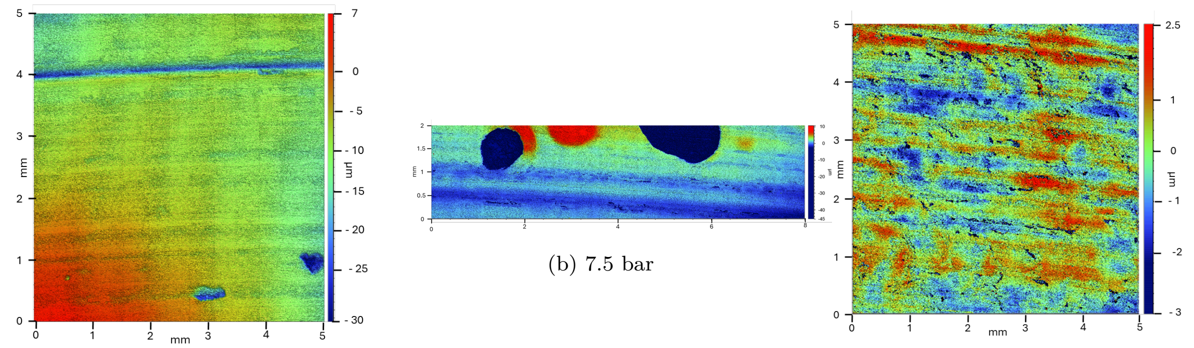

(a) 5 bar

(b) 7.5 bar

(c) 10 bar

Figure 6.19: Surface topography of corroded PEO-Al rotor after 5, 7.5 and 10 bar test

6.7 Photographic images

From the photographic image of the Al-PEO friction ring after corrosion, shown in Figure 6.20, chipping of the PEO coating is observed along the top edge of the friction ring. Additionally, spot-like features are present on the bottom edge of the friction ring. Both of these phenomena were only apparent following corrosion of the rotor. It is worth emphasising that the chips and pits are confined to the edges of the friction ring, with no such defects observed on the central rubbing surface.

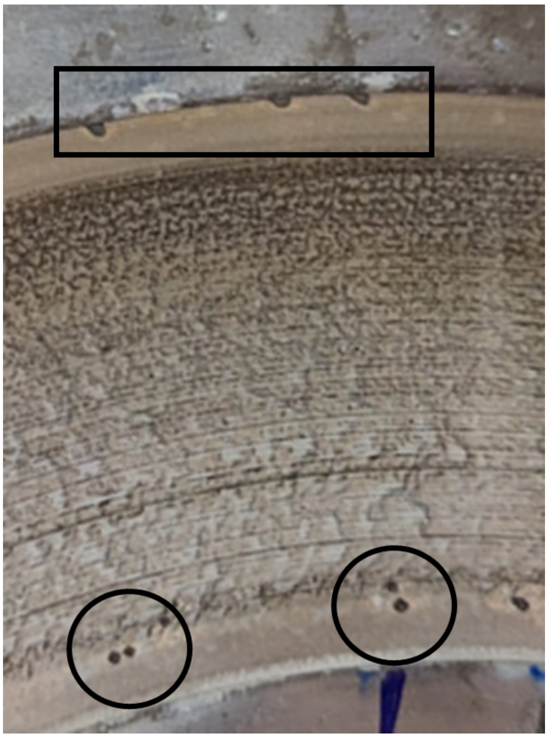

Figure 6.20: Surface image of corroded PEO coated rotor showing pits on the friction ring

6.7.1 Light microscope images

Figure 6.21 presents light microscopy images of the corroded Al-PEO rotor surface at the end of brake testing, highlighting cracks within the PEO coating. However, it is difficult to determine whether these cracks extend fully through the coating to the underlying substrate material. The surrounding areas of the coating appear to be largely unaffected by cracks, as minimal flaking or delamination is observed.

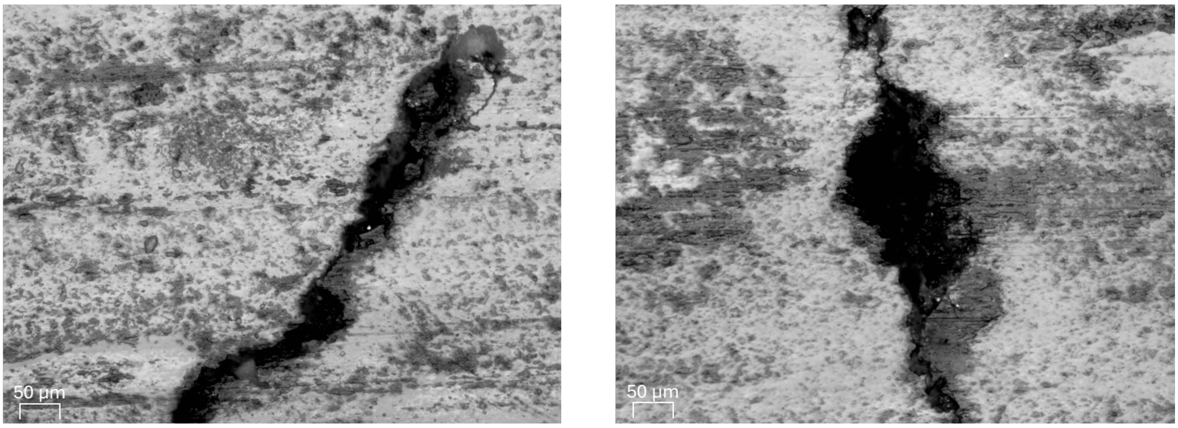

Figure 6.21: Surface cracks observed on the PEO-coated rotor under light microscope

6.7.2 Secondary electron microscope (SEM) images

Figure 6.22 presents a cross-sectional electron micrograph of the Al-PEO brake rotor following the complete brake and corrosion test protocol. The coating thickness remains approximately 45 µm, consistent with its pre-test measurement. This indicates minimal wear, strong adhesion, and preserved structural integrity. The intermetallic compounds present in the Al 6082 alloy are believed to have influenced the growth of the PEO coating, resulting in the slightly uneven interface with the substrate.

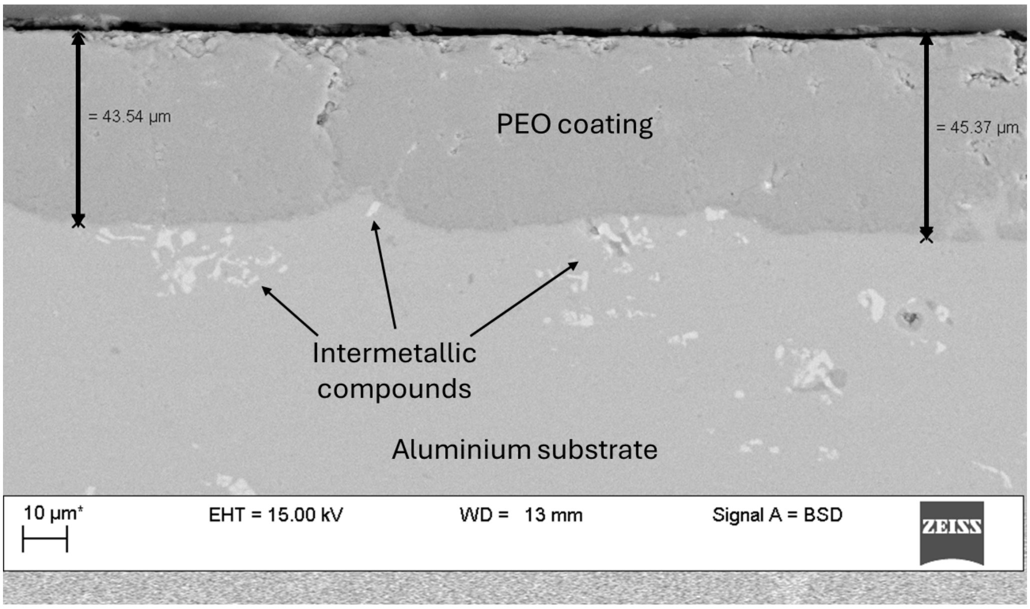

Figure 6.22: SEM image of a cross-section of PEO coating after testing

Figure 6.23 shows a cross-sectional SEM image of the outer edge of the friction ring, highlighting several potential corrosion pits. Towards the left of the image, a small area of the coating of width about 0.3 mm has locally delaminated, exposing the substrate material beneath. However, it is important to note that this delaminated has occurred at the extreme edge of the coated friction ring, where the PEO process is inherently less effective.

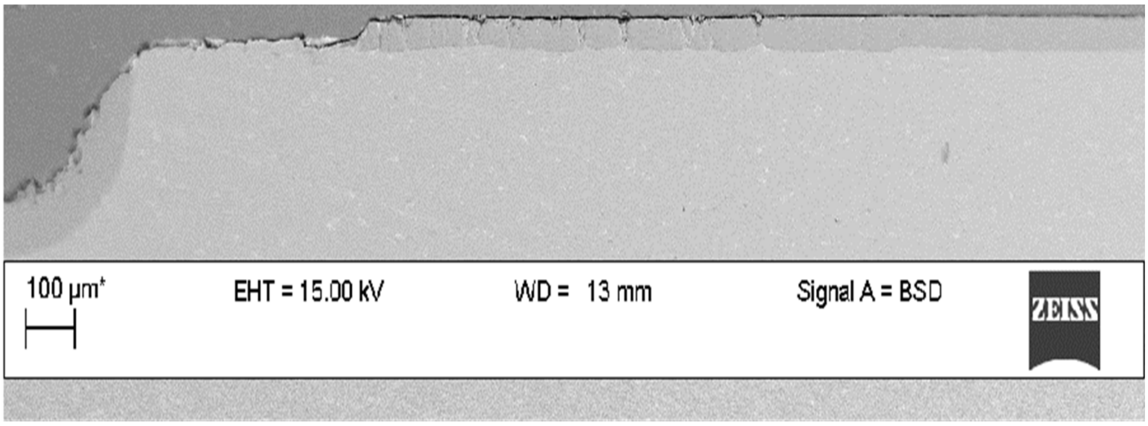

Figure 6.23: SEM image of the cross-section near the edge of the coated surface

6.8 Summary

The Al-PEO rotor was fabricated from a billet of Al-6082 alloy and designed as a three-piece assembly to facilitate easy modification of the venting system. This design also simplified the coating process, as only the friction surface required treatment. The plasma electrolytic oxidation process was performed by Curtiss-Write Keronite Ltd.

In the uncorroded conditions, the Al-PEO rotor achieved surface temperatures ranging from approximately 150°C to over 300°C, with steady-state CoF values ranging between 0.5 and nearly 0.8. After 96 hours of exposure to a salt spray environment, the rotor's braking performance exhibited a slight decline compared to the uncorroded tests. Nevertheless, it still produced respectable surface temperatures and CoF values within a similar range to those for the uncorroded rotor.

Following the corrosion testing, noticeable changes were observed on the rotor surface, including alterations in colour and the formation of pits and delaminations at the edges of the rubbing surface. The corroded Al-PEO rotor produced higher brake pad wear than its uncorroded counterpart. However, brake wear emissions remained largely unaffected by the corrosion cycle, except for a relatively small increase in PM10 particles at the highest pressure of 10 bar.

Overall, the uncorroded Al-PEO rotor demonstrated strong tribological performance up to surface temperature in excess of 300°C without any indication of coating delamination or other forms of failure. Pad wear and particulate emissions were less affected by the corrosion cycle compared to the GCI and AL-MMC rotors, as detailed in Chapters 4 and 5.

Although some pitting and surface cracking was observed on the rotor surfaces post-corrosion, this was largely restricted to the edges of the friction ring where the PEO process is less effective. More attention paid to the precise processing conditions at the edges of the PEO-treated rubbing surfaces would likely prevent such defects from occurring even under the present severe corrosion conditions.

The following chapter provides a comparative analysis and discussion of the results for the three brake rotors considered in this thesis: The GCI, Al-MMC, and Al-PEO rotors.

Chapter 7

Discussion

"The first method for estimating the intelligence of a ruler is to look at the men he has around him"

Niccolò Machiavelli

7.1 Introduction

The literature review found that much research is being carried out on particle emissions from friction brakes due to the impending Euro 7 legislation strictly limiting such emissions. However, with the increase of hybrid and fully electric vehicles on the roads, corrosion due to the lack of frequent use of friction brakes is likely to be an issue that needs to be considered when considering emissions. As there is only a small amount of research previously carried out on corrosion and its effects on brake rotors and particle wear emissions, this has created a knowledge gap which the present study has been designed to alleviate.

This chapter firstly compares and contrasts the braking performance, particle emissions, and surface characteristics of the brake rotor made from conventional GCI with those of two lightweight alternatives, namely a 30% SiC reinforced aluminium metal matrix composite (Al-MMC) and a PEO surface-treated Al 6082 alloy (Al-PEO), before and after all 3 rotors were subjected to the same severe corrosive environment. The performance of each type of rotor is then evaluated separately in the context of relevant literature, allowing for a broader understanding of their performance characteristics and positioning within the context of existing research.

7.2 Dynamometer test results

The CoF and rubbing surface temperature for the three tested brake rotors, GCI, Al-MMC, and Al-PEO in both uncorroded and corroded states are presented in Figures 7.1 and 7.2, respectively.

The data points recorded during the last run of each test were averaged for the period between the 2000s and 6000s after the start of the test, as this period represents a phase where near steady-state conditions were achieved, ensuring a more accurate and meaningful comparison of the rotor performance. The error bars in Figure 7.1 and 7.2 show the standard deviation of the output readings over this period. The Al-MMC rotor is referred to as ”MMC”, and the Al-PEO rotor is referred to as ”PEO” in Figures 7.1 and 7.2.

7.2.1 Coefficient of friction

Figure 7.1a presents the steady-state CoF of the three uncorroded brake rotors. It can be seen that the Al-PEO brake rotor produced the highest CoF values at 5 and 7.5 bar. The friction coefficients for the Al-PEO rotor at these low pressures were above 0.65, which is somewhat higher than is usual for an automotive brake, and it is possible that a stable transfer layer had not yet been fully formed on the PEO surface. All three brake rotors produced similar CoF results at the high brake pressure of 10 bar.

Figure 7.1b shows that, at 5 and 7.5 bar, the Al-PEO rotor in the corroded conditions again produced the highest steady-state CoF, while at 10 bar, the Al-MMC and Al-PEO rotors produced very similar steady-state CoF values. The corroded GCI rotor consistently produced lower CoFs than before corrosion, and the low CoF of around 0.35 measured at 10 bar might be a cause for concern in terms of the efficient operation of the GCI brake post-corrosion.

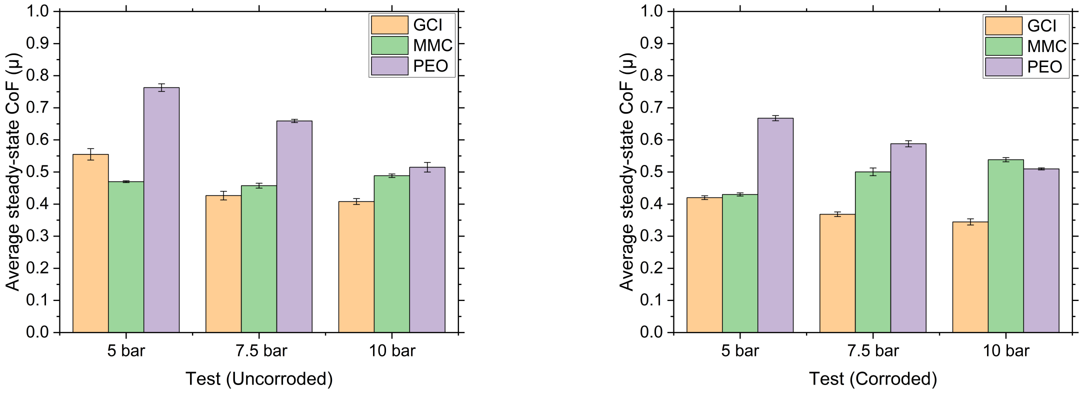

(a) Uncorroded rotor

(b) Corroded rotor

Figure 7.1: Steady-state CoF results for GCI, Al-MMC and Al-PEO brake rotors

7.2.2 Rotor surface temperature

Figure 7.2a shows the steady state surface temperature of the uncorroded GCI, Al-MMC and Al-PEO brake rotors, this was done by taking an average of the last run of each test. It can be seen that the Al-PEO rotor attained the highest surface temperature at 5 and 7.5 bar, while the Al-MMC had the lowest temperature at 5 bar. At 7.5 bar, both the GCI and Al-MMC rotors had similar surface temperatures. At the highest pressure of 10 bar, the surface temperatures of the three brake rotors were around the same. This was despite the large differences in thermal conductivity and specific heat of the different rotor materials, see Table 7.1.

After corrosion, the surface temperatures of all three rotors tended to reduce compared to the pre-corrosion values, mirroring the general reduction in CoF shown in Figure 7.1b. The corroded Al-PEO rotor produced the highest surface temperature compared to the GCI and Al-MMC rotors at all pressures, as shown in Figure 7.2b. The Al-MMC rotor had the lowest surface temperature at 5 bar, but during the 7.5 bar and 10 bar tests, it produced temperatures intermediate between those of the other two rotors. Likewise, at 7.5 and 10 bar, GCI produced the lowest surface temperatures out of the three brake rotors, but at 5 bar, produced temperatures intermediate between the Al-PEO and Al-MMC brake rotors.

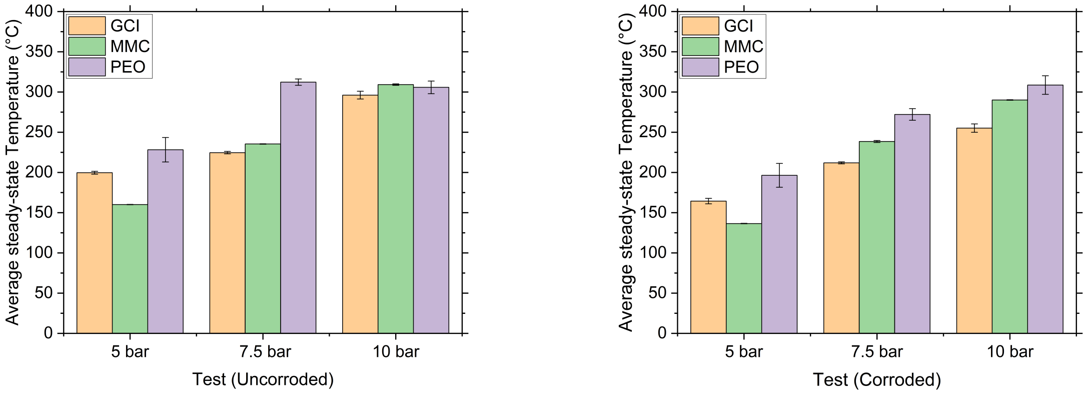

(a) Uncorroded rotor

(b) Corroded rotor

Figure 7.2: Steady-state surface temperature for GCI, Al-MMC and Al-PEO brake rotors

Figure 7.3 shows surface temperature plotted against CoF for the uncorroded and corroded brake rotors at 5, 7.5 and 10 bar of pressure. The general trend for surface temperature to increase with increasing CoF is obvious for the three brake rotors in both the uncorroded and corroded conditions. This correlation between surface temperature and CoF has been widely reported [93], [144], [145]. Given that the applied pressure and rotational speed in these drag braking tests were constant, the braking power and, hence, the rate of heat generation should be directly proportional to the mean CoF at the rubbing interface [26]. The higher the rate of heat generated, the higher the surface temperature, although this simple analysis does not account for the differing heat partition between the disc or pads and the differing rates of heat loss by conduction and convection of the different rotor materials, see Table 7.1.

It can be seen from Figure 7.3 that, especially at 5 bar, the surface temperature of the Al-PEO rotor was lower than that of GCI and Al-MMC rotors at the same CoF under both uncorroded and corroded conditions. The surface temperature of the Al-MMC also tended to be lower than that of the GCI rotor despite having similar CoF values. This is likely to be due to the higher thermal conductivity of the Al-based rotors' substrate alloy material compared to that of the GCI allowing heat to be conducted away more rapidly from the friction surface.

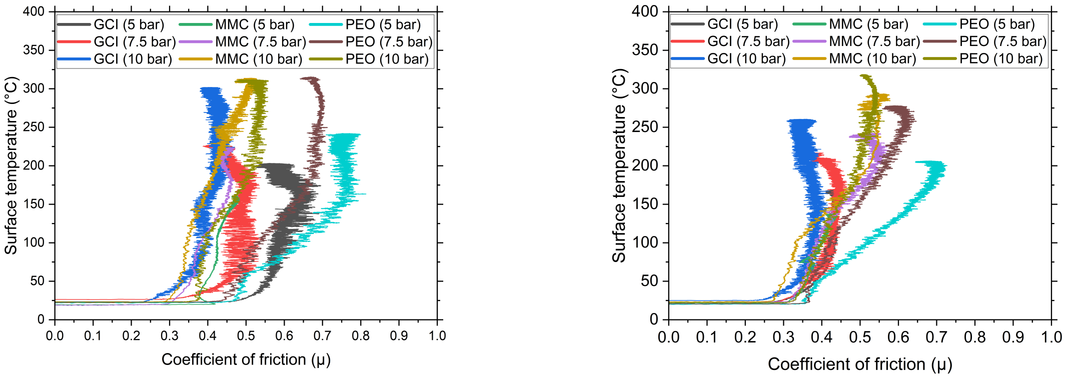

(a) Uncorroded rotors

(b) Corroded rotors

Figure 7.3: Surface temperature vs CoF loss of GCI, Al-MMC and Al-PEO uncorroded and corrosion rotor

The thermal properties of the different materials also play an important role in determining the partition of heat between the pad and the rotor at the friction interface. Typical thermal properties for the different rotor materials are illustrated in Table 7.1.

Table 7.1: Thermal properties of different materials used in brake rotors at 20°C [146]

Materials	Density (kg/m^3)	Specific heat ((J/kg K)	Conductivity (W/m K)
GCI	7200	649	53
Al-MMC	2900	800	130
Al alloy (6082)	2700	895	180
PEO coating	3030	828	1.6

For the Al-PEO rotor, the alumina coating acts as a thermal barrier due to its very low conductivity, as shown in Table 7.1. Due to this low thermal conductivity, the PEO coating acts as a thermal barrier, protecting the substrate alloy material by raising the temperature on the rotor surface and slowing down the conduction of heat into the substrate. The higher surface temperature will also allow a higher rate of heat convection and, to a lesser extent, radiation from the rotor surface to the surroundings.

Alnaqi et al. [58] generated a thermal model showing the effect of different PEO coating thicknesses. It was found that as the coating thickness increased, so did the surface temperature. The temperature at the interface between the coating and the substrate subsequently decreased, confirming that the coating does act as a thermal barrier. Alnaqi et al. also carried out experimental tests on a PEO-coated and non-coated rotor and found that the coated rotor constantly produced higher surface temperatures than the non-coated rotor under the same braking conditions.

Although the thermal barrier properties of the PEO coating will tend to raise the rotor surface temperature as indicated by Alnaqi et al. [146], the simple heat partitioning equation 7.1 suggests that the low conductivity of the PEO will also increase the heat flow into the pad and thereby tend to reduce the temperature of the disc surface. However, such a simple analysis, based solely on the bulk thermal properties of the alumina coating, takes no account of the fact that this coating is only about 50 microns thick and that the alloy substrate below has a much higher conductivity. Also, the PEO rotor very quickly developed a dark transfer layer on its surface, the thickness and thermal properties of which are unknown. More accurate calculations of the pad/disc heat partitioning effect would require much more detailed experimental and numerical analysis, which was considered outside the scope of the present work.

$$\gamma = \frac{q''_P}{q''_P + q''_R} = 1 - \frac{1}{1 + \sqrt{\frac{\rho_P c_P k_P}{\rho_R c_R k_R}}} \tag{7.1}$$

A final point about these temperature results is that, unlike the CoF, which is an average value taken over the entire pad/rotor contact patch, the temperature measured by the rubbing thermocouple is essentially a single point value. If the position of this point was changed, then so would be the measured temperature. For example, the maximum rotor temperature is likely to occur immediately behind the trailing end of the pad where it is very difficult to reliably position the thermocouple. However, any small difference in recorded temperature values due to the location of the thermocouple is unlikely to affect the relative temperatures for the different rotor materials which were all measured at the same relative position to the pad.

7.3 Pad wear

The dimensional wear loss of the brake pads against the uncorroded and corroded GCI, Al-MMC and Al-PEO rotors is presented in Figure 7.4a and 7.4b, respectively. These results represent the average thickness loss of both pads measured after the 3 tests at each pressure condition. The error bars show the standard deviation of the results from both the inboard and outboard pads.

It can be seen in Figure 7.4a that the uncorroded GCI at the 5 bar test had the highest pad wear, followed by the Al-MMC and then the Al-PEO brake rotor which produced the lowest pad wear, despite having the highest CoF as shown in Figure 7.1a. At a higher brake pressure of 7.5 bar, the pad wear of uncorroded GCI and Al-MMC brake rotors was reduced, while the pad wear for the Al-PEO rotor increased and now produced the highest pad wear. At 10 bar brake pressure, the pad wear increased for all brake rotors compared with the 5 bar results, as would be expected. GCI produces the lowest wear, followed by the Al-MMC rotor and then the Al-PEO rotor, which gave the highest pad wear recorded for any of these tests.

From the results for the corroded rotors shown in Figure 7.4b, it can be seen that the pad wear for the GCI brake rotor was constantly high throughout the brake pressure range. In contrast, the pad wear for the corroded Al-MMC and Al-PEO rotors increased with increasing brake pressure, and again, the Al-PEO rotor gave the highest wear at 10 bar.

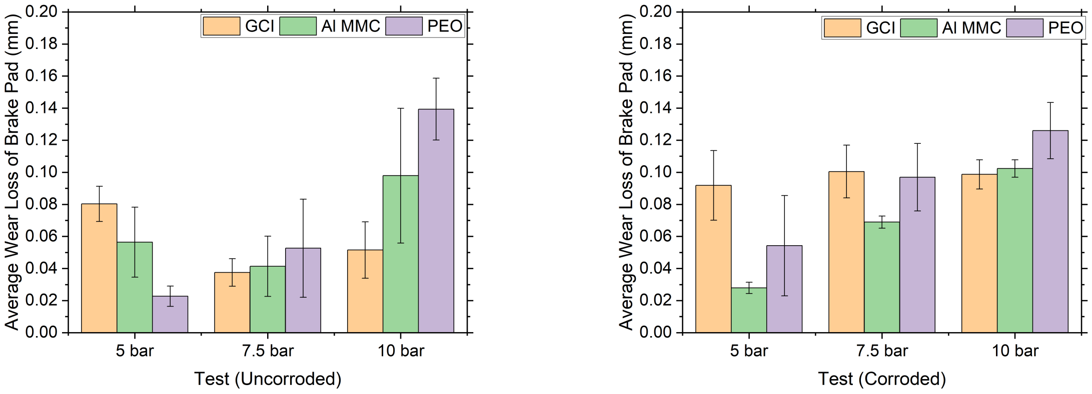

(a) Uncorroded rotors (b) Corroded rotors

Figure 7.4: Dimensional wear of brake pads against GCI, Al-MMC and Al-PEO uncorroded and corroded rotor surface

Figure 7.5 presents the gravimetric wear loss of the brake pads against the Al-MMC and Al-PEO uncorroded and corroded rotor surfaces. Again, the results represent average weight loss for both pads after the 3 tests at each pressure condition. The error bars show the standard deviation of the three repeat weight measurements for each pad, i.e. 6 measurements in total. The weight wear loss of the pads against the GCI rotor was not measured.

Figure 7.5 shows that the pad gravimetric wear loss during both the uncorroded and corroded rotor tests was consistent with the expected overall trend that, as the brake pressure increases, the friction material wears at a faster rate. This is expected because, ignoring the relatively small differences in friction coefficient, the braking power increases linearly with pressure in these constant rotating speed tests and hence the wear rate will also be expected to increase.

In the uncorroded rotor tests, Figure 7.5a shows that the gravimetric pad wear reflects the trend of the dimensional wear, with the weight loss being greatest against the Al-PEO rotor at 10 bar pressure.

For the corroded rotor tests, Figure 7.5b shows that the Al-PEO consistently produced greater pad weight loss than the Al-MMC rotor test. This is again consistent with the thickness loss measurements shown in Figure 7.4b. Although it is perhaps surprising that the wear of the same pad material was greater against the PEO surface, it should be remembered that this friction material was developed specifically to run against an MMC rotor as fitted to the Lotus Elise. It would not be expected to perform as well against a completely different surface such as the PEO alumina. Also, the heat partitioning effect mentioned above could mean that the pads were running much hotter against the PEO, and hence, the wear rate was higher. Unfortunately there was no attempt made to measure the pad temperature during the current tests.

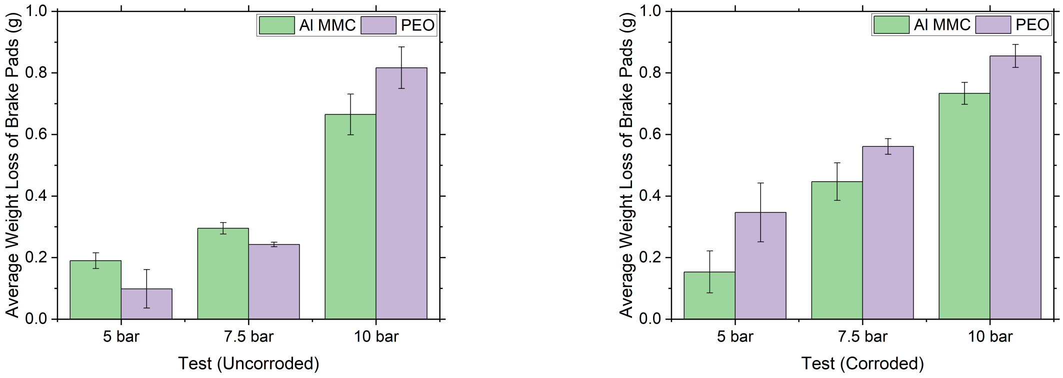

(a) Uncorroded rotors (b) Corroded rotors

Figure 7.5: Weight loss of brake pads against GCI, Al-MMC and Al-PEO uncorroded and corroded rotor surface

7.4 Particle emissions

A direct comparison should be possible between the GCI, Al-MMC and Al-PEO emissions results since all three rotors followed the same test protocol. However, the steady-state CoF values were quite different for these rotor materials, both before and after corrosion, as indicated in the histogram plots of Figure 7.1a and 7.1b. Therefore, to make a valid comparison between the different rotors, the emission results were factored by the frictional work done in the steady state period of about 60 minutes duration over which the Dekati ELPI+ measured emissions were made. These normalised results in terms of the accumulated PM2.5 and PM10 emissions from the uncorroded and corroded brake in mg divided by the estimated frictional work done in MJ over the measurement period are shown in Figures 7.6 and 7.7 for the PM2.5 and PM10 particle size range respectively. A sample calculation used to process these results from the Dekati measurements is given in Appendix A.

Figures 7.6a and 7.7a showed that at 5 and 7.5 bar, the uncorroded Al-PEO rotor produced lower emissions, especially in the larger PM10 category. In contrast, the Al-MMC rotor produced the highest particle emissions from the three brake rotors in the PM2.5 size. In the bigger PM10 size range, the GCI brake rotor produced the highest emissions at 5 bar and 7.5 bar. However, at 10 bar, there was a noticeable decrease in emissions for the uncorroded GCI in both size ranges. It may be that, at this high applied pressure, particles are less readily released from the highly compressed pad-rotor contact patch for this industry-standard friction pair, which has been optimised over many years.

Figures 7.6b and 7.7b show that the corroded Al-PEO rotor produced much lower wear emissions than the GCI and Al-MMC rotors at all pressures and in both particle size ranges of PM2.5 and PM10. Although emissions generally increased with increasing pressure for the Al-PEO, they decreased with pressure for the GCI and Al-MMC. However, the corroded Al-PEO rotor emitted the lowest emissions even at 10 bar. After the 5 bar test, the emissions measured for the corroded Al-MMC rotor dropped significantly, and it produced lower emissions than the GCI rotor at both 7.5 and 10 bar. Since the measured pad wear was generally greater for the Al-PEO rotor, whilst the wear emissions are lower in both uncorded and corroded states, it is concluded that the wear of the Al-PEO must be minimal compared with that of the other two rotor surfaces.

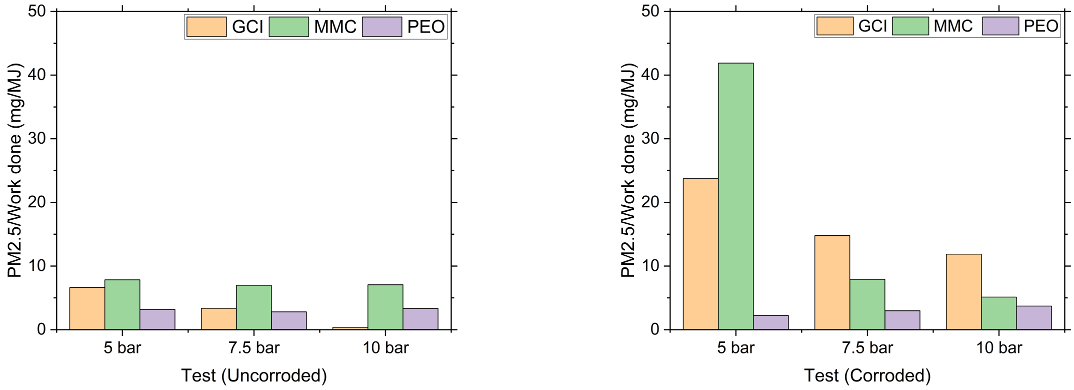

(a) Uncorroded rotors

(b) Corroded rotors

Figure 7.6: PM 2.5 particle emission per unit work done for uncorroded and corroded brake rotor surfaces

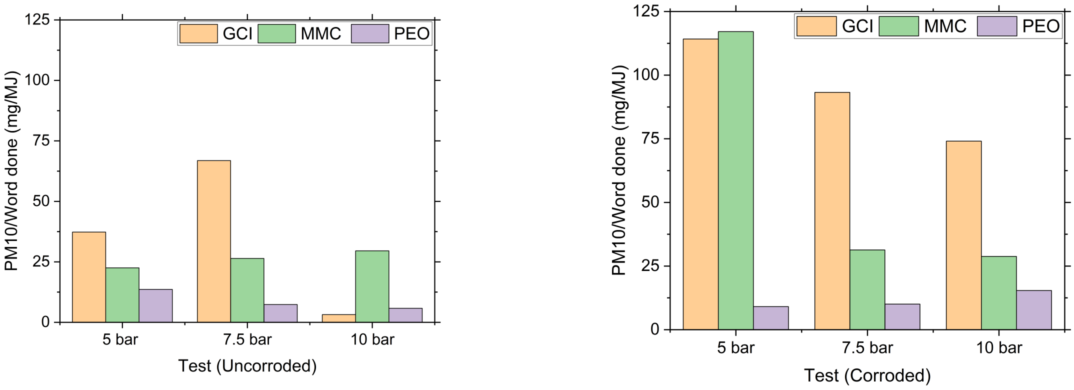

(a) Uncorroded rotors

(b) Corroded rotors

Figure 7.7: PM 10 particle emission per unit work done for uncorroded and corroded brake rotor surfaces

7.5 Surface analysis

7.5.1 Surface images

Figure 7.8 shows surface images of the GCI, Al-MMC and Al-PEO rotors at different stages throughout the uncorroded rotor tests. The GCI rotor images are labelled with ”G”, the Al-MMC is labelled ”A”, and the Al-PEO is labelled ”P”. It is apparent from these images that a noticeable darkening occurred on the friction ring surfaces of all three brake rotors. This development, which was assumed to be due to material transfer from the pad, became more noticeable as the pressure was increased.

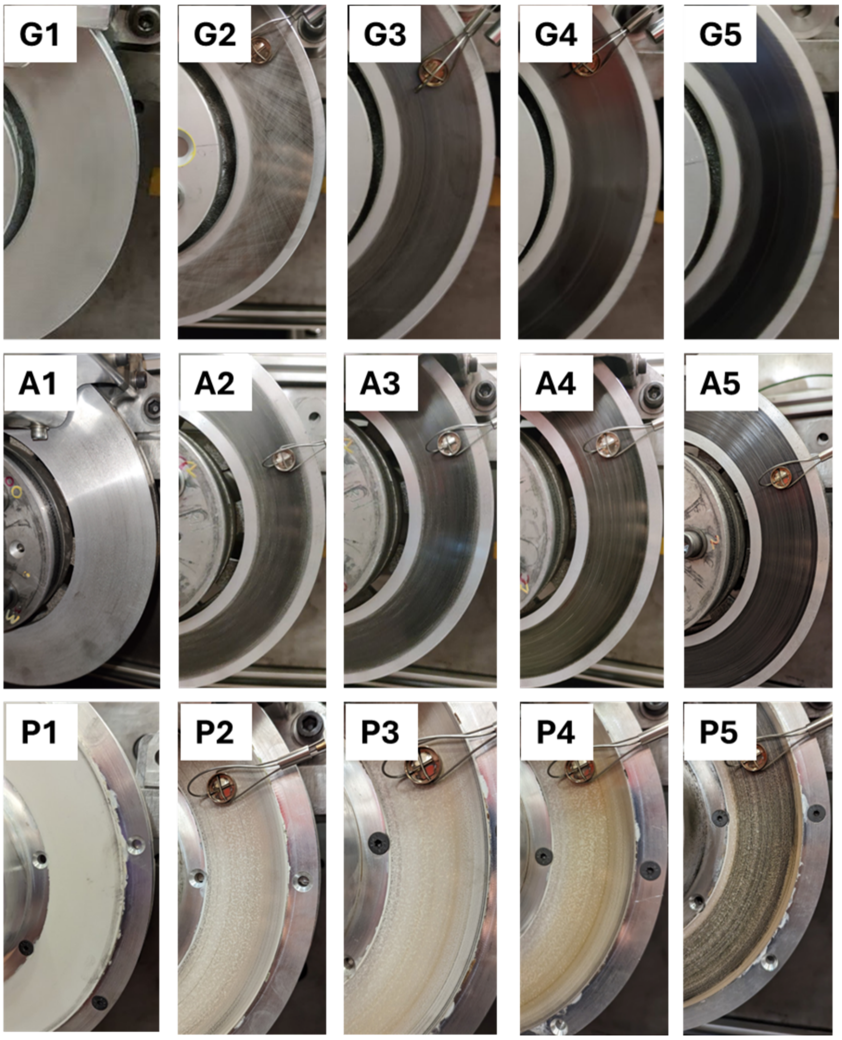

Figure 7.8: Images of uncorroded GCI, Al-MMC and Al-PEO rotors: 1) new brake rotor, 2) after bedding-in, 3) after 5 bar, 4) after 7.5 bar and 5) after 10 bar

Figure 7.9 shows the three brake rotors after exposure in the salt spray chamber for 96 hours. The GCI rotor (G6) has a red layer of corrosion products, assumed to be iron oxides. The Al-MMC rotor (A6) appeared to have a layer of salt-like deposits on its surface, presumably due to corrosion of the Al matrix. On the other hand, the Al-PEO friction surface appeared to be very similar to how it was before undergoing the corrosion cycle, indicating that the PEO layer is very resistant to corrosion. The fact that the non-PEO areas surrounding the friction ring do not appear as corroded as the Al-MMC rotor friction ring could be due to the different grades of aluminium alloy or the effects of SiC particles exposed on the surface of the Al-MMC rotor.

Overall, these images show that the Al-PEO rotor was much less affected by the corrosive environment. In contrast, the GCI rotor appeared to be the most affected, as it developed a heavy and very obvious rust layer.

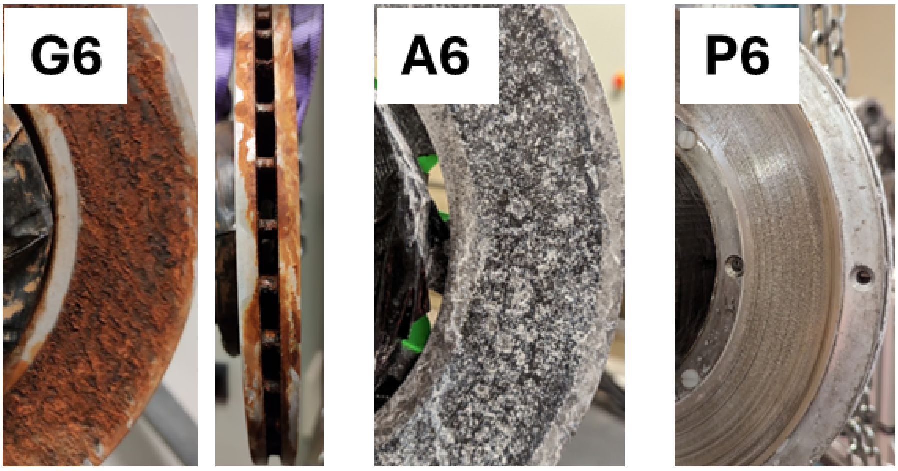

Figure 7.9: Images of GCI, Al-MMC and Al-PEO after 96h in the salt spray brake rotor

Images of the three corroded brake rotors taken during the subsequent dynamometer tests are shown in Figure 7.10. The surface images of the GCI and Al-MMC brake rotors both showed underlying marks left by the corrosion, which remained throughout the subsequent dynamometer tests. A wear band can be seen on the outer edge of the GCI rotor friction ring, perhaps indicating a non-uniform contact pressure distribution. The Al-MMC rotor appears to have wear marks across the friction rings, as shown in Figure 5.19c. For the Al-PEO rotor, very small pits are visible at the edges of the friction ring, shown in Figure 6.20. However, the main friction ring surface does not seem to have been significantly affected by the corrosion exposure.

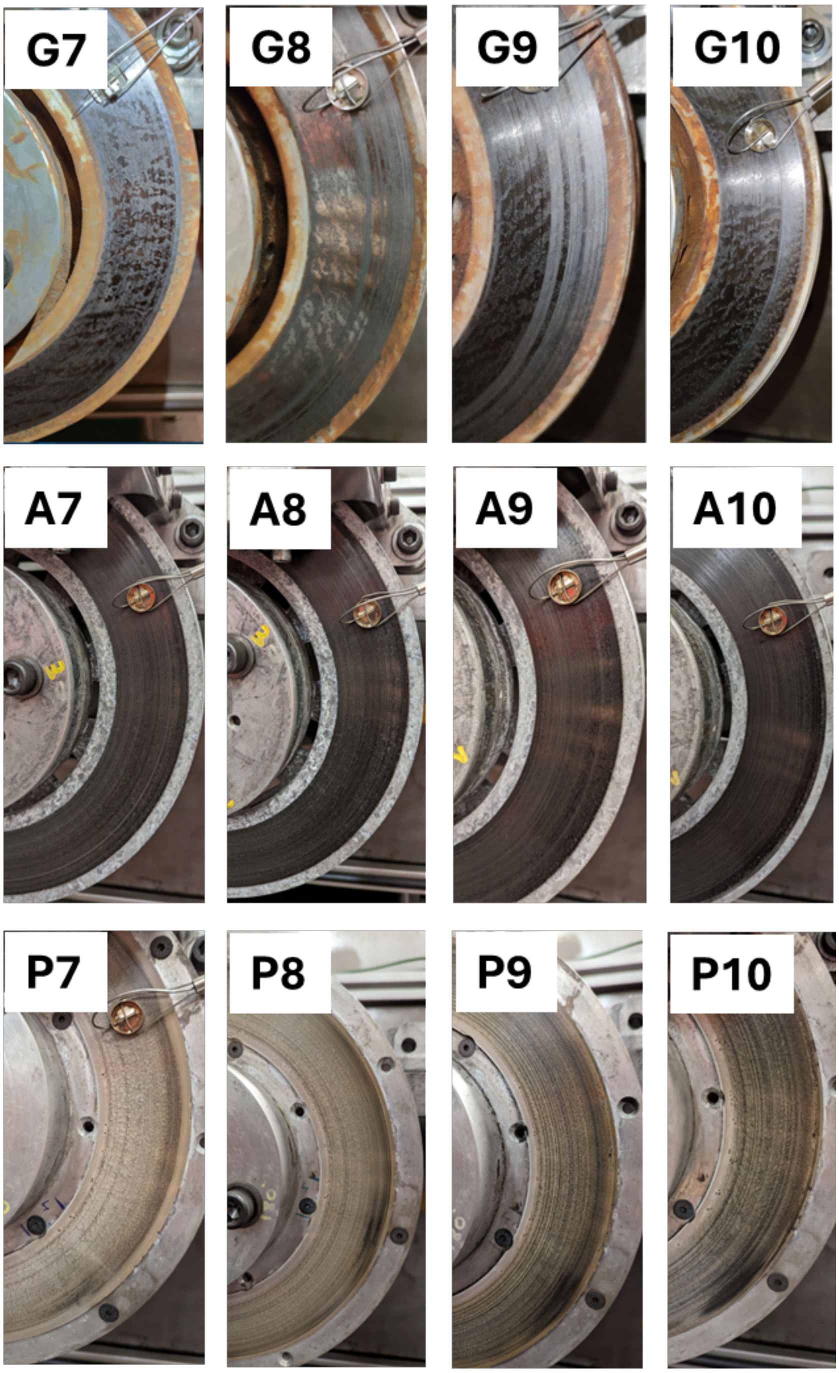

Figure 7.10: Images of corroded GCI, Al-MMC and Al-PEO rotors: 7) after bedding-in, 8) after 5 bar, 9) after 7.5 bar and 10) after 10 bar

7.5.2 Surface Topography

NpFlex surface topography images of the friction ring of all three uncorroded rotors at the end of dynamometer testing are shown in Figure 7.11. The surface topography of each rotor is quite different, despite having gone through the same brake test procedure.

The Al-MMC rotor in the centre of Figure 7.11 appears to have a large number of circumferential grooves on its surface. The depth scale on the RHS of these images shows that these wear marks are quite deep into the surface of the rotor. The GCI rotor also shows signs of circumferential wear scars, but these are less deep than for the Al-MMC. The Al-PEO surface remains flat with few signs of significant wear scars.

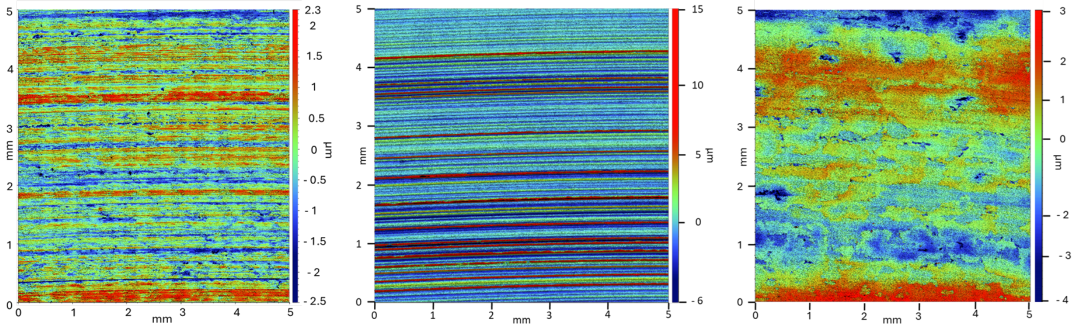

Figure 7.11: Surface images of uncorroded GCI (left), Al-MMC (middle) and Al-PEO (right) rotor after 10 bar test

The corresponding surfaces at the end of the brake tests of the corroded rotors are shown in Figure 7.12. All three brake rotors appear to have pits or other surface damage, presumably due to the effects of the corrosion exposure. The Al-PEO image shows a deep pit which, based on the scale bar to the RHS of the image, may have gone through the coating and exposed the substrate material. Pits can also be seen in both GCI and Al-MMC brake rotors, shown in Figure 4.17 and Figure 7.12. The pits on the GCI brake rotor are not as deep as those found on the Al-PEO rotor, but there are many more of them. Deep grooves and circumferential wear scars can still be seen on the surface of the corroded Al-MMC rotor.

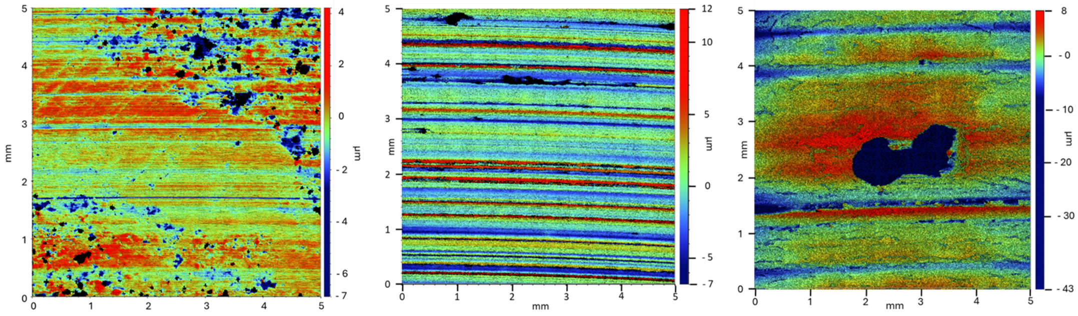

Figure 7.12: Surface images of corroded GCI (left), Al-MMC (middle) and Al-PEO (right) rotor surfaces after 10 bar test

7.5.3 SEM analysis

SEM images of sections through the rubbing surfaces of the three rotors after each completed the full test protocol are shown in Figure 7.13. It can be seen that corrosion has impacted all three rotors, with the GCI rotor having corroded graphite flakes near its surface, as indicated by the light grey colouration, and the Al-MMC showing signs of surface damage, with perhaps SiC hard particles having been removed. In the case of the GCI rotor, the corroded graphite flakes can be seen to exist at depths greater than 10 microns below the surface, and the light grey areas indicate weakened material around the flakes. The top surface of the GCI rotor image in Figure 7.13 more clearly indicates the presence of a tribolayer than for either Al-MMC or Al-PEO. In the case of Al-MMC, the removal of silicon carbide particles can be seen only at the surface level. Figure 7.13 shows that the PEO coating on the Al-PEO rotor has become delaminated and has been removed from the Al substrate, but only on the very edges of the coated area and not on the actual friction surface. However, this lamination has perhaps affected the pad and rotor pressure distribution by reducing the overall mean contact area.

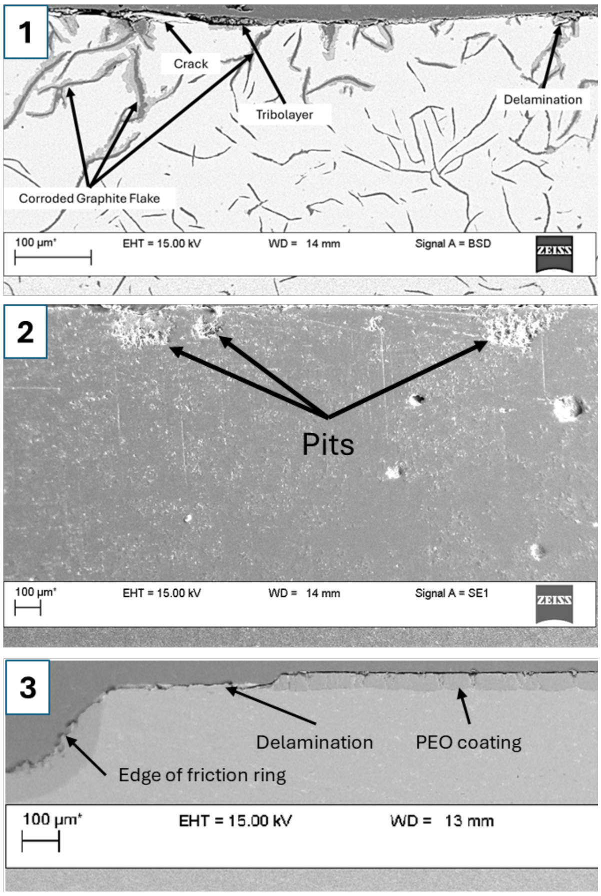

Figure 7.13: SEM images of the cross-section of 1) GCI, 2) Al-MMC and 3) Al-PEO corroded brake rotors after testing

7.6 Further discussion results

7.6.1 GCI rotor

Friction plays a crucial role in braking systems, as most foundation brakes rely on friction to slow down or stop a vehicle. Several factors influence friction, including surface temperature and wear. Developing a well-formed tribolayer is essential for achieving a stable friction and temperature regime, allowing consistent wear rate [26]. The formation and growth of a robust tribolayer can enhance the CoF and reduce wear, thereby making the bedding-in process a critical stage in establishing this tribolayer to enable good brake performance.

Oesterle et al. [96] observed that the development of a third-body layer, or tribolayer, progressively increased the CoF during the bedding-in process of a GCI rotor. Similarly, Candeo et al. [111] found that tribolayer formation contributes to stabilising the CoF. Additionally, Candeo et al. reported that both wear and particle emissions increased during the bedding-in phase as the tribolayer developed.

Surface roughness also plays a crucial role in determining the tribological properties of a brake system. In a study conducted by Okamura et al., [147], the effects of different surface textures on GCI brake rotors were investigated, focusing on their tribological behaviour during the running-in phase. The results revealed that a smoother rotor surface resulted in a higher CoF, which was attributed to increased adhesive interactions at the contact interface. On the other hand, a rougher rotor surface led to a lower CoF, as the increased surface irregularities reduced the real contact area between the rotor and the friction material. This reduction in the real contact area limited the adhesive forces, thus lowering the overall friction coefficient.

The present GCI study showed that as the brake pressure increases, the particle emissions decrease in both PM2.5 and PM10 size categories; see Figure 7.6 and 7.7. A similar study carried out by Asmawi et al. [19] found that the particle emissions in the PM10 category for a GCI rotor also decreased as the brake pressure increased. The decreasing particle emissions with the increase of brake pressure could be attributed to the reduction in CoF at higher brake pressures but may also be due to the retention of particles in the pad rotor contact area at high applied pressures.

The presence of a tribolayer affects not only the braking performance but also the formation of surface corrosion. Molina et al. [34] found that the formation of corrosion on the surface of a GCI brake rotor is not only dependent on the surface material but also on the tribolayer formed during the bedding-in process. As the brake pads used against the GCI rotor utilized a low-metallic friction material, this could explain the formation of crevices on the surface, as low-metallic brake pads contain abrasive metal fibres, and some of these fibres may have become attached to the transfer layer. However, the overriding mechanism for the high levels of corrosive products seen on the surface of the GCI rotor is assumed to be the conventional oxidation of the cast iron and embedded graphite flakes. These corrosion effects caused the particle emissions from the GCI rotor to increase considerably compared with the uncorroded surface, as shown in Figures 7.6 and 7.7.

7.6.2 Al-MMC rotor

The uncorroded Al-MMC rotor demonstrated stable CoF and relatively low pad wear at low temperatures below about 200°C. However, when temperatures exceeded 200°C, pad wear increased due to the softening of the Al matrix. As the Al softens and loses tensile strength, the SiC hard particles become more prominent and exposed on the rotor surface, leading to increased pad wear [148]. The formation of surface grooves at this stage is likely an early indication of scoring or gouging by those loose particles, as previously reported by Ahmad et al. [52]. Ahmad et al. [52] investigated a similar Al-MMC brake rotor and found that increased brake pressure led to greater deformation of the tribolayer, resulting in increased wear debris. It is thought that the accumulation of hard SiC wear debris contributed to an increase in the surface roughness of both the rotor and the brake pad, ultimately leading to the breakdown of the transfer layer.

This scouring effect is evident in both the surface image (A5) in Figure 7.8 and the NpFlex image in Figure 7.11. The increase in pad wear from both the uncorroded and corroded Al-MMC at a high brake pressure of 10 bar, shown in Figures 7.4 and 7.5, can be attributed to this phenomenon. Oda et al. [149] reported that the wear rate of a similar Al-MMC rotor increased as a result of this softening effect. Similarly, Dwivedi et al. [150] observed surface scoring at high temperatures in an Al-MMC rotor, which contributed to increased wear of both the rotor and brake pad.

The corroded Al-MMC rotor produced a greater variation in CoF compared to the uncorroded rotor. This variability is likely due to several factors, including the dislodgement of SiC particles from the Al-MMC matrix following corrosion, which not only accelerates wear but also disrupts the tribolayer, thereby affecting braking performance [151].

The formation of surface pits, combined with abrasive wear caused by the dislodged SiC particles and tribolayer degradation, was found to negatively impact friction stability and increase the overall wear rate for the corroded Al-MMC, as shown in Figures 7.4 and 7.5. Additionally, these effects contribute to higher airborne wear emissions for the corroded Al-MMC, as the breakdown of the surface layer releases more particulate matter. This explains the observed increase in emissions between the corroded and uncorroded Al-MMC rotor tests under identical braking conditions, as shown in Figure 7.6 and 7.7.

In the corroded Al-MMC study, the pits seen on the surface of the rotor are highly likely to be due to the hard particles (SiC) being pulled from the metal matrix during braking. This dislodgment of the hard particles can be seen in Figure 7.13. A study by Nunes et al. [152] found that micro-crevices and pits formed near the hard particles in the metal matrix interface after corrosion and the resulting particle removal. The increased particle pull-out is thought to be due to the SiC reinforcement particles acting as a cathodic site in the matrix, resulting in galvanic corrosion [153]–[155]. The matrix microstructure may also be affected by the corrosive environment, which can change the mechanical behaviour causing the SiC particles to be more easily pulled out of the matrix under braking conditions, as can be seen in the SEM image of the corroded Al-MMC rotor in Figure 7.13. This could result in the hard SiC particles being trapped between the pad and rotor or embedded in the brake pad, causing abrasive wear, thereby increasing the depth of the wear scars on the surface of the rotor, as can be seen in Figure 7.12. The subsequent increase in surface roughness may have disrupted the formation of the tribolayer on the rotor surface, which plays a crucial role in stabilising friction during braking [156]. This disruption could further contribute to the observed reduction in CoF, affecting overall braking performance after corrosion.

7.6.3 Al-PEO rotor

In the case of the corroded Al-PEO rotor, the cracks found on the surface of the friction ring, Figure **??**, could be attributed to the difference in thermal expansion between the PEO layer and the substrate as well as the thermal-mechanical load of the brake duty cycle. Shrestha et al. [157] reported a similar effect in the RELIABLE project in that, after the 300°C initial brake temperature (IBT) test, the PEO rotor did show signs of thermal crazing and micro-cracking on the rubbing surface. However, this did not affect the braking performance or expose the substrate material. Only after the higher IBT tests of 400°C were deep cracks found, which were thought to be due to the difference of thermal expansion between the substrate and coating as well as due to the softening of the substrate material at this high temperature.

The same corrosion test, ASTM B117 for up to 336 hours, as in the current study, was performed by Shrestha et al. [157] after both 300°C and 400°C IBT braking tests. It was observed that a white “rust” formed on the surface of the coating, which was similar to that found on the current Al-PEO rotor after it was placed in the salt spray chamber for 96 hours, Figure 7.9 A6. Shrestha et al. [157] also found that after the 300°C IBT test, the rotor showed negligible corrosion effects with just a few spots of white rust. However, after the 400ºC IBT test, the brake rotor suffered more white rust. This is thought to be due to the brake rotor suffering thermal crazing and developing cracks in the coating during the more severe braking cycles. These cracks created pathways for the salt solution to penetrate deeply through the coating and into the substrate, resulting in further damage.

Gulden et al. [50] also reported ”judder spots” on the alumina coating of an Al-PEO rotor after a thermal shock test. On closer inspection of the judder spots by SEM, cracks could be seen. The formation of these cracks was thought to be due to the large differences in thermal expansion between the coating and the substrate. The exposed edges of the cracks were found to increase pad wear. The pits and cracks found on the surface of the present rotor after corrosion could have a similar effect on pad wear and could explain the increase in emissions for the corroded Al-PEO rotor tests at high brake line pressure as shown in Figures 7.6 and 7.7.

After a PEO-coated rotor was subjected to a similar test, Gulden et al. [125] also observed something similar to the pits and cracks found in the friction ring of the present corroded Al-PEO rotor, as shown in Figure 6.21. They identified these defects as ”dimples” and performed a depth measurement that demonstrated that these dimples extend into the substrate material. This was similar to what was found in the present SEM analysis, shown in Figure 7.13, and also complies with the NpFlex analysis, Figure 7.12, which shows that the pits have penetrated the coating.

The formation of dimples or pits on the surface of the coating in the present study could be attributed to shortcomings in the PEO coating process, especially around the inner and outer radial edges of the rubbing surface. The PEO treatment was only applied on the friction surface and not over the entire rotor. Hence, these edges of the friction ring may not have been properly coated, resulting in a more porous alumina layer at these locations. This porous layer would have afforded little protection against the corrosive salt solution, allowing the Al substrate material to suffer surface corrosion effects. Hence, the vast majority of the dimples or pits found on the present coating were close to the edges of the friction ring.

The increase in wear particles emitted for the corroded Al-PEO rotor can be attributed to the disruption of the tribolayer, whether this is from corrosion pitting or severe wear scarring. The uncorroded Al-PEO rotor performed much better than the corroded rotor by producing higher and more stable CoF whilst at the same time having lower particle emissions. The increase in wear particles has been linked to the disruption of the tribolayer in other research [156], [158], [159]. The trapped wear particles generated from braking are released into the environment due to wear scars and pits, providing an easy release route.

7.6.4 Effects of pad material and other tribological influences

The friction material used against both the Al-MMC and Al-PEO brake rotors was the same. These brake pads primarily contain glass fibres in their composition, as shown in Table 5.1 and Figure 5.22a, classifying them as non-asbestos organic (NAO) pads [79]. NAO pads generally offer lower performance but few NVH problems compared to other brake pad variants, such as metallic or ceramic pads.

NAO brake pads typically exhibit low wear rates at temperatures below 220°C; however, once this threshold is exceeded, wear rates increase significantly [26]. This effect is evident in Figure 7.4, where a substantial rise in pad wear is observed between the 7.5 bar and 10 bar tests for both the uncorroded Al-MMC and Al-PEO rotors. In contrast, the GCI rotor exhibited only a slight increase in pad wear, despite all three brake rotors reaching similar surface temperatures.

One possible explanation for this difference is the type of brake pad used. The GCI rotor was paired with low-metallic brake pads, which are more thermally stable than NAO pads due to the presence of metal fibres [70]. These metal fibres help maintain performance at elevated temperatures, reducing wear compared to NAO pads at these higher temperatures.

Another factor that could contribute to the low CoF and increased wear of the corroded rotors is the breakdown of the tribolayer due to corrosion effects. Candeo et al. [111] tested a GCI rotor on a copper-free metallic brake pad and found that the dynamic formation and disruption of the tribolayer due to corrosion will result in increased wear. As the tribolayer tries to develop during braking, the crevices in the corroded surface may prevent this by its development acting as a channel for the wear particles, resulting in, for example, an increase in wear particles and a reduction in CoF.

Changes in surface roughness directly influence the contact area between the brake pad and the rotor, which also affects the braking performance. A study by Barros et al. [159] examined the effects of severe wear on a cast iron rotor. They found that under these conditions there was an abrupt reduction in contact area plateaux, an effect that occurs only during the regime of severe wear. Additionally, their study reported that the CoF increased under severe wear conditions. This can be seen in the corroded Al-MMC rotor, as it showed an increase in CoF and pad wear at 10 bar, whereas the other two corroded rotors demonstrated a reduction in CoF at higher brake pressures.

The reduction in CoF for the corroded GCI rotor can be attributed to a decrease in the real contact area between the brake pad and the rotor surface, caused by the presence of corrosion crevices, as shown in Figure 7.13. In contrast, the uncorroded GCI brake rotor had a relatively smooth surface, free from noticeable crevices or pits. For the corroded GCI rotor, these surface irregularities likely reduced the area of the actual contact points between the pad and rotor, thereby diminishing the friction force generated at the sliding interface, despite the nominal contact area and pressure remaining unchanged [95]. This reduction in contact area could partly explain the large increase in emissions seen for the corroded GCI rotor as the wear particles were more readily ejected from the contact interface.

Nogueira et al. [110] investigated the friction, wear and particle emission of copper-free metallic-based friction material against a GCI rotor. They found that the particle emissions rate is linked to the characteristics of the tribolayer and that the growth of the tribolayer is dependent on the availability of wear particles to attach to the rotor surface. However, if the tribolayer is disrupted, this allows the wear particles in the friction layer to become airborne. As suggested above, this disruption of the tribolayer and increase in emissions could also be helped by the reduced contact area between the pads and rotor.

7.7 Summary

The tried and tested GCI was generally found to perform well as a brake rotor material, demonstrating well-rounded performance when not corroded. Especially noticeable was its low PM emissions at relatively high braking pressures in its uncorroded state. However, its effectiveness diminishes significantly after exposure to severely corrosive environments. The Al-MMC, on the other hand, experienced surface scouring and damage at relatively low temperatures even in the uncorroded condition, and the corrosion treatment exacerbated this surface damage. The PEO coating on the uncorroded Al alloy brake rotor performed admirably, exhibiting good friction performance and minimal rotor wear. Additionally, it was significantly more corrosion-resistant than the other two rotor materials. The particle emissions for the PEO-coated rotor in both uncorroded and corroded states were also generally significantly lower compared to the GCI and Al-MMC rotors. Despite these advantages, the PEO coating was not without its drawbacks such as the potential for micro-cracking, pitting and delamination post-corrosion, and further refinements both of the PEO and a compatible friction material process are necessary, bearing in mind that such a rotor has yet to enter series production, unlike the other two alternatives considered.

Chapter 8

Conclusions & Recommendations for Future Work

> *"Knowledge is like money: To be of value it must circulate"*
>
> *Louis L'amour*

8.1 Conclusions

The literature review reported in Chapter 2 has highlighted very few previous studies that have examined the effect of corrosion on PM emissions from a GCI brake rotor or indeed from alternative lightweight brake rotors designed to replace GCI. The present study has therefore concentrated on the effects that severe corrosion may have on the wear emissions and basic tribology of a standard GCI rotor, as well as two lightweight alternatives, aluminium metal matrix (Al-MMC) and plasma electrolytic oxidation treated aluminium (Al-PEO) brake rotors.

The drag brake duty cycle tests conducted on the University of Leeds brake dynamometer equipped with a particle emissions capture system were found to be a reliable and repeatable means of measuring friction coefficient, rotor surface temperature, pad wear rate and PM emissions during near steady-state sliding conditions. This was considered preferable to the more complex braking duty cycles such as represented by the WLTP brake cycle, where the tribological conditions vary continuously. The corrosion cycle of 96 hours of exposure to a saltwater environment at 35°C at 95% humidity, although severe, was found to be suitable to accelerate the corrosion process to enable brake testing both before and after the rotor was exposed to this corrosive environment within a reasonable timescale.

After 96 hours of exposure to the salt spray solution, the overall trend in terms of braking performance was that the corroded GCI rotor consistently produced significantly lower CoF and rotor surface temperature than the uncorroded rotor. However, despite this reduced braking performance, the corroded GCI rotor produced at least double the mass of emission particles in both the PM2.5 and PM10 categories compared with the uncorroded rotor at 5 bar pressure and remarkably up to almost 30 times more particle mass in the PM10 category at the highest pressure of 10 bar. There are at least 2 potential reasons for this very significant increase in particle emission for the corroded GCI rotor: (1) the salt spray solution produces multiple corrosion products (mainly iron oxides) on the surface of the GCI rotor that are easily removed during brake application to increase the emitted PM, (2) even after most of these loose corrosion products have been removed, the surface of the rotor remains rougher and with obvious crevices and pits which inhibit the formation of a stable tribolayer. This corrosion-damaged surface also increases the PM emissions from the pad as indicated by the pad wear measurements which showed an increase of up to of 2.6 times the pad dimensional wear loss measured against the uncorroded surface for the same braking duty.

In the Al-MMC study, a prototype 30% SiC aluminium metal matrix rotor was tested in an identical fashion to the GCI rotor although using a different pad material more suited to the Al-MMC surface. The uncorroded Al-MMC rotor was found to be able to withstand high surface temperatures of at least 300°C under long-duration drag braking conditions during which the rotor was able to produce respectable steady-state CoF values between 0.4 and 0.6, despite showing signs of deep surface grooving. However, after the rotor was subjected to 96 hours in the salt spray bath, the surface of the rotor changed and pits appeared near the edges of the rubbing surface. The corroded Al-MMC rotor was found to produce less stable friction, lower surface temperatures, and increased the pad wear rate by up to 60% compared to the uncorroded rotor. The brake wear emissions in both PM10 and PM2.5 categories more than doubled after corrosion. This was likely due to the hard SiC particles being ejected out from the aluminium matrix after it had undergone the severe corrosion cycle. The abrasive effect of these hard particles is thought to lead to a breakdown of the tribolayer and increased wear emissions.

The final brake rotor to be tested in this study was a prototype AA6082 alloy brake rotor, the rubbing surfaces of which had received a plasma electrolytic oxidation (PEO) treatment to form a 50 micron thick alumina surface layer. The uncorroded Al-PEO rotor was able to withstand high surface temperatures of at least 300°C over long-duration drag braking conditions. The rotor was able to produce respectable steady-state CoF values between 0.5 and 0.8 against the same brake pad as used for the Al-MMC tests. After the rotor was subjected to 96 hours in the salt spray environment, the colour of the rubbing surface changed and "dimples" or pits appeared at the edges of this surface. It was found that the corroded Al-PEO rotor produced somewhat lower friction, lower surface temperatures and up to 50% increased pad wear compared with its uncorroded counterpart. However, the brake PM emissions did not significantly increase after corrosion except for PM10 particles emitted at the highest pressure of 10 bar.

Overall, all three brake rotors performed within industrial expectations of CoF with values between 0.4 and 0.8, and all rotors survived surface temperatures above 300°C in both uncorroded and corroded conditions without evidence of significant brake fade. However, all three rotors were adversely affected by corrosion. Considering only the surface appearance of each rotor, it was found that the Al-PEO rotor was the least affected by corrosion exposure, showing very little surface corrosion products or loss of coating thickness. Although there were some cracks and pits found in the coating after corrosion, the location of these defects was limited to the edges of the coated area and not on the actual friction ring itself. The Al-MMC brake rotor had obvious corrosion products on its surface after removal from the salt spray bath but these were quickly removed during the brake bedding-in process. However, during the subsequent drag brake testing, the rotor showed signs of heavy wear and surface scouring, which are thought to be due to loose SiC particles dislodged as a result of the corrosion causing the Al alloy matrix to weaken. The GCI rotor was the one most affected by corrosion. After it was taken from the salt spray chamber, the surface was found to have developed a thick flaky oxide layer (”red rust”). Although these corrosion products were largely removed from the friction surface during the bedding-in stops, the thick oxide layer remained inside the vents and would have inhibited the cooling of the rotor. In addition, even after most of the oxide layer was removed from the rubbing surface, crevices and pits were found to exist deep into the GCI surface throughout the repeated drag braking cycles.

For all rotors, the effect of corrosion not only negatively impacted the CoF, surface temperature and pad wear but also increased the particle wear emissions, especially for the GCI rotor. The corroded PEO-Al rotor produced very much lower PM10 and PM2.5 emissions, by a factor of at least 3 compared to the corroded GCI under all brake line pressure tests. The corroded Al-MMC rotor also produced significantly lower PM10 and PM2.5 emissions than the corroded GCI under all brake line pressure, except at 5 bar pressure.

The findings throughout this project suggest that potential alternative lightweight materials for brake rotors may offer distinct advantages compared with the traditional GCI. Not only do such rotors offer significant weight savings, but the lightweight Al-PEO and Al-MMC rotors considered in the present study were shown to have greater corrosion resistance compared to standard GCI and generally cause lower wear PM emissions, especially after corrosion. However, the Al-MMC rotor was found to suffer more surface damage throughout its rubbing surface due to the release of hard SiC particles from the Al matrix as a result of thermal softening of the matrix, exacerbated by the corrosion. In contrast, the corroded Al-PEO rotor only suffered significant damage to the alumina surface layer near the edges of the friction surface. However, further research and development of the PEO process and a more compatible friction material are required to enable such lightweight PEO-treated rotors to be fully acceptable as a viable alternative to the well-established and relatively cheap GCI.

This study has shown that corrosion not only affects braking performance but also significantly increases particle emissions. With the introduction of Euro 7 legislation that limits brake-related emissions, and the ongoing shift from ICE vehicles to hybrid and fully electric vehicles, the impact of corrosion on braking systems will become increasingly important. The findings indicate that alternative lightweight materials, especially when paired with protective hard coatings, offer a promising solution to either replace or complement grey cast iron rotors. These materials provide benefits such as reduced unsprung mass, lower emissions, and improved corrosion resistance, thereby advancing both material design and compliance with future regulations for braking systems.

8.2 Research limitation

Throughout this research, certain limitations have been identified and are listed below.

- One of the primary limitations of this research was the absence of a GTR-24 compliant brake emissions dynamometer and/or a brake dynamometer capable of simulating inertia. As a result, we had to choose a steady-state testing protocol, which does not accurately reflect real-world braking events or driving cycles. Additionally, we did not compare the findings to the brake emissions limits established by the Euro 7 legislation.
- Another limitation is the difference in friction materials and their surface areas. Finding friction materials that are compatible with all three brake rotors proved to be challenging due to the variations in the morphology of each rotor. This difficulty led to the selection of different friction materials. However, using different materials introduced an additional variable in the results, as the differences in tribology and emissions could be attributed to the varying friction materials. Additionally, the surface geometry of the brake pads naturally differs between the friction materials, which could have altered the contact area and pressure, impacting the overall

results.

- The bedding-in procedure was limited in producing stable results, particularly the coefficient of friction, among the three brake pressures.
- Access to a limited number of test samples for Al-MMC and Al-PEO materials was another limitation experienced in this study. The lack of additional samples prevented further trial testing and analysis, which would have required cutting the brake rotors.

8.3 Recommendations for Future Work

Following this project, there are alternative ideas, investigations, or improvements that could be explored as outlined below.

- Inducing corrosion of brake pads and rotor when in contact with each other. This would help to simulate the more real-world scenario of when the vehicle is parked with the pads still in contact with the rotor. This would be especially useful for coated rotors and metallic brake pads, to investigate if galvanic corrosion occurs and what the effects would be on the coating integrity.
- Characterisation of the PM collected on the Dekati stages by SEM, EDX, and other advanced methods would help identify the origins and nature of the wear particles produced and how these are altered after the corrosion exposure.
- Brake and corrosion tests should be conducted on different lightweight and coated brake rotor materials. PEO-Al and Al-MMC are not the only novel materials available. There are other coating applications such as laser cladding, ferritic nitrocarburising (FNC), high-voltage oxygen fuel (HVOF) or cold spraying of GCI and other rotor materials which could increase the surface hardness and corrosion resistance.
- The brake test procedure should be developed to bring it in more in line with the GTR-24 test standard for measuring brake emissions. The Leeds brake dynamometer should be upgraded to be able to simulate vehicle inertia so that it can perform a variable-speed braking duty cycle.

References

[1] BBC, *Ban on new petrol and diesel cars in UK from 2030 under PM's green plan - BBC News*. [Online]. Available: `https://www.bbc.co.uk/news/science-environment-54981425`.

[2] *Norway to 'completely ban petrol powered cars by 2025' — The Independent — The Independent*. [Online]. Available: `https://www.independent.co.uk/climate-change/news/norway-to-ban-the-sale-of-all-fossil-fuelbased-cars-by-2025-and-replace-with-electric-vehicles-a7065616.html`.

[3] *Which countries have banned petrol and diesel cars?* [Online]. Available: `https://news.trust.org/item/20201118095737-8h1uh`.

[4] *These Are The Countries Moving The Fastest To Ban Combustion Engine Cars*. [Online]. Available: `https://www.hotcars.com/fastest-countries-to-ban-combustion-engine-cars/`.

[5] OECD, *Non-exhaust Particulate Emissions from Road Transport*. OECD, **december** 2020, ISBN: 9789264452442. DOI: `10.1787/4a4dc6ca-en`. [Online]. Available: `https://www.oecd.org/en/publications/non-exhaust-particulate-emissions-from-road-transport_4a4dc6ca-en.html`.

[6] BBC, *'London throat': Toxic brake dust could cause condition, scientists say - BBC News*. [Online]. Available: `https://www.bbc.co.uk/news/uk-england-london-51049326`.

[7] P. Monks, J. Allan, D. Carruthers, D. Carslaw, G. Fuller, R. H. OBE, M. Heal, A. Lewis, E. Nemitz, M. Williams **and** C. Reeves, "AIR QUALITY EXPERT GROUP. Non-Exhaust Emissions from Road Traffic," **page** 51 014, 2013. [Online]. Available: `http://uk-air.defra.gov.uk`.

[8] K. Chau, "Pure electric vehicles," **in** *Alternative Fuels and Advanced Vehicle Technologies for Improved Environmental Performance*, Elsevier, 2014, **pages** 655–684, ISBN: 9780857095220. DOI: `10.1533/9780857097422.3.655`. [Online]. Available: `https://linkinghub.elsevier.com/retrieve/pii/B9780857095220500212`.

[9] M. Yoong, Y. Gan, G. Gan, C. Leong, Z. Phuan, B. Cheah **and** K. Chew, "Studies of regenerative braking in electric vehicle," **in** *2010 IEEE Conference on Sustainable Utilization and Development in Engineering and Technology*, IEEE, **november** 2010, **pages** 40–45, ISBN: 978-1-4244-7504-9. DOI: `10.1109/STUDENT.2010.5686984`. [Online]. Available: `http://ieeexplore.ieee.org/document/5686984/`.

[10] J. Wahlström, M. Leonardi, M. Tu, Y. Lyu, G. Perricone, S. Gialanella **and** U. Olofsson, "A study of the effect of brake pad scorching on tribology and airborne particle emissions," *Atmosphere*, **jourvol** 11, **number** 5, 2020, ISSN: 20734433. DOI: `10.3390/ATMOS11050488`.

[11] O. Aranke, W. Algenaid, S. Awe **and** S. Joshi, "Coatings for Automotive Gray Cast Iron Brake Discs: A Review," *Coatings*, **jourvol** 9, **number** 9, **page** 552, **august** 2019, ISSN: 2079-6412. DOI: `10.3390/coatings9090552`. [Online]. Available: `https://www.mdpi.com/2079-6412/9/9/552`.

[12] W. Li, X. Yang, S. Wang, J. Xiao **and** Q. Hou, "Comprehensive Analysis on the Performance and Material of Automobile Brake Discs," *Metals*, **jourvol** 10, **number** 3, **page** 377, **march** 2020, ISSN: 2075-4701. DOI: `10.3390/met10030377`. [Online]. Available: `https://www.mdpi.com/2075-4701/10/3/377`.

[13] F. Gulden, A. Stich, S. Gramstat, H. W. Höppel **and** M. Göken, "Fundamental Investigations of Aluminium Matrix Brake Rotors for the Use in Passenger Cars," **in** *Eurobrake*, 2017.

[14] I. Ghouri, R. Barker, P. Brooks, S. Kosarieh **and** D. Barton, "The Effects of Corrosion on Particle Emissions from a Grey Cast Iron Brake Disc," **in** *SAE Technical Paper Series*, **volume** 1, SAE International, Sep. 2022. DOI: `10.4271/2022-01-1178`. [Online]. Available: `https://www.sae.org/content/2022-01-1178/`.

[15] C. Houska, "Deicing Salt – Recognizing The Corrosion Threat," *TMR Consulting, Pittsburgh, PA USA*, **pages** 1–11, 2007.

[16] K. Liu, P. Xu, F. Wang, C. Jin, M. Huang, D. Dai **and** C. Fu, "Deicing efficiency analysis and economic-environment assessment of a novel induction heating asphalt pavement," *Journal of Cleaner Production*, **jourvol** 273, **page** 123 123, **november** 2020, ISSN: 09596526. DOI: `10.1016/j.jclepro.2020.123123`. [Online]. Available: `http://www.sciencedirect.com/science/article/pii/S0959652620331681%20https://linkinghub.elsevier.com/retrieve/pii/S0959652620331681`.

[17] F.-Y. Ma, "Corrosive Effects of Chlorides on Metals," **in** *Pitting Corrosion*, InTech, **march** 2012. DOI: `10.5772/32333`. [Online]. Available: `http://www.intechopen.com/books/pitting-corrosion/corrosive-effects-of-chlorides-on-metals`.

[18] E. Bowman, G. Jacobson, G. Koch, J. Varney, N. Thopson, O. Moghissi, M. Gould **and** J. Payer, "International Measures of Prevention, Application, and Economics of Corrosion Technologies Study," *NACE International*, A–19, 2016.

[19] A. Sanuddin, C. Gilkeson, P. Brooks, S. Kosarieh, D. Barton **and** S. Shrestha, "Preliminary Comparisons of Particulate Emissions Generated from Different Disc

Brake Rotors," Eurobrake, 2021, **pages** 1–7. [Online]. Available: `https://eprints.whiterose.ac.uk/177272/`.

[20] *How do car brakes work? — Haynes Publishing.* [Online]. Available: `https://haynes.com/en-gb/tips-tutorials/how-do-car-brakes-work`.

[21] *BRAKING SYSTEM: FUNDAMENTAL OF BRAKING SYSTEM.* [Online]. Available: `http://automotivesafetybrakingsystem.blogspot.com/2011/02/fundamental-of-braking-system.html`.

[22] B. Bhushan, "Principles and Applications of Tribology," *Industrial Lubrication and Tribology*, **jourvol** 51, **number** 6, **pages** 313–313, **december** 1999, ISSN: 0036-8792. DOI: `10.1108/ilt.1999.51.6.313.1`. [Online]. Available: `https://www.emerald.com/insight/content/doi/10.1108/ilt.1999.51.6.313.1/full/html`.

[23] S. Venkatesh **and** K. Murugapoopathiraja, "Scoping Review of Brake Friction Material for Automotive," *Materials Today: Proceedings*, **jourvol** 16, **pages** 927–933, 2019, ISSN: 22147853. DOI: `10.1016/j.matpr.2019.05.178`. [Online]. Available: `https://linkinghub.elsevier.com/retrieve/pii/S2214785319310247`.

[24] Brembo, *Brake Disc BREMBO COATED DISC LINE 09.C937.11 Coated, High-carbon, Internally Vented buy cheap online.* [Online]. Available: `https://www.onlinecarparts.co.uk/brembo-12812305.html`.

[25] A. J. Day, M. Tirovic **and** T. P. Newcomb, "Thermal Effects and Pressure Distributions in Brakes," *Proceedings of the Institution of Mechanical Engineers, Part D: Journal of Automobile Engineering*, **jourvol** 205, **number** 3, **pages** 199–205, Jul. 1991, ISSN: 0954-4070. DOI: `10.1243/PIME{\_}PROC{\_}1991{\_}205{\_}171{\_}02`. [Online]. Available: `http://journals.sagepub.com/doi/10.1243/PIME_PROC_1991_205_171_02`.

[26] A. Day, *Braking of Road Vehicles.* 2014, **pages** 1–472, ISBN: 9780123973382. DOI: `10.1016/C2011-0-07386-6`.

[27] G. B. Kudal **and** M. R. Chopade, "Heat Transfer Characteristics of Ventilated Disc Brake Rotor with Diamond Pillars-A Review," *International Journal of Current Engineering and Technology*, **jourvol** 4, **number** 4, **pages** 219–222, 2011. DOI: `10.14741/ijcet/22774106/spl.4.2016.45`.

[28] Brembo, *Discs — Brembo - Official Website.* [Online]. Available: `https://www.brembo.com/en/car/sporting-use/discs`.

[29] *Snub Braking Explained.* [Online]. Available: `https://www.dieselhub.com/towing/snub-braking.html`.

[30] O. Towoju, "Braking Pattern Impact on Brake Fade in an Automobile Brake System," *Journal of Engineering Sciences*, **jourvol** 2, **number** February, e11–e16, 2019, ISSN: 23122498. DOI: `10.21272/jes.2019.6(2).e2`. [Online]. Available: `http://jes.sumdu.edu.ua/wp-content/uploads/2019/04/JES_2019_02_E11-E16.pdf`.

[31] A. Akay, "Acoustics of friction," *The Journal of the Acoustical Society of America*, **jourvol** 111, **number** 4, **pages** 1525–1548, **april** 2002, ISSN: 0001-4966. DOI: `10.1121/1.1456514`. [Online]. Available: `https://pubs.aip.org/jasa/article/111/4/1525/547190/Acoustics-of-friction`.

[32] P. Ioannidis, D. C. Barton **and** P. C. Brooks, "Noise and vibration characterisation of cast iron and siliconised carbon composite brake rotors," *SAE Technical Papers*, **number** 724, 2005, ISSN: 26883627. DOI: `10.4271/2005-01-2313`.

[33] T. Budinsky, "Towards the Active Suppression of Disc Brake Squeal," Ph.D. dissertation, University of Leeds, 2018.

[34] N. Molina Montasell **and** B. Ferrer, “Brake Rotor Corrosion and Friction Cleaning Effect on Vehicle Judder Performance,” **in** *SAE Technical Papers*, **volume** 2019-Septe, Sep. 2019, **pages** 1–10. DOI: `10.4271/2019-01-2115`. [Online]. Available: `https://www.sae.org/content/2019-01-2115/`.

[35] E. A. T. Davin, A.-L. Cristol, A. Beaurain, P. Dufrénoy **and** N. Zaquen, “Differences in Wear and Material Integrity of NAO and Low-Steel Brake Pads under Severe Conditions,” *Materials*, **jourvol** 14, **number** 19, **page** 5531, Sep. 2021, ISSN: 1996-1944. DOI: `10.3390/ma14195531`. [Online]. Available: `https://www.mdpi.com/1996-1944/14/19/5531`.

[36] T. Grigoratos **and** G. Martini, “Brake wear particle emissions: a review,” *Environmental Science and Pollution Research*, **jourvol** 22, **number** 4, **pages** 2491–2504, 2015, ISSN: 16147499. DOI: `10.1007/s11356-014-3696-8`.

[37] *Ceramic vs. Metallic Brake Pads — Bridgestone Tires.* [Online]. Available: `https://www.bridgestonetire.com/tread-and-trend/drivers-ed/ceramic-vs-metallic-brake-pads`.

[38] *Brake Pads, Clutches, Gaskets.* [Online]. Available: `https://www.dupont.com/fabrics-fibers-and-nonwovens/kevlar-for-stronger-brake-pads-clutches-gaskets.html`.

[39] W. Österle **and** I. Urban, “Friction layers and friction films on PMC brake pads,” *Wear*, **jourvol** 257, **number** 1-2, **pages** 215–226, 2004, ISSN: 00431648. DOI: `10.1016/j.wear.2003.12.017`.

[40] S. Jadhav **and** S. Sawant, “A review paper: Development of novel friction material for vehicle brake pad application to minimize environmental and health issues,” *Materials Today: Proceedings*, **jourvol** 19, **pages** 209–212, 2019, ISSN: 22147853. DOI: `10.1016/j.matpr.2019.06.703`. [Online]. Available: `https://linkinghub.elsevier.com/retrieve/pii/S2214785319320772`.

[41] P. V. Gurunath **and** J. Bijwe, "Friction and wear studies on brake-pad materials based on newly developed resin," *Wear*, **jourvol** 263, **number** 7-12 SPEC. ISS. **pages** 1212–1219, 2007, ISSN: 00431648. DOI: `10.1016/j.wear.2006.12.050`.

[42] P. Blau, "Compositions, Functions, and Testing of Friction Brake Materials and Their Additives," Oak Ridge National Laboratory (ORNL), Oak Ridge, TN (United States), Tech. Rep. September, **october** 2001. DOI: `10.2172/788356`. [Online]. Available: `http://www.osti.gov/servlets/purl/788356/`.

[43] O. E. Ige, F. L. Inambao **and** G. A. Adewumi, "Effects of fiber, fillers and binders on automobile brake pad performance: A review," *International Journal of Mechanical Engineering and Technology (IJMET)*, **jourvol** 10, **number** 6, **pages** 135–150, 2019, ISSN: 0976-6359. [Online]. Available: `http://www.iaeme.com/IJMET/index.asp135http://www.iaeme.com/ijmet/issues.asp?JType=IJMET&VType=10&IType=6http://www.iaeme.com/IJMET/issues.asp?JType=IJMET&VType=10&IType=6`.

[44] R. Gilardi, L. Alzati, M. Thiam, J. F. Brunel, Y. Desplanques, P. Dufrénoy, S. Sharma **and** J. Bijwe, "Copper substitution and noise reduction in brake pads: Graphite type selection," *Materials*, **jourvol** 5, **number** 11, **pages** 2258–2269, 2012, ISSN: 19961944. DOI: `10.3390/ma5112258`.

[45] P. Kumar **and** V. K. Srivastava, "A Review on Wear and Friction Performance of Carbon–Carbon Composites at High Temperature," *International Journal of Applied Ceramic Technology*, **jourvol** 13, **number** 4, **pages** 702–710, 2016, ISSN: 17447402. DOI: `10.1111/ijac.12538`.

[46] *Thermal camera shows how hot brake rotors get during use.* [Online]. Available: `https://www.motorauthority.com/news/1109461_thermal-camera-shows-how-hot-brake-rotors-get-during-use`.

[47] G. Savage, *Carbon-Carbon Composites*, First. London: Chapman & Hall, 1993, **page** 389, ISBN: 978-94-010-4690-9. DOI: `https://doi.org/10.1007/978-94-011-1586-5`.

[48] P. J. Blau, B. C. Jolly, J. Qu, W. H. Peter **and** C. A. Blue, "Tribological investigation of titanium-based materials for brakes," *Wear*, **jourvol** 263, **number** 7-12 SPEC. ISS. **pages** 1202–1211, 2007, ISSN: 00431648. DOI: `10.1016/j.wear.2006.12.015`.

[49] W. H. Hunt, "Metal Matrix Composites," *Comprehensive Composite Materials*, **pages** 57–66, **january** 2000. DOI: `10.1016/B0-08-042993-9/00134-0`. [Online]. Available: `https://linkinghub.elsevier.com/retrieve/pii/B0080429939001340`.

[50] F. Gulden, S. Gramstat, A. Stich, H. W. Hoppel **and** U. Tetzlaff, "Properties and Limitation of an Oxide Coated Aluminum Brake Rotor," **in** *SAE Technical Papers*, **volume** 2018-Octob, **october** 2018, **pages** 1–8. DOI: `10.4271/2018-01-1877`. [Online]. Available: `https://www.sae.org/content/2018-01-1877/`.

[51] A. Thomas, N. Zervos, A. Eklund **and** S. A. Awe, "Al-matrix Composite Automotive Brake Disc Simulation of Thermomechanical Behaviour of Al-matrix Composite Automotive Brake Disc," **in** *Eurobrake 2019*, 2019.

[52] F. Ahmad, S. H. Lo, M. Aslam **and** A. Haziq, "Tribology behaviour of alumina particles reinforced aluminium matrix composites and brake disc materials," *Procedia Engineering*, **jourvol** 68, **number** 0, **pages** 674–680, 2013, ISSN: 18777058. DOI: `10.1016/j.proeng.2013.12.238`. [Online]. Available: `http://dx.doi.org/10.1016/j.proeng.2013.12.238`.

[53] Engineered Performance Coatings, *EPC provides high-quality HVOF coatings to protect and improve a components surface properties.* [Online]. Available: `https://www.ep-coatings.com/processes/hvof/?gclid=Cj0KCQjw7Nj5BRCZARIsABwxDKJeGjshhg-CN9JUthCG1oDpHUwdc0JWT9dU8iUInRh2A3b-MunhMPYaAuH5EALw_wcB`.

[54] A. Demir, R. Samur **and** I. Kiliçaslan, "Investigation of the coatings applied onto brake discs on disc-brake pad pair," *Metalurgija*, **jourvol** 48, **number** 3, **pages** 161–166, 2009, ISSN: 05435846.

[55] A. P. Krelling, M. M. d. Souza, C. E. d. Costa **and** J. C. G. Milan, "HVOF-sprayed Coating Over AISI 4140 Steel for Hard Chromium Replacement," *Materials Research*, **jourvol** 21, **number** 4, **pages** 3–12, 2018, ISSN: 1516-1439. DOI: `10.1590/1980-5373-mr-2018-0138`.

[56] A. Rogov, A. Matthews **and** A. Yerokhin, "Towards a digital twin of the plasma electrolytic oxidation process : Relaxation kinetics of PEO coatings on Al," **pages** 1–24, 2020.

[57] Keronite LTD, "Plasma Electrolytic Oxidation," *Surface Engineering*, 2019. [Online]. Available: `https://www.tekniker.es/en/plasma-electrolytic-oxidation`.

[58] A. A. Alnaqi, S. Kosarieh, D. C. Barton, P. C. Brooks **and** S. Shrestha, "Material characterisation of lightweight disc brake rotors," *Proceedings of the Institution of Mechanical Engineers, Part L: Journal of Materials: Design and Applications*, **jourvol** 232, **number** 7, **pages** 555–565, Jul. 2018, ISSN: 1464-4207. DOI: `10.1177/1464420716638683`. [Online]. Available: `http://journals.sagepub.com/doi/10.1177/1464420716638683`.

[59] M. Mathissen, T. Grigoratos, T. Lahde **and** R. Vogt, "Brake Wear Particle Emissions of a Passenger Car Measured on a Chassis Dynamometer," *Atmosphere*, **jourvol** 10, **number** 9, **page** 556, 2019, ISSN: 2073-4433. DOI: `10.3390/atmos10090556`.

[60] F. H. Farwick zum Hagen, M. Mathissen, T. Grabiec, T. Hennicke, M. Rettig, J. Grochowicz, R. Vogt **and** T. Benter, "On-road vehicle measurements of brake wear particle emissions," *Atmospheric Environment*, **jourvol** 217, **number** September, **page** 116 943, 2019, ISSN: 18732844. DOI: `10.1016/j.atmosenv.2019.116943`. [Online]. Available: `https://doi.org/10.1016/j.atmosenv.2019.116943`.

[61] J. K. Thompson, A. Marks **and** D. Rhode, “Inertia simulation in brake dynamometer testing,” *SAE Technical Papers*, **number** 724, 2002, ISSN: 26883627. DOI: `10.4271/2002-01-2601`.

[62] P. G. Sanders, N. Xu, T. M. Dalka **and** M. M. Maricq, “Airborne brake wear debris: Size distributions, composition, and a comparison of dynamometer and vehicle tests,” *Environmental Science and Technology*, **jourvol** 37, **number** 18, **pages** 4060–4069, 2003, ISSN: 0013936X. DOI: `10.1021/es034145s`.

[63] H. Hagino, M. Oyama **and** S. Sasaki, “Laboratory testing of airborne brake wear particle emissions using a dynamometer system under urban city driving cycles,” *Atmospheric Environment*, **jourvol** 131, **pages** 269–278, 2016, ISSN: 18732844. DOI: `10.1016/j.atmosenv.2016.02.014`. [Online]. Available: `http://dx.doi.org/10.1016/j.atmosenv.2016.02.014`.

[64] F. H. F. zum Hagen, M. Mathissen, T. Grabiec, T. Hennicke, M. Rettig, J. Grochowicz, R. Vogt **and** T. Benter, “Study of Brake Wear Particle Emissions: Impact of Braking and Cruising Conditions,” *Environmental Science & Technology*, **jourvol** 53, **number** 9, **pages** 5143–5150, **may** 2019, ISSN: 0013-936X. DOI: `10.1021/acs.est.8b07142`. [Online]. Available: `https://pubs.acs.org/doi/10.1021/acs.est.8b07142`.

[65] G. Perricone, V. Matějka, M. Alemani, J. Wahlström **and** U. Olofsson, “A test stand study on the volatile emissions of a passenger car brake assembly,” *Atmosphere*, **jourvol** 10, **number** 5, 2019, ISSN: 20734433. DOI: `10.3390/atmos10050263`.

[66] J. Hussain, “Thermal and material characterisation of coated lightweight disc brake rotor,” Ph.D. dissertation, University of Leeds, 2018, **page** 121. [Online]. Available: `http://journals.sagepub.com/doi/10.1177/1464420716638683`.

[67] R. R. Boyna, “Impact of friction test scale on brake friction performance,” **page** 59, 2014. [Online]. Available: `http://opensiuc.lib.siu.edu/theses/2051`.

[68] *Pin on Disk Test — About Tribology.* [Online]. Available: `https://www.tribonet.org/wiki/pin-on-disk-test/`.

[69] J. Kukutschová **and** P. Filip, "Review of Brake Wear Emissions," *Non-Exhaust Emissions*, **pages** 123–146, 2018. DOI: `10.1016/b978-0-12-811770-5.00006-6`.

[70] J. Wahlström, A. Söderberg, L. Olander, A. Jansson **and** U. Olofsson, "A pin-on-disc simulation of airborne wear particles from disc brakes," *Wear*, **jourvol** 268, **number** 5-6, **pages** 763–769, 2010, ISSN: 00431648. DOI: `10.1016/j.wear.2009.11.014`.

[71] Y. Lyu, E. Bergseth, J. Wahlström **and** U. Olofsson, "A pin-on-disc study on the tribology of cast iron, sinter and composite railway brake blocks at low temperatures," *Wear*, **jourvol** 424-425, **number** November 2018, **pages** 48–52, 2019, ISSN: 00431648. DOI: `10.1016/j.wear.2019.01.110`. [Online]. Available: `https://doi.org/10.1016/j.wear.2019.01.110`.

[72] M. Djafri, M. Bouchetara, C. Busch **and** S. Weber, "Effects of humidity and corrosion on the tribological behaviour of the brake disc materials," *Wear*, **jourvol** 321, **pages** 8–15, **december** 2014, ISSN: 00431648. DOI: `10.1016/j.wear.2014.09.006`. [Online]. Available: `http://dx.doi.org/10.1016/j.wear.2014.09.006%20https://linkinghub.elsevier.com/retrieve/pii/S004316481400283X`.

[73] P. G. Sanders, T. M. Dalka **and** R. H. Basch, "A reduced-scale brake dynamometer for friction characterization," *Tribology International*, 2001, ISSN: 0301679X. DOI: `10.1016/S0301-679X(01)00053-6`.

[74] J. O. Chung, S. R. Go, J. H. Kim, H. R. Kim **and** H. B. Choi, "Conditions for Transfer Film Formation and Its Effect on Friction Coefficients in NAO Friction Materials Containing Various Abrasive Components," *International Journal of Precision Engineering and Manufacturing*, **jourvol** 19, **number** 7, **pages** 1011–1017, 2018, ISSN: 20054602. DOI: `10.1007/s12541-018-0119-7`.

[75] K. Bhambare, M. Haffey **and** S. Jelic, “Brake duty cycle simulation for thermal design of vehicle braking system,” *SAE Technical Papers*, **jourvol** 2013, **number** January 2013, 2013, ISSN: 26883627. DOI: `10.4271/2013-36-0015`.

[76] S. A. Johnston, L. Tijerina, T. R. C. Inc, W. R. Garrott, NHTSA, D. A. Guenther, T. O. S. University, G. J. Heydinger **and** S. Inc, “Brake Testing Methodology Study - Driver Effects Testing,” **jourvol** 47, **number** March, **page** 51, 1999.

[77] Q. Jian, L. Wang **and** Y. Shui, “Thermal analysis of ventilated brake disc based on heat transfer enhancement of heat pipe,” *International Journal of Thermal Sciences*, **jourvol** 155, **page** 106 356, Sep. 2020, ISSN: 12900729. DOI: `10.1016/j.ijthermalsci.2020.106356`. [Online]. Available: `https://www.sciencedirect.com/science/article/pii/S1290072918310305?dgcid=rss_sd_all&utm_source=researcher_app&utm_medium=referral&utm_campaign=RESR_MRKT_Researcher_inbound%20https://linkinghub.elsevier.com/retrieve/pii/S1290072918310305`.

[78] M. A. Maleque, S. Dyuti **and** M. M. Rahman, “Material selection method in design of automotive brake disc,” *WCE 2010 - World Congress on Engineering 2010*, **jourvol** 3, **number** May 2014, **pages** 2322–2326, 2010, ISSN: 2078-0958.

[79] S. M. Wahid, “Automotive brake wear: a review,” *Environmental Science and Pollution Research*, **jourvol** 25, **number** 1, **pages** 174–180, 2018, ISSN: 16147499. DOI: `10.1007/s11356-017-0463-7`.

[80] M. Mathissen **and** T. Grigoratos, “D2 . 9 – New real-drive brake cycle for chassis dynamometer tests,” *A low environmental impact brake system*, 2018.

[81] M. Mathissen, J. Grochowicz, C. Schmidt, R. Vogt, F. H. Farwick zum Hagen, T. Grabiec, H. Steven **and** T. Grigoratos, “A novel real-world braking cycle for studying brake wear particle emissions,” *Wear*, **jourvol** 414-415, **pages** 219–226,

november 2018, ISSN: 00431648. DOI: `10.1016/j.wear.2018.07.020`. [Online]. Available: `https://linkinghub.elsevier.com/retrieve/pii/S004316481830557X`.

[82] K. Krishnapur, J. Luo **and** T. Kaster, "Brake squeal rig and LACT vehicle test correlation improvements - Focus on thermal conditionings," *SAE Technical Papers*, **number** 724, 2004, ISSN: 26883627. DOI: `10.4271/2004-01-2791`.

[83] J. Glisovic **and** M. Demic, "Dynamometer for testing high-frequency noise of disc brakes," **jourvol** 38, **number** 3, 2012.

[84] A. Mamakos, M. Arndt, D. Hesse **and** K. Augsburg, "Physical characterization of brake-wear particles in a PM10 dilution tunnel," *Atmosphere*, **jourvol** 10, **number** 11, 2019, ISSN: 20734433. DOI: `10.3390/atmos10110639`.

[85] SAE International, "SAE J2522," *SAE International*, **pages** 724–776, 2016.

[86] Bruker, "Efficiently Measuring the Behavior of Brake Materials Correlation Between Benchtop and Dynamometer Tests Testing Brake Materials at a Reduced Scale," **pages** 1–14, 2017.

[87] M. Mathissen, J. Grochowicz, C. Schmidt, R. Vogt, F. H. Farwick zum Hagen, T. Grabiec, H. Steven **and** T. Grigoratos, "A novel real-world braking cycle for studying brake wear particle emissions," *Wear*, **jourvol** 414-415, **number** July, **pages** 219–226, 2018, ISSN: 00431648. DOI: `10.1016/j.wear.2018.07.020`. [Online]. Available: `https://doi.org/10.1016/j.wear.2018.07.020`.

[88] X. Hua, J. Zeng, H. Li, J. Huang, M. Luo, X. Feng, H. Xiong **and** W. Wu, "A Review of Automobile Brake-by-Wire Control Technology," *Processes*, **jourvol** 11, **number** 4, **page** 994, **march** 2023, ISSN: 2227-9717. DOI: `10.3390/pr11040994`. [Online]. Available: `https://www.mdpi.com/2227-9717/11/4/994`.

[89] X. Zhao, L. Xiong, G. Zhuo, W. Tian, J. Li, Q. Shu, X. Zhao **and** G. Xu, "A Review of One-Box Electro-Hydraulic Braking System: Architecture, Control, and

Application," *Sustainability (Switzerland)*, **jourvol** 16, **number** 3, 2024, ISSN: 20711050. DOI: `10.3390/su16031049`.

[90] L. Masello, G. Castignani, B. Sheehan, F. Murphy **and** K. McDonnell, "On the road safety benefits of advanced driver assistance systems in different driving contexts," *Transportation Research Interdisciplinary Perspectives*, **jourvol** 15, **number** April, **page** 100 670, 2022, ISSN: 25901982. DOI: `10.1016/j.trip.2022.100670`. [Online]. Available: `https://doi.org/10.1016/j.trip.2022.100670`.

[91] J. K. Katiyar, S. Bhattacharya, V. K. Patel **and** V. Kumar, "Introduction of Automotive Tribology," *Energy, Environment, and Sustainability*, **pages** 3–13, 2019, ISSN: 25228374. DOI: `10.1007/978-981-15-0434-1{\_}1`.

[92] W. Österle **and** I. Urban, "Third body formation on brake pads and rotors," *Tribology International*, **jourvol** 39, **number** 5, **pages** 401–408, **may** 2006, ISSN: 0301679X. DOI: `10.1016/j.triboint.2005.04.021`. [Online]. Available: `https://linkinghub.elsevier.com/retrieve/pii/S0301679X05001477`.

[93] M. Eriksson **and** S. Jacobson, "Tribological surfaces of organic brake pads," *Tribology International*, **jourvol** 33, **number** 12, **pages** 817–827, **december** 2000, ISSN: 0301679X. DOI: `10.1016/S0301-679X(00)00127-4`. [Online]. Available: `https://linkinghub.elsevier.com/retrieve/pii/S0301679X00001274`.

[94] M. Kchaou, A. Sellami, J. Fajoui, R. Kus, R. Elleuch **and** F. Jacquemin, "Tribological performance characterization of brake friction materials: What test? What coefficient of friction?" *Proceedings of the Institution of Mechanical Engineers, Part J: Journal of Engineering Tribology*, **jourvol** 233, **number** 1, **pages** 214–226, 2019, ISSN: 2041305X. DOI: `10.1177/1350650118764167`.

[95] R. L. Machado Pinto, J. C. Horta Gutiérrez, R. B. D. Pereira, P. E. de Faria **and** J. C. C. Rubio, "Influence of Contact Plateaus Characteristics Formed on the Surface of Brake Friction Materials in Braking Performance through Experimental

Tests," *Materials*, **jourvol** 14, **number** 17, **page** 4931, **august** 2021, ISSN: 1996-1944. DOI: `10.3390/ma14174931`. [Online]. Available: `https://www.mdpi.com/1996-1944/14/17/4931`.

[96] W. Oesterle **and** A. I. Dmitriev, "Some Considerations on the Role of Third Bodies during Automotive Braking," *SAE International Journal of Passenger Cars - Mechanical Systems*, **jourvol** 7, **number** 4, **pages** 1287–1294, 2014, ISSN: 19464002. DOI: `10.4271/2014-01-2490`.

[97] W. Osterle, H. Kloß **and** A. I. Dmitriev, "Friction control during automotive braking: Experimental observations and simulation at nanometre scale," *Tribology - Materials, Surfaces and Interfaces*, **jourvol** 3, **number** 4, **pages** 196–202, 2009, ISSN: 17515831. DOI: `10.1179/175158309X12586382418454`.

[98] L. Wei, Y. Choy **and** C. Cheung, "A study of brake contact pairs under different friction conditions with respect to characteristics of brake pad surfaces," *Tribology International*, **jourvol** 138, **number** April, **pages** 99–110, **october** 2019, ISSN: 0301679X. DOI: `10.1016/j.triboint.2019.05.016`. [Online]. Available: `https://doi.org/10.1016/j.triboint.2019.05.016%20https://linkinghub.elsevier.com/retrieve/pii/S0301679X19302750`.

[99] T. Grigoratos **and** M. Giorgio, *Non-exhaust traffic related emissions. Brake and tyre wear PM.* 2014, **pages** 1–53, ISBN: 978-92-79-38303-8. DOI: `10.2790/21481`. [Online]. Available: `https://ec.europa.eu/jrc`.

[100] EPA, *Particulate Matter (PM) Basics — US EPA*. [Online]. Available: `https://www.epa.gov/pm-pollution/particulate-matter-pm-basics`.

[101] S. Hussain, M. K. Abdul Hamid, A. R. Mat Lazim **and** A. R. Abu Bakar, "Brake wear particle size and shape analysis of non-asbestos organic (NAO) and semi metallic brake pad," *Jurnal Teknologi*, **jourvol** 71, **number** 2, **pages** 129–134, 2014, ISSN: 01279696. DOI: `10.11113/jt.v71.3731`.

[102] B. Maher **and** D. Allsop, *How we discovered a possible link between car exhausts and Alzheimer's*, 2016. [Online]. Available: `https://theconversation.com/how-we-discovered-a-possible-link-between-car-exhausts-and-alzheimers-64779`.

[103] M. Gasser, M. Riediker, L. Mueller, A. Perrenoud, F. Blank, P. Gehr **and** B. Rothen-Rutishauser, "Toxic effects of brake wear particles on epithelial lung cells in vitro," *Particle and Fibre Toxicology*, **jourvol** 6, **number** 1, **page** 30, **december** 2009, ISSN: 1743-8977. DOI: `10.1186/1743-8977-6-30`. [Online]. Available: `https://particleandfibretoxicology.biomedcentral.com/articles/10.1186/1743-8977-6-30`.

[104] *Better Understanding Particulate Matter*. [Online]. Available: `https://www.thecmmgroup.com/know-thy-enemy-particulate-matter/`.

[105] The European Parlıament, "Regulation Of The European Parliament And Of The Council - on type-approval of motor vehicles and engines and of systems, components and separate technical units intended for such vehicles, with respect to their emissions and battery durability (Euro 7)," *European Union*, **jourvol** 109, **number** 23, 2024.

[106] Informal Working Group (IWG), "Non-Exhaust Brake Emissions — Laboratory testing — Part 1: Inertia Dynamometer Protocol to Measure and Characterise Brake Emissions Using the WLTP-Brake Cycle," **number** June, 2020, ISSN: 19961073. DOI: `10.1049/oap-cired.2017.1227`.

[107] Y. Lyu, M. Leonardi, J. Wahlström, S. Gialanella **and** U. Olofsson, "Friction, wear and airborne particle emission from Cu-free brake materials," *Tribology International*, **jourvol** 141, **number** September, **page** 105 959, **january** 2020, ISSN: 0301679X. DOI: `10.1016/j.triboint.2019.105959`. [Online]. Available: `https://doi.org/10.1016/j.triboint.2019.105959%20https://linkinghub.elsevier.com/retrieve/pii/S0301679X19304785`.

[108] L. Wei, Y. S. Choy, C. S. Cheung **and** D. Jin, “Tribology performance, airborne particle emissions and brake squeal noise of copper-free friction materials,” *Wear*, **jourvol** 448-449, **number** October 2019, **page** 203 215, 2020, ISSN: 00431648. DOI: `10.1016/j.wear.2020.203215`. [Online]. Available: `https://doi.org/10.1016/j.wear.2020.203215`.

[109] F. Varriale, D. Carlevaris, J. Wahlström, V. Malmborg **and** Y. Lyu, “On the impact of pad material ingredients on particulate wear emissions from disc brakes,” *Results in Engineering*, **page** 101 397, Sep. 2023, ISSN: 25901230. DOI: `10.1016/j.rineng.2023.101397`. [Online]. Available: `https://doi.org/10.1016/j.scitotenv.2020.143747%20https://linkinghub.elsevier.com/retrieve/pii/S2590123023005248`.

[110] A. P. G. Nogueira, M. Leonardi, G. Straffelini **and** S. Gialanella, “Sliding Behavior and Particle Emissions of Cu-Free Friction Materials with Different Contents of Phenolic Resin,” *Tribology Transactions*, **jourvol** 63, **number** 4, **pages** 770–779, Jul. 2020, ISSN: 1040-2004. DOI: `10.1080/10402004.2020.1753870`. [Online]. Available: `https://doi.org/10.1080/10402004.2020.1753870%20https://www.tandfonline.com/doi/full/10.1080/10402004.2020.1753870`.

[111] S. Candeo, A. Nogueira, M. Leonardi **and** G. Straffelini, “A study of friction, wear and particulate emissions during the bedding stage of a Cu-free friction material,” *Wear*, **jourvol** 486-487, **number** September, **page** 204 095, **december** 2021, ISSN: 00431648. DOI: `10.1016/j.wear.2021.204095`. [Online]. Available: `https://doi.org/10.1016/j.wear.2021.204095%20https://linkinghub.elsevier.com/retrieve/pii/S0043164821004798`.

[112] S. Gramstat, R. Waninger, D. Lugovyy **and** M. Schröder, “Friction couple investigations in terms of brake particle emissions,” *Eurobrak 2018*, **pages** 1–15, 2018, ISSN: 02637863.

[113] A. Mancini, B. Tsyupa, S. Pin, M. Bandiera, F. Bertasi, M. Federici, A. Bonfanti, G. Perricone, L. Gigli **and** E. Bolzacchini, "Chemistry of the Brake Emissions: Influence of the Test Cycle," **october** 2021, **pages** 1–9. DOI: `10.4271/2021-01-1300`. [Online]. Available: `https://www.sae.org/content/2021-01-1300/`.

[114] D. Hesse, C. Hamatschek, K. Augsburg, T. Weigelt, A. Prahst **and** S. Gramstat, "Testing of Alternative Disc Brakes and Friction Materials Regarding Brake Wear Particle Emissions and Temperature Behavior," *Atmosphere*, **jourvol** 12, **number** 4, **page** 436, **march** 2021, ISSN: 2073-4433. DOI: `10.3390/atmos12040436`. [Online]. Available: `https://www.mdpi.com/2073-4433/12/4/436`.

[115] Y. Lyu, A. Sinha, U. Olofsson, S. Gialanella **and** J. Wahlström, "Characterization of ultrafine particles from hardfacing coated brake rotors," *Friction*, **jourvol** 11, **number** 1, **pages** 125–140, **january** 2023, ISSN: 2223-7690. DOI: `10.1007/s40544-021-0585-2`. [Online]. Available: `https://link.springer.com/10.1007/s40544-021-0585-2`.

[116] L. Selley, L. Schuster, H. Marbach, T. Forsthuber, B. Forbes, T. W. Gant, T. Sandstrom, N. Camina, T. Athersuch, I. Mudway **and** A. Kumar, "Brake dust exposure exacerbates inflammation and transiently compromises phagocytosis in macrophages," 2019. DOI: `10.1002/smll.))`. [Online]. Available: `doi:%2010.1039/c9mt00253g`.

[117] X. Chu, M. Qing **and** Y. Wang, "Effect of chloride ion on metal corrosion behavior under pinhole defect of coating studied by wbe technology," *Corrosion and Protection*, **jourvol** 40, **number** 1, **pages** 23–27, 2019, ISSN: 1005748X. DOI: `10.11973/fsyfh-201901005`.

[118] K. CHANDLER **and** J. HUDSON, "Iron and Steel," **in** *Corrosion*, Elsevier, 1976, **pages** 3–3. DOI: `10.1016/B978-0-408-00109-0.50033-X`. [Online]. Available: `https://linkinghub.elsevier.com/retrieve/pii/B978040800109050033X`.

[119] K. E. Heusler, D. Landolt **and** S. Trasatti, "Electrochemical corrosion nomenclature," *Pure and Applied Chemistry*, **jourvol** 61, **number** 1, **pages** 19–22, 1989, ISSN: 13653075. DOI: `10.1351/pac198961010019`.

[120] L. SHREIR, "Basic Concepts of Corrosion," **in** *Corrosion*, Elsevier, 1976, **pages** 3–1. DOI: `10.1016/B978-0-408-00109-0.50009-2`. [Online]. Available: `https://linkinghub.elsevier.com/retrieve/pii/B9780408001090500092`.

[121] W. Tait Stephen, *An introduction to electrochemical corrosion testing for practicing engineers and scientists.* 1996, ISBN: 9780966020700. [Online]. Available: `https://books.google.co.uk/books?id=dZzyLQAACAAJ`.

[122] G. Cueva, A. Sinatora, W. Guesser **and** A. Tschiptschin, "Wear resistance of cast irons used in brake disc rotors," *Wear*, **jourvol** 255, **number** 7-12, **pages** 1256–1260, **august** 2003, ISSN: 00431648. DOI: `10.1016/S0043-1648(03)00146-7`. [Online]. Available: `https://linkinghub.elsevier.com/retrieve/pii/S0043164803001467`.

[123] K. H. Cho, J. M. Han, H. Jang, S. J. Kim, J. Y. Lee, H. D. Park, J. S. Oh **and** J. D. Lim, "Corrosion induced brake torque variation: The effect from gray iron microstructure and friction materials," *SAE Technical Papers*, **number** 724, 2005, ISSN: 26883627. DOI: `10.4271/2005-01-3919`.

[124] M. A. Hamid, A. Kaulan, S. Syahrullail **and** A. A. Bakar, "Frictional Characteristics under Corroded Brake Discs," *Procedia Engineering*, **jourvol** 68, **pages** 668–673, 2013, ISSN: 18777058. DOI: `10.1016/j.proeng.2013.12.237`. [Online]. Available: `http://dx.doi.org/10.1016/j.proeng.2013.12.237%20https://linkinghub.elsevier.com/retrieve/pii/S1877705813020912`.

[125] F. Gulden, B. Reinhold, S. Gramstat, A. Stich, U. Tetzlaff **and** H. W. Höppel, "Investigation of the run-in and corrosion behavior of a PEO-coated aluminum brake disc," **in** *10th International Munich Chassis Symposium*, 2020, **pages** 611–631. DOI: `10.1007/978-3-658-26435-2{\_}43`. [Online]. Available: `https://`

link.springer.com/chapter/10.1007/978-3-658-26435-2_43%20http://link.springer.com/10.1007/978-3-658-26435-2_43.

[126] M. Motta, L. Fedrizzi **and** F. Andreatta, "Corrosion Stiction in Automotive Braking Systems," *Materials*, **jourvol** 16, **number** 10, **page** 3710, **may** 2023, ISSN: 1996-1944. DOI: `10.3390/ma16103710`. [Online]. Available: `https://www.mdpi.com/1996-1944/16/10/3710`.

[127] W. Y. Loh, R. H. Basch, D. Li **and** P. Sanders, "Dynamic modeling of brake friction coefficients," *SAE Technical Papers*, **jourvol** 110, **pages** 2627–2636, 2000, ISSN: 26883627. DOI: `10.4271/2000-01-2753`.

[128] T. Budinsky, P. Brooks **and** D. Barton, "A new prototype system for automated suppression of disc brake squeal," *Proceedings of the Institution of Mechanical Engineers, Part D: Journal of Automobile Engineering*, **jourvol** 235, **number** 5, **pages** 1423–1433, **april** 2021, ISSN: 0954-4070. DOI: `10.1177/0954407020964624`. [Online]. Available: `http://journals.sagepub.com/doi/10.1177/0954407020964624`.

[129] J. D. Wilcox, "Isokinetic Flow and Sampling," *Journal of the Air Pollution Control Association*, **jourvol** 5, **number** 4, **pages** 226–245, **february** 1956, ISSN: 0002-2470. DOI: `10.1080/00966665.1956.10467715`. [Online]. Available: `http://www.tandfonline.com/doi/abs/10.1080/00966665.1956.10467715`.

[130] A. Sanuddin, S. Kosarieh, C. Gilkeson, P. Brooks **and** D. Barton, "Airflow Simulation and Measurement of Brake Wear Particle Emissions with a Novel Test Rig," *Jurnal Kejuruteraan*, **jourvol** si3, **number** 1, **pages** 95–101, Sep. 2020, ISSN: 22897526. DOI: `10.17576/jkukm-2020-si3(1)-15`. [Online]. Available: `http://www.ukm.my/jkukm/wp-content/uploads/2020/si3/1/15.pdf`.

[131] A. B. Sanuddin, "Particulate wear debris of coated lightweight disc brakes," Ph.D. dissertation, University of Leeds, 2020.

[132] Dekati, "Dekati ® ELPI + User Manual," 2016.

[133] Ferodo, *COAT+ Brake Discs — Ferodo.* [Online]. Available: `https://www.ferodo.co.uk/products/light-vehicles/brake-discs/coat-brake-discs.html`.

[134] D. G. Grieve, D. C. Barton, D. A. Crolla **and** J. T. Buckingham, "Design of a lightweight automotive brake disc using finite element and Taguchi techniques," *Proceedings of the Institution of Mechanical Engineers, Part D: Journal of Automobile Engineering*, **jourvol** 212, **number** 4, **pages** 245–254, **april** 1998, ISSN: 0954-4070. DOI: `10.1243/0954407981525939`. [Online]. Available: `http://journals.sagepub.com/doi/10.1243/0954407981525939`.

[135] A. A. Alnaqi, S. Shrestha, D. C. Barton **and** P. C. Brooks, "Optimisation of Alumina Coated Lightweight Brake Rotor," **in** *SAE Technical Papers*, **volume** 2014-Septe, Sep. 2014. DOI: `10.4271/2014-01-2501`. [Online]. Available: `https://www.sae.org/content/2014-01-2501/`.

[136] ASTM International, *B117 Operating Salt Spray (Fog) Apparatus*, 2011. DOI: `10.1520/B0117-11`.

[137] Anon, *Give brakes a break — Ferodo.* [Online]. Available: `https://www.ferodo.com/en-gb/blog/give-brakes-a-break.html`.

[138] SAE International, "Brake Pads, Lining, Disc, and Drum Wear Measurements (SAE J2986)," *SAE International*, 2019. DOI: `https://doi.org/10.4271/J2986{\_}201901`. [Online]. Available: `https://saemobilus.sae.org/content/J2986_201901`.

[139] S. Rhee, M. Jacko **and** P. Tsang, "The role of friction film in friction, wear and noise of automotive brakes," *Wear*, **jourvol** 146, **number** 1, **pages** 89–97, **may** 1991, ISSN: 00431648. DOI: `10.1016/0043-1648(91)90226-K`. [Online]. Available: `https://linkinghub.elsevier.com/retrieve/pii/004316489190226K`.

[140] A. Orłowicz, M. Mróz, G. Wnuk, O. Markowska, W. Homik **and** B. Kolbusz, “Coefficient of Friction of a Brake Disc-Brake Pad Friction Couple,” *Archives of Foundry Engineering*, **jourvol** 16, **number** 4, **pages** 196–200, **december** 2016, ISSN: 2299-2944. DOI: `10.1515/afe-2016-0109`. [Online]. Available: `http://journals.pan.pl/dlibra/publication/117378/edition/102054/content%20http://journals.pan.pl/dlibra/publication/117273/edition/101953/content`.

[141] D. Hesse **and** C. Hamatschek, “Investigations on the Deposition Behaviour of Brake Wear Particles on the Wheel Surface,” **pages** 1–13, 2021. DOI: `10.4271/2021-01-1301.Abstract`.

[142] W. Österle, M. Griepentrog, T. Gross **and** I. Urban, “Chemical and microstructural changes induced by friction and wear of brakes,” *Wear*, **jourvol** 250-251, **number** PART 2, **pages** 1469–1476, 2001, ISSN: 00431648. DOI: `10.1016/s0043-1648(01)00785-2`.

[143] S. Rhee, D. Sharma, S. R. Singh **and** A. Rathee, “An Investigation of the Role of Wear and Friction Film Influencing the Friction Coefficient of Brakes: Mechanism of Brake Fade,” **in** *SAE Technical Paper Series*, **volume** 1, **october** 2020, **pages** 1–17. DOI: `10.4271/2020-01-1630`. [Online]. Available: `https://www.sae.org/content/2020-01-1630/`.

[144] S. Fan, L. Zhang, L. Cheng, G. Tian **and** S. Yang, “Effect of braking pressure and braking speed on the tribological properties of C/SiC aircraft brake materials,” *Composites Science and Technology*, **jourvol** 70, **number** 6, **pages** 959–965, Jun. 2010, ISSN: 02663538. DOI: `10.1016/j.compscitech.2010.02.012`. [Online]. Available: `http://dx.doi.org/10.1016/j.compscitech.2010.02.012%20https://linkinghub.elsevier.com/retrieve/pii/S0266353810000710`.

[145] L. Y. Barros, J. C. Poletto, D. Buneder, R. Flores, G. Gehlen, P. D. Neis, N. F. Ferreira **and** L. T. Matozo, “An experimental study of the transition in the wear

regime of brake friction materials," *Polymer Composites*, **jourvol** 42, **number** 12, **pages** 6310–6321, 2021, ISSN: 15480569. DOI: `10.1002/pc.26299`.

[146] A. A. Alnaqi, "Characterisation of coated lightweight brake rotors by," Ph.D. dissertation, 2014, **page** 330.

[147] T. Okamura **and** M. Ono, "Effect of Brake Disc Surface Texture on Friction Behavior during Running-in," **in** *SAE Technical Papers*, SAE, **october** 2004, ISBN: 2004012765. DOI: `10.4271/2004-01-2765`. [Online]. Available: `https://www.sae.org/content/2004-01-2765/`.

[148] H. Nakanishi, K. Kakihara, A. Nakayama **and** T. Murayama, "Development of aluminum metal matrix composites (Al-MMC) brake rotor and pad," *JSAE Review*, **jourvol** 23, **number** 3, **pages** 365–370, Jul. 2002, ISSN: 03894304. DOI: `10.1016/S0389-4304(02)00203-5`. [Online]. Available: `https://linkinghub.elsevier.com/retrieve/pii/S0389430402002035`.

[149] N. Oda, Y. Sugimoto, T. Higuchi **and** K. Minesita, "Development of Disk Brake Rotor Utilizing Aluminum Metal Matrix Composite," **in** *SAE Technical Papers*, **february** 1997. DOI: `10.4271/970787`. [Online]. Available: `https://www.sae.org/content/970787/`.

[150] R. Dwivedi, "Performance of MMC Rotors in Dynamometer Testing," **march** 1994. DOI: `10.4271/940848`. [Online]. Available: `https://www.sae.org/content/940848/`.

[151] X. Xiao, Y. Yin, J. Bao, L. Lu **and** X. Feng, "Review on the friction and wear of brake materials," *Advances in Mechanical Engineering*, **jourvol** 8, **number** 5, **page** 168 781 401 664 730, **may** 2016, ISSN: 1687-8140. DOI: `10.1177/1687814016647300`. [Online]. Available: `http://journals.sagepub.com/doi/10.1177/1687814016647300`.

[152] P. C. Nunes **and** L. V. Ramanathan, "Corrosion behavior of alumina-aluminum and silicon carbide-aluminum metal-matrix composites," *Corrosion*, **jourvol** 51, **number** 8, **pages** 610–617, 1995, ISSN: 00109312. DOI: `10.5006/1.3293621`.

[153] H. M. Zakaria, "Microstructural and corrosion behavior of Al/SiC metal matrix composites," *Ain Shams Engineering Journal*, **jourvol** 5, **number** 3, **pages** 831–838, 2014, ISSN: 20904479. DOI: `10.1016/j.asej.2014.03.003`. [Online]. Available: `http://dx.doi.org/10.1016/j.asej.2014.03.003`.

[154] S. MOSLEH-SHIRAZI, F. AKHLAGHI **and** D.-y. LI, "Effect of SiC content on dry sliding wear, corrosion and corrosive wear of Al/SiC nanocomposites," *Transactions of Nonferrous Metals Society of China*, **jourvol** 26, **number** 7, **pages** 1801–1808, Jul. 2016, ISSN: 10036326. DOI: `10.1016/S1003-6326(16)64294-2`. [Online]. Available: `http://dx.doi.org/10.1016/S1003-6326(16)64294-2%20https://linkinghub.elsevier.com/retrieve/pii/S1003632616642942`.

[155] W. Neil **and** C. Garrard, "The corrosion behaviour of aluminium-silicon carbide composites in aerated 3.5% sodium chloride," *Corrosion Science*, **jourvol** 36, **number** 5, **pages** 837–851, 1994, ISSN: 0010938X. DOI: `10.1016/0010-938X(94)90174-0`.

[156] H. Rajaei, M. Griso, C. Menapace, A. Dorigato, G. Perricone **and** S. Gialanella, "Results in Materials Investigation on the recyclability potential of vehicular brake pads," *Results in Materials*, **jourvol** 8, **number** November, **page** 100 161, 2020, ISSN: 2590-048X. DOI: `10.1016/j.rinma.2020.100161`. [Online]. Available: `https://doi.org/10.1016/j.rinma.2020.100161`.

[157] S. Shrestha, R. Francis **and** A. Smith, "Alloy selection for wear-resistant lightweight aluminium brake disc," *Surface Engineering*, **january** 2024, ISSN: 0267-0844. DOI: `10.1177/02670844231217399`. [Online]. Available: `http://journals.sagepub.com/doi/10.1177/02670844231217399`.

[158] A. Sinha, G. Ischia, C. Menapace **and** S. Gialanella, “Experimental Characterization Protocols for Wear Products from Disc Brake Materials,” *Atmosphere*, **jourvol** 11, **number** 10, **page** 1102, **october** 2020, ISSN: 2073-4433. DOI: `10.3390/atmos11101102`. [Online]. Available: `https://www.mdpi.com/2073-4433/11/10/1102`.

[159] L. Barros, J. Poletto, D. Buneder, P. Neis, N. Ferreira, R. Pavlak **and** L. Matozo, “Effect of pressure in the transition between moderate and severe wear regimes in brake friction materials,” *Wear*, **jourvol** 438-439, **number** August, **page** 203 112, **november** 2019, ISSN: 00431648. DOI: `10.1016/j.wear.2019.203112`. [Online]. Available: `https://doi.org/10.1016/j.wear.2019.203112%20https://linkinghub.elsevier.com/retrieve/pii/S0043164819312499`.

Appendix A

Appendix

A.1 Appendix section

Calculation for Figures 7.6 and 7.7

Braking power (W) = Torque (Nm) * Angular velocity (radian/s)

Tests are all conducted at a constant shaft rotational speed of 150 rev/min. Therefore:

Angular velocity = 2π * 150/60 = 15.7 rad/s

For example, if time-averaged torque over steady region of test = 162.37 Nm, then:

Braking power (W) = Torque (Nm) * Angular velocity (rad/s) = 162.37 * 15.7 = 2550.5 W

Now, total frictional work done over the duration of the steady-state region of the test given by:

Total brake work done (J) = Average braking power (W) x Steady-state test duration (s)

For example, if the duration of the steady state duration of the test during which emissions are measured is 4000 s, then

Total brake work done = 2550.5 * 4000 = 10202007.98 J = 10.2 MJ

Now, to estimate the total mass of PM emissions from the brake over the 4000s steady portion of the test, we must first convert the Dekati reading in mg/m3 to total mg released from the brake.

The flow rate drawn into the Dekati by the vacuum pump is 9.94 litres per minute and we know 1 litre = 0.001 m^3.

Therefore, the volume flow rate into the Dekati is given by:

9.94 x 0.001 = 0.00994 m^3/min

For example, assume that the steady-state value of PM 2.5 emissions measured by the Dekati is 0.0618 mg/m3

Then this is equivalent to the total emissions over the 4000s steady-state period of test given by:

PM2.5 emissions = 0.0618 * 0.00994 * 4000/60 = 0.04095 mg

To calculate the total emissions from the brake and not just that which is measured by the Dekati, the ratio between the ducting and sample probe is needed.

The diameter of the ducting tube is 225 mm and the sample probe diameter is 5.54 mm

Therefore the cross-sectional area of the duct and sampling probe are as follows;

Area of Duct = π r^2 = $\pi * (0.1125)^2 = 0.03976m^2$

Area of Probe = π r^2 =π * $(0.00277)^2 = 2.41 * 10^{-5}m^2$

Therefore, the ratio between the cross-sectional area of the duct and the sampling probe is;

$0.03976/2.41*10^{-5} = 1649.47$

Given the isokinetic design of the probe, the total PM 2.5 emission in the ducting system over the 4000 s sampling period is then:

PM 2.5 (Total) = 0.040955 * 1649.47 = 67.55 mg

Finally, calculating total PM2.5 emissions/total frictional work over the sampling period, we get for this example:

PM2.5 emissions/ frictional work = 67.55 / 10.2 = 6.62 mg/MJ